Single-column and mixed-layer model analysis of subtropical stratocumulus response mechanisms relevant to climate change

Christopher R. Jones

A dissertation
submitted in partial fulfillment of the
requirements for the degree of

Doctor of Philosophy

University of Washington

2013

Reading Committee:

Christopher Bretherton, Chair

Ka-Kit Tung

Robert Wood

Program Authorized to Offer Degree:
Department of Applied Mathematics

University of Washington

Abstract

Single-column and mixed-layer model analysis of subtropical stratocumulus response mechanisms relevant to climate change

Christopher R. Jones

Chair of the Supervisory Committee:
Professor Christopher Bretherton
Department of Applied Mathematics and Atmospheric Sciences

Subtropical stratocumulus clouds are important part of the Earth's energy budget. The response of low clouds to Earth's changing climate is one of the dominant uncertainties in global warming projections, due primarily to unresolved parameterized cloud processes in global climate models (GCMs). Improving our understanding of the role stratocumulus clouds play in response to climate change requires both a better understanding of the underlying physical mechanisms that govern stratocumulus clouds, and also better representing these processes in GCMs. This work addresses both aspects, using a range of models, from an idealized mixed-layer model (MLM) to a high-resolution large eddy simulation (LES).

The aerosol indirect effect (AIE) for nondrizzling stratocumulus clouds is strongly dependent on an entrainment-sedimentation feedback that increases the entrainment efficiency for higher droplet concentrations, thereby decreasing the cloud amount. However, a single column model (SCM) derived from the CAM5 GCM exhibits the opposite sign of this response mechanism. Using an SCM we find that a combination of issues contribute to this, but the primary cause is due to a representation of cloud condensate within the PBL parameterization that is inconsistent with other microphysical parameterizations that affect the cloud liquid water, rendering the entrainment efficiency insensitive to droplet concentration.

The response of a representative stratocumulus to a variety of idealized climate-change perturbations is used in conjunction with an identically-forced LES to interpret the under-

lying mechanisms behind the observed sensitivity. The MLM and LES agree remarkably well for all cases where the boundary layer doesn't decouple in the LES. For $2\times CO_2$ forcing perturbations estimated from the CMIP3 multimodel mean, the MLM predicts a positive shortwave cloud feedback, like most CMIP3 global climate models. The cloud remains overcast but thins in the warmer, moister, CO_2-enhanced climate, due to the combined effects of an increased lower-tropospheric vertical humidity gradient and an enhanced free tropospheric greenhouse effect that reduces the radiative driving of turbulence. Reduced subsidence due to weakening of tropical overturning circulations and a strengthening of the capping inversion partly counteract these two factors by raising the inversion and allowing the cloud layer to deepen. These compensating mechanisms may explain the large scatter in low cloud feedbacks predicted by climate models.

The rapidity with which a stratocumulus cloud can respond to perturbations is important for understanding its response to perturbations that occur across a range of characteristic time scales. Using a MLM and LES, I show that there are three separate timescales: a slow adjustment timescale associated with boundary layer deepening (several days), an intermediate thermodynamic timescale (approximately 1 day), and a hitherto unidentified fast timescale (6-12 hours) for cloud water path adjustment associated with internal entrainment rate feedbacks. The fast timescale response is elicited by perturbations to overlying humidity and surface and atmosphere temperature, whereas purely radiative perturbations do not elicit an entrainment-liquid water path feedback. A range of MLM entrainment closures are shown to support a fast timescale, provided the entrainment rate is sensitive to the integrated buoyancy flux. The underlying entrainment-liquid flux adjustment mechanism suggests a cloud-thinning response to a uniformly warmed climate perturbation.

TABLE OF CONTENTS

Page

LIST OF FIGURES

LIST OF TABLES

ABBREVIATIONS

BL: Boundary layer. Used interchangeably with PBL.

CAM: Community Atmosphere Model GCM. CAM5 refers to CAM version 5.

CCN: Cloud condensation nuclei.

GCM: Global climate model (a.k.a. general circulation model).

ITCZ: Inter-tropical convergence zone.

LES: Large eddy simulation.

LW: Longwave radiation.

LWCF: See LWCRE.

LWCRE: Longwave cloud radiative effect.

LWP: Column integrated liquid water path.

MBL: Marine boundary layer. Used interchangeably with PBL.

MLM: Mixed-layer model.

PBL: Planetary boundary layer.

SCAM: Single-column model implementation of CAM.

SCM: Single-column model.

SST: Sea-surface temperature.

STBL: Stratocumulus–topped boundary layer.

SW: Shortwave (solar) radiation.

SWCRE: Shortwave cloud radiative effect.

SWCF: See SWCRE.

TOA: Top of atmosphere.

VARIABLE NAMES

Variable names and physical constants, along with brief description, defining relationships, and units (in parentheses).

Constants

c_p: Specific heat of dry air, $c_p \approx 1005$ J kg^{-1} K^{-1}.

L: The latent heat of vaporization for water, $L \approx 2.5 \times 10^6$ J kg^{-1}.

g: Acceleration due to gravity, $g = 9.8$ m s^{-1}.

δ: 0.608

R_d: Gas constant for dry air, $R_d = 287.04$ J kg^{-1} K^{-1}.

ρ_w: Density of liquid water $\rho_w \approx 1000$ kg m^{-3}.

Variables

A: Non-dimensional entrainment efficiency.

h: Moist static energy $h = c_pT + gz + Lq_v$ (J/kg).

p: Pressure (Pa).

q_v: Water vapor mixing ratio (kg/kg).

q_ℓ: Liquid water mixing ratio (kg/kg).

q_t: Total water mixing ratio $q_t = q_v + q_\ell$.

s_ℓ: Liquid static energy $s_\ell = c_p T + gz - Lq_\ell = h - Lq_t$ (J/kg).

s: Static energy $s = c_p T + gz$ (J/kg).

s_v: Virtual static energy, $s_v = c_p T_v + gz \approx s_{v\ell} + (1 - (1+\delta)\varepsilon) Lq_\ell$ (J/kg)

s_{vl}: Virtual liquid static energy, $s_{v\ell} \approx h - \mu L$ (J/kg).

T: Temperature (K).

w_*: Convective velocity scale, defined by $w_*^3 = 2.5 \int_0^{z_i} \langle w'b' \rangle dz$ (m s^{-1}).

w_e: Entrainment rate (m s^{-1}).

z: Height above surface (m).

z_i: Inversion height (m).

z_b: Stratocumulus cloud base (m).

β: Thermodynamic variable, $\beta = \frac{1+\gamma\varepsilon(1+\delta)}{1+\gamma}$.

ε: $\frac{c_p T}{L}$.

γ: $\frac{L}{C_p} \frac{\partial q^*}{\partial T}$.

ρ: Density of air (kg m^{-3}).

θ_ℓ: Liquid water potential temperature, $\theta_\ell \approx \theta - \frac{L}{c_p} q_\ell$ (K).

μ: $1 - \delta\varepsilon$.

ACKNOWLEDGMENTS

I wish to express my thanks and gratitude to Chris Bretherton for his guidance throughout these years. I thank Peter Blossey for performing the large eddy simulations included in this analysis, as well as for our many useful discussions and ongoing collaborations. Thanks are also due to Rob Wood, Peter Caldwell, and the many others who have provided feedback, discussions, and criticisms that have substantially improved the quality of this research.

Chapter 1

INTRODUCTION

1.1 Stratocumulus clouds and their relevance to climate

Stratocumulus (Sc) clouds are convective, boundary layer clouds that form under a capping temperature inversion over relatively cooler surface temperature[1]. Stratocumuli are the most ubiquitous of all cloud types (Warren et al., 1986, 1988), covering approximately 22% of the ocean and 12% of the land surface (Hahn and Warren, 2007 (updated 2009)). The frequency of occurrence of marine stratocumulus is well-correlated with lower tropospheric stability (LTS, Klein and Hartmann, 1993) and estimated inversion strength (EIS Wood and Bretherton, 2006), which are measures of the relative coolness of the sea-surface temperature (SST) compared to the temperature in the lower free troposphere. In the midlatitude regions, marine stratocumulus tend to form particularly in summer under regions of synoptic descent following cold fronts associated with extratropical cyclones (Norris and Iacobellis, 2005). They are also commonly found in semi-permanent Sc cloud decks over the eastern subtropical oceans, under strong temperature inversions sustained by large scale subsidence from the descending branch of the Hadley circulation, over relatively cool SST from coastal upwelling, and supported by cold advection. The strong temperature inversion inhibits penetrative convection, and the large scale subsidence counteracts boundary layer deepening through entrainment. The relative steadiness of these stratocumulus decks has made them the frequent target of observational field campaigns (e.g., Stevens et al., 2003; Bretherton et al., 2004; Wood et al., 2011) which have provided valuable information regarding the structure of the marine boundary layer (MBL).

Stratocumulus clouds play an important role in the earth's radiation budget, and it is

[1]For an excellent review of stratocumulus, see (Wood, 2012). The discussion provided in the current introduction merely scratches the surface

in this regard that they are directly relevant to the global climate and climate change. In general, clouds have both a longwave (LW) and shortwave (SW) radiative effect. Clouds reflect incoming solar radiation, thereby decreasing the net incoming top of atmosphere (TOA) SW radiation, having a cooling effect. Clouds also absorb infrared radiation from the surface and re-emit it at a lower cloud-top temperature, thus decreasing the outgoing LW radiation at the TOA, yielding a warming effect. Overall, the global mean balance is a net cooling effect (Ramanathan et al., 1989; Loeb et al., 2009). For stratocumuli in particular, the impact in the LW is minimal due to the cloud top temperature being relatively close to the surface temperature, while the SW contribution is quite large (Chen et al., 2000), making them an important factor in Earth's TOA radiative balance. A number of studies have argued that, due to the large SW footprint and wide geographical spread of Sc, a relatively small fractional change in the Sc cloud amount is capable of inducing a radiative effect of the same magnitude as doubling CO_2 (Hartmann and Short, 1980; Randall et al., 1984; Slingo, 1990).

1.2 The STBL

Physical Processes

The stratocumulus-topped boundary layer (STBL) is shaped by a combination of cloud-top LW radiative cooling, cloud-top entrainment mixing, surface sensible and latent heat fluxes, horizontal advection, solar heating, and drizzle (see Figure 1.1 for a schematic representation of the contributing processes and mean vertical structure of a well-mixed STBL).

Stratocumulus are distinguished from stratus (St) and cumulus (Cu) by a visibly cellular structure that is driven by some form of convection. This may be surface driven (such as in the case of cold air outbreaks), or driven primarily by cloud-top, LW radiative cooling, which acts as "upside-down thermal convection," with cold plumes descending from cloud-top driving the convective motion. In the persistent subtropical stratocumulus decks, LW radiative cooling is the dominant term in the energy budget of the STBL (Caldwell et al., 2005).

Surface sensible heat flux (SHF) drives turbulent mixing from the surface, and latent

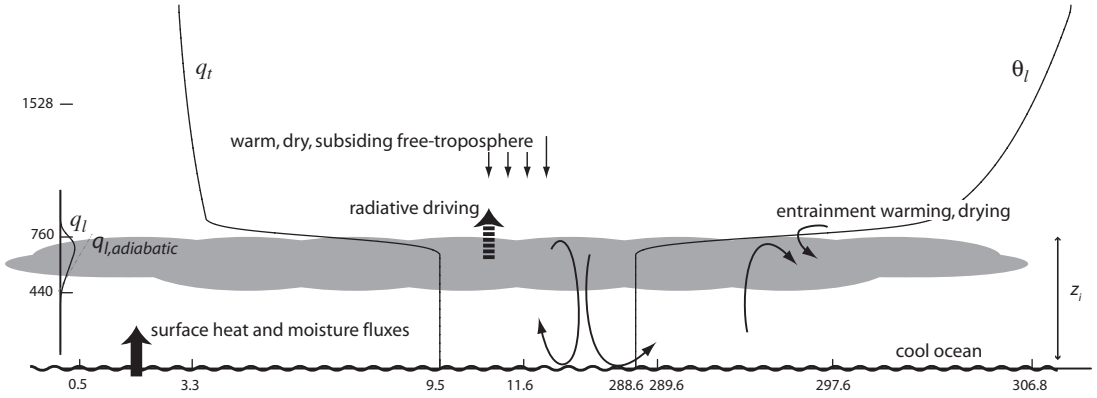

Figure 1.1: Sketch of mean thermodynamics structure of lower troposphere for July 2001, near 30°N,120°W. The potential temperature, specific humidity, and height at 850 hPa are indicated, as are values within the STBL and at the sea surface. *Figure and caption reproduced from Figure 12 of Stevens et al. (2007).*

heat flux (LHF) provides a source of moisture to the boundary layer. As moist parcels from the surface in updraughts rise past the lifted condensation level (LCL), condensation forms onto cloud condensation nuclei (CCN). This process releases latent heat, producing an even greater buoyancy boost to the updraught parcel and spurring further turbulent mixing and condensation within the cloud layer.

The updraft parcels are inhibited from penetrating too far into the free troposphere by the capping temperature inversion. Relative to the warm free troposphere air, the boundary layer updraft parcels are moist but negatively buoyant. As the updraft reaches this entrainment interface layer (EIL) it mixes with typically dry, warm free troposphere air. This cloud top mixing process, known as *entrainment*, is an extremely important factor in the STBL, contributing both to boundary layer deepening (Randall, 1984) as well as boundary layer warming and drying. Entrainment is typically the second largest term in the STBL energy budget. If conditions are favorable, a statistical steady-state may be obtained when the mean entrainment rate is balanced by the large scale subsidence[2].

[2]This equilibration occurs on a timescale on the order of several days (Schubert et al., 1979b), however, which is slower than the many processes which may interfere with achieving this steady state (e.g., diurnal heating or synoptic variability).

The net effect of cloud-top LW radiative cooling, entrainment warming, and evaporative cooling in the EIL provides enough cooling for the downdraught parcel to become negatively buoyant relative to the cloud top boundary layer air. Thus, because updrafts tend to be moister and warmer than downdrafts, there is a net positive buoyancy flux within the STBL that serves as the primary source of turbulent kinetic energy (TKE).

Provided the STBL is shallow enough, and turbulent mixing is vigorous enough, the surface and cloud-top turbulent drivers conspire to homogenize the total water mixing ratio $q_t = q_v + q_\ell$ and the moist adiabatically conserved temperature-like variable (e.g., liquid potential temperature θ_ℓ), and the layer is referred to as "well-mixed" or "coupled." Advection within the STBL also plays a role, with cold advection tending to help maintain a shallow, well-mixed layer and warm advection tending to support a deeper layer.

Particularly as the STBL deepens and the cloud liquid water content (LWC, q_ℓ) increases, a stable region between the surface and the cloud layer may be induced through a region of negative buoyancy flux developing below the cloud base. The stratified STBL may then decouple into two separate mixed layers, a cloud layer and a subcloud layer (Nicholls, 1984). Decoupled layers frequently occur, even within the persistent stratocumulus decks off eastern continents. Using aircraft observational data, Jones et al. (2011) estimated that approximately 40% of the boundary layer sampled during the VOCALS field campaign in the Southeast Pacific (Wood et al., 2011) was decoupled, with decoupled layers associated with a deeper boundary layer. Despite the importance of decoupling for vertical transport of heat and moisture in the boundary layer, as well as its role in the Sc-Cu transition and stratocumulus break-up (Bretherton and Wyant, 1997), our focus is on the well-mixed boundary layer in the remainder of this document[3].

In the well-mixed STBL, the cloud base approximately coincides with the LCL. Within the cloud layer, q_ℓ typically increases adiabatically from cloud base, though departures from adiabaticity are not uncommon (Wood, 2012). Frequently the LWC near the cloud top

[3]One practical reason for our focus on the well-mixed boundary layer is that it allows us to use a mixed-layer model (Chapter 2.1) in the analysis (as in Chapters 4-5). More broadly, though, we expect that the STBL processes investigated in this analysis should also apply to the decoupled STBL, provided cloud top entrainment is a dominant process governing the STBL structure, but further analysis in a decoupled setting would be required to verify this hypothesis.

is sub-adiabatic, due to entrainment-induced droplet evaporation (Nicholls and Leighton, 1986).

Due to their limited depth, stratocumulus clouds do not produce heavy rain. However, marine stratocumulus frequently drizzle, with the median rate approximately 0.6 mm d^{-1} (Leon et al., 2008), peaking near cloud-base and evaporating below cloud base. Drizzle is highly variable in STBLs because it is very sensitive to cloud thickness and concentrations of cloud droplet-nucleating aerosols, both of which are quite variable in space and time. Precipitation that reaches the surface may act as a moisture sink to dry the STBL, but even drizzle that evaporates below the surface tends to stabilize the STBL by heating the cloud layer and cooling the subcloud layer.

Feedback Mechanisms

The individual physical processes of the previous section are each intimately linked to the others through a complex network of feedbacks. Some of the dominant feedback mechanisms are summarized in the flow chart of Figure 1.2, which represents both internal feedbacks between boundary layer quantities and STBL responses to changes in external forcings, such as the large scale dynamics or aerosol concentrations.

The many intricate, nonlinear feedbacks operating across a range of timescales that regulate boundary layer clouds is one of the many features that makes them so difficult to accurately represent in GCMs.

One of the most fundamental macrophysical feedback loops relates cloud amount, TKE, and entrainment (Wood, 2012). Consider, for example, an increase in the cloud amount. This directly increases the TKE in the boundary layer by increasing the integrated buoyancy flux. Increased LWP also directly increases the entrainment efficiency through additional evaporative enhancement (Turton and Nicholls, 1987), and also increases cloud droplet sedimentation, which in itself *decreases* entrainment efficiency (Bretherton et al., 2007). Focusing first on the TKE, increased TKE drives more entrainment. Increased entrainment tends to decrease TKE through stabilization of the boundary layer, and, on a slower timescale, warms and dries the STBL which typically decreases (though may increase, depending on

the large scale conditions – see Randall, 1984) cloud thickness and LWP. Thus, considering only LWP, TKE, and w_e in Figure 1.2 already shows a complicated set of interrelated processes through which individual physical processes respond to changes in one part of the system.

Consider next the precipitation-mediated macrophysical feedbacks. Increasing the LWP tends to increase precipitation through increased collision-coalescence growth of droplets (Comstock et al., 2005). In the previous section I argued that precipitation stabilizes the STBL by warming the cloud layer while cooling the subcloud layer. This stabilization reduces TKE, working against the additional TKE generated by a thicker cloud. TKE supports precipitation by increasing the time drizzle drops spend in the cloud layer, thus aiding in their growth (Wood, 2012), so inhibiting TKE inhibits this process. For sufficiently heavy drizzle, the STBL will dry due to the flux of liquid water out through the surface, thereby decreasing the LWP.

Similarly, microphysical changes in cloud droplet concentration will affect the entrainment rate through cloud droplet sedimentation (Ackerman et al., 2004; Bretherton et al., 2007) and the amount of precipitation through its role in the collision efficiency.

From the perspective of cloud-climate feedbacks, the driving question is to understand how the STBL will respond to changing large scale conditions in the global mean. The coupling of the STBL to the large scale conditions modulates the relative strength of these feedbacks (e.g., the extent of entrainment drying depends on the overlying humidity), providing for a wide range of possible expressions for these feedbacks based on the large scale forcings. This is at the heart of the cloud-climate feedback uncertainties. Analyzing the response of a STBL to a variety of perturbations to the large scale forcings is the subject of Chapter 4.

1.3 Motivation for this work

The overarching motivation for this work is to better understand the ways in which Sc respond to climate change, and how this response in turn influences climate change. Progress toward this goal requires us to improve our understanding of the underlying physical mechanisms that govern Sc response to the changes expected to accompany global warming

(particularly, changes in aerosol and greenhouse gas concentrations, surface and air temperature, and large scale circulation), and also to better represent these processes in GCMs.

Cess et al. (1990) demonstrated that cloud-climate feedbacks were the primary cause for intermodel spread in climate sensitivity in an intercomparison of 19 GCMs. Although there has been progress in the understanding and assessment of cloud-climate interactions in the intervening years (Bony et al., 2006), cloud-climate feedbacks are still the greatest source of uncertainty in climate sensitivity in GCMs (Randall et al., 2007). In particular, marine boundary layer (MBL) clouds, are not well-represented in the current climatology by GCMs (Lauer et al., 2010) and have been identified as the primary source of this uncertainty in global climate sensitivity (Bony and Dufresne, 2005).

Accurate representation of cloud response to perturbations in radiative forcing at the global scale are complicated by the nonlinear interactions of clouds with the environment (Soden et al., 2008). Although there is increasing consensus amongst models that cloud response to climate change exerts a net warming effect, the uncertainty is substantial. Our understanding of the physical processes underlying the cloud-climate interaction of MBL clouds is limited, and the relative strengths of interactions between local physical processes and large scale forcings underpins much of the uncertainty (Bony et al., 2006). MBL clouds respond to changes in large scale circulations of the atmosphere (dynamics), as well as local thermodynamics. Among these effects, the thermodynamic component of the cloud response, which relies heavily on subgrid parameterizations of physical processes, is the least understood and the cause for the greatest discrepancy between models (Bony et al., 2004).

It is our view that a range of cloud models, from the simplest mixed-layer models (MLMs), to single-column, and large eddy simulations (LESs), working in concert provides a critical understanding of the challenges and strengths of each modelling approach, leading to a deeper understanding of the underlying processes being modelled.

At the simplest level is the MLM. First proposed by Lilly (1968), the MLM exploits the vertical structure of a well-mixed STBL to construct a model that constrains the vertical profiles of q_t and s_ℓ to be well-mixed below a capping inversion. MLMs have repeatedly been used throughout the years to provide insight into and understanding of MBL clouds. Schubert et al. (1979a) and Schubert et al. (1979b) applied a MLM to an air mass that is

assumed to advect over warmer or cooler SST, or in a region of differing large scale divergence, showing that under cold advection the MBL warms, moistens and deepens, while the opposite occurs under warm advection, while the divergence affected the cloud top height on a relatively slow timescale, in the process identifying characteristic thermodynamic and inversion deepening timescales. Bretherton and Wyant (1997) used a MLM to show that increased latent heat flux (LHF) over warmer SST could induce the mixed layer to decouple through a deepening-warming mechanism, thereby explaining the Sc-Cu transition. Caldwell and Bretherton (2009) used a MLM in a "two-box" framework (popularized by Pierrehumbert, 1995) to assess Sc climate change-induced response mechanisms. They identified a subsidence-lapse rate mechanism for increasing the SWCF, in which increased free-tropospheric stability in a warmed climate conspires to induce decreased subsidence[4] which simultaneously deepens the boundary layer while weakening entrainment, thus increasing LWP in the warmer climate. Recently, Caldwell et al. (2012) interpreted an ensemble of GCM climate-change simulations through a MLM. They showed that, even though within the set of GCMs the cloud fraction does not compare well with observations by a variety of metrics (e.g., mean state or correlation with EIS), the same GCMs do perform significantly better when the output is interpreted through the MLM. Furthermore, BL clouds are well-correlated with EIS (Wood and Bretherton, 2006), and though this relationship is captured well by the MLM, it is not by the parent GCMs. The net result is that the MLM tends to predict a negative cloud feedback from low clouds (i.e., they offset some of the surface temperature increase due to global warming), while the GCMs tend to produce more positive feedbacks. Thus, MLMs have been successfully used to evaluate and interpret STBL processes, and also to investigate cloud-climate feedbacks. However, because of the ubiquity of decoupling and cumulus convection over much of the subtropical oceans, MLMs present an inherently limited perspective that must be carefully tested against models that support more realistic MBL vertical structure.

GCMs rely on parameterizations for subgrid processes, including stratiform, shallow cumulus, boundary layer mixing, deep convection, and cloud microphysics. Single col-

[4]Decreased subsidence through a weakening of the Hadley circulation is an expected dynamic change in a warmed climate, according to Vecchi and Soden (2007).

umn models (SCMs) have long provided a testing platform on which parametrizations are validated through idealized studies (e.g., Zhang and McFarlane, 1995; Lock et al., 2000a; Bretherton and Park, 2009a; Park and Bretherton, 2009). The use of SCMs to evaluate unexpected behavior in a parametrization is thus a valued approach, allowing one to isolate the behavior of the parametrization. This is the approach we take to address the aerosol indirect effect (AIE) for non-drizzling stratocumulus in SCAM5 (Chapter 3).

SCMs have also been used to study cloud-climate feedbacks directly. In principle, SCMs can more realistically represent MBL vertical structure and hence cloud response. In practice, few SCMs achieve this goal because of discretization issues associated with their coarse vertical resolution and complications arising from interactions between all the moist physics parameterizations that affect the simulated clouds. Zhang and Bretherton (2008) used an SCM to study cloud-climate feedbacks directly using a two-box framework in order to explore the underlying causes behind the negative low cloud feedback of the parent CAM3 GCM, and found that the observed low cloud feedback in their study resulting from unphysical interactions between parameterizations of boundary layer turbulence, shallow, and deep convection. Recently, there have been a number of intercomparisons featuring SCMs (Zhu et al., 2005; Wyant et al., 2007; Zhang et al., 2013), often in concert with LES intercomparisons for the same case studies (Stevens et al., 2005; Ackerman et al., 2009; Blossey et al., 2013). These studies provide insights into the behavior of GCM parameterizations ideally forced to represent a specific cloud regime. A challenge for single-column climate modelling is that there is no unambiguous way to project findings from the SCM regarding climate feedback mechanisms onto those of the parent GCM.

LESs are the foremost tool for high-resolution, turbulence-resolving modelling commonly in use today. There is an LES component to each of the analyses presented in this dissertation. In Chapter 3, LES is used as a benchmark for the expected response of a non-drizzling nocturnal stratocumulus to changes in droplet concentration. Chapter 4 uses a single LES analysis of cloud-climate feedbacks for a well-mixed STBL and further interprets the behavior through a MLM. In Chapter 5, a LES is used to verify the existence of a fast time-scale that is derived from MLM analysis.

1.4 Organization of remaining chapters

In the remaining chapters, I present analyses of various ways in which STBL feedbacks are expressed in a MLM, SCM, and LES. Each is framed in terms of some combination of the DYCOMSII–RF01 (Stevens et al., 2005) or CGILS (Zhang et al., 2013) case study. The models and case studies are described collectively in Chapter 2.

To ease the confusion of the reader, I have included glossaries starting on page *ix* that list and briefly describe the many acronyms, abbreviations, variable names, and symbols used liberally throughout this document.

Chapters 3-5 present the bulk of the analysis performed for this dissertation. I have attempted to make each of these chapters as self-contained as possible, each complete with its own introduction and conclusions. If desired, these can be read independently in conjunction with the relevant portions of Chapter 2.

Chapter 3 aims to improve the representation of the aerosol indirect effect (AIE) in the CAM5 GCM by addressing the sensitivity of cloud LWP to droplet concentration (N_d) in a non-drizzling, nocturnal stratocumulus, using both SCM and LES. The SCM is shown to exhibit a LWP sensitivity to N_d opposite to that of the LES, due primarily to the internal representation of the liquid water profile within the boundary layer mixing scheme that contributes to an entrainment efficiency insensitive to droplet concentration.

In Chapter 4, an MLM and LES are used to assess the response of a prototypical STBL to changes in large scale forcings representative of climate change, with the aim of identifying the underlying physical response mechanisms. Perturbations considered include increased CO_2 concentration, increased temperature (both surface and aloft), increased EIS, increased free troposphere relative humidity, decreased horizontal wind speed, and warming in the presence of decreased subsidence. Each of these perturbations were chosen based on changes expected to accompany climate warming.

Chapter 5 identifies a hitherto unarticulated fast internal STBL adjustment timescale (on the order of a few hours) using MLM and LES. This fast scale is an expression of a physically robust entrainment-LWP feedback. We also consider which perturbations project onto this fast scale, and the role that is played by the entrainment closure. Results and

suggestions for future work are broadly summarized in Chapter 6.

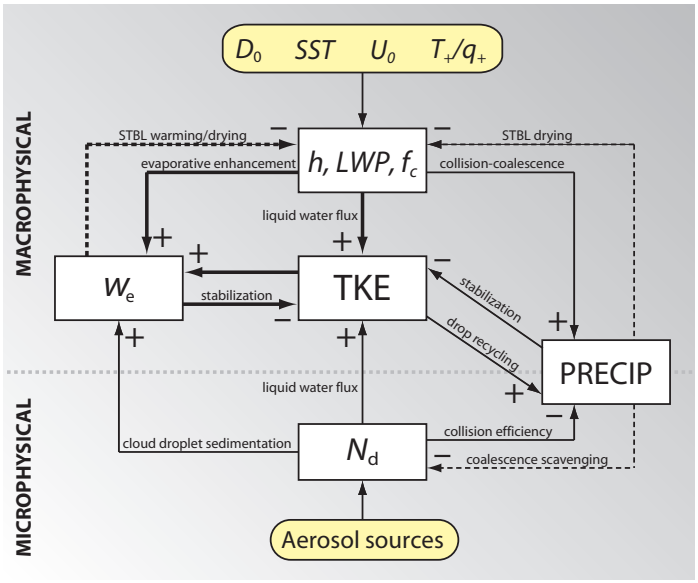

Figure 1.2: Conceptual system dynamics diagram illustrating important feedbacks that serve to regulate the thickness h, liquid water path LWP, and cloud cover f_c of stratocumulus clouds. Yellow rounded rectangles show external meteorological and aerosol parameters: surface divergence D_0, surface temperature SST, surface wind speed U_0, free-tropospheric temperature T_+ and humidity q_+, and aerosol sources. White boxes show key internal variables: TKE represents a measure of the strength of the TKE within the STBL; w_e is the cloud-top entrainment rate; PRECIP is a measure of the precipitation rate; and N_d is the cloud droplet concentration, which is the key microphysical variable that can influence macrophysical processes. Plus and minus signs indicate positive and negative impacts of one variable on another, with the key physical processes accompanying the arrows where necessary. Thick arrows indicate the cloud-radiation-turbulent-entrainment feedback system that constitutes a dominant negative feedback system regulating stratocumulus thickness and cover. Solid lines indicate feedbacks that operate on time scales comparable with the eddy turnover time scale (typically an hour or less), while dashed lines indicate feedbacks that operate on markedly longer time scales. The thick dotted gray line is used to separate the chart into (top) macrophysical and (bottom) microphysical variables, with precipitation straddling the boundary between the macrophysical and microphysical realms. *Figure and caption reproduced from Figure 14 of Wood (2012) with the permission of the author.*

Chapter 2

MODELS

This chapter provides an overview of the mixed-layer model (MLM), single column model (SCM), and large eddy simulation (LES) used in this analysis. The MLM is featured in Chapters 4 and 5. The SCAM5 SCM is the focus of Chapter 3, and the LES is used throughout Chapters 3-5.

2.1 MLM

The mixed-layer model, first proposed by Lilly (1968), is a bulk model (Stevens, 2006) that uses the structure of the well-mixed STBL to construct a system of 3 ordinary differential equations (ODEs) governing the evolution of the boundary layer. The MLM assumes that moist-adiabatically conserved moisture and temperature variables are well-mixed by turbulence and hence remain vertically uniform beneath an infinitesimally thin capping temperature inversion at all times. The base of the inversion coincides with the cloud top, and the STBL is assumed to be 100% cloud-covered, provided the lifting condensation level (LCL) is below the inversion. Observations confirm that well-mixed cloud-topped boundary layers occur frequently in nature (e.g., Jones et al., 2011), and mixed-layer theory also generates plausible STBL equilibrium states in areas well-known for the presence of stratocumulus when forced by observed climatology (Stevens, 2006).

The MLM used in this analysis follows in the tradition of Bretherton and Wyant (1997), Uchida et al. (2010), and Caldwell and Bretherton (2009). As in Bretherton and Wyant (1997), we construct the MLM in terms of the inversion height z_i, the total water mixing ratio q_t, and the moist static energy h. Here,

$$q_t = q_v + q_\ell \tag{2.1}$$

$$h = c_p T + gz + Lq_v = s_\ell + Lq_t, \tag{2.2}$$

where q_v is the water vapor mixing ratio, q_ℓ is the liquid water mixing ratio, $c_p \approx 1005$ J kg^{-1} K^{-1} the specific heat of dry air, T the temperature, $g = 9.8$ m s^{-1} the acceleration due to gravity, and $L \approx 2.5 \times 10^6$ J kg^{-1} is the latent heat of vaporization.

Following Bretherton and Wyant (1997), budget equations for h and q_t can be written as:

$$\frac{\partial z_i}{\partial t} = w_e + \overline{w_s(z_i)} \tag{2.3a}$$

$$\frac{\partial h}{\partial t} = -\frac{\partial E}{\partial z} - (\boldsymbol{v} \cdot \nabla_H h) \tag{2.3b}$$

$$\frac{\partial q_t}{\partial t} = -\frac{\partial W}{\partial z} - (\boldsymbol{v} \cdot \nabla_H q_t)\,. \tag{2.3c}$$

Here w_e is the entrainment rate, $\overline{w_s(z_i)}$ the specified large scale subsidence rate, $(\boldsymbol{v} \cdot \nabla_H \phi)$ is the specified, vertically uniform horizontal advection of ϕ[1], and

$$E(z) = \langle w'h' \rangle(z) + \frac{F_R(z)}{\rho_0} \tag{2.4a}$$

$$W(z) = \langle w'q_t' \rangle(z) + F_P(z), \tag{2.4b}$$

where $\langle w'\phi' \rangle$ is the horizontally averaged upward turbulent flux of ϕ, $F_R(z)$ is the net radiative flux at height z, $F_P(z)$ is the precipitation flux, and ρ_0 is a reference boundary layer density. Assuming h and q_t are vertical uniform requires $E(z)$ and $W(z)$ to be linear functions of z. The surface fluxes are parameterized using a bulk aerodynamic formula,

$$\langle w'\phi' \rangle(0) = C_T V \Delta^s \phi, \tag{2.5}$$

and the turbulent flux at the inversion interface is provided by the jump condition

$$\langle w'\phi' \rangle(z_i) = -w_e \Delta^i \phi, \tag{2.6}$$

where $\Delta^i \phi \equiv \phi(z_i^+) - \phi$, $C_T \approx 1 \times 10^{-3}$ is a non-dimensional surface transfer coefficient, V is the surface wind speed, $\Delta^s \phi \equiv \phi^*(SST, p_0) - \phi$, p_0 is the surface pressure, SST is

[1]Here, and throughout this chapter, ϕ is used as a dummy variable to refer to either h or q_t.

the sea surface temperature, and ϕ^* is understood to be evaluated assuming 100% moisture saturation.

Combining these relations we can write the MLM prognostic equations as:

$$\frac{dz_i}{dt} = w_e + \overline{w_s(z_i)} \tag{2.7a}$$

$$\frac{dh}{dt} = \frac{1}{z_i}\left(w_e \Delta^i h + C_T V \Delta^s h - \Delta F_R^{BL}/\rho_0 - z_i\left(\boldsymbol{v}\cdot\nabla_H h\right)\right) \tag{2.7b}$$

$$\frac{dq_t}{dt} = \frac{1}{z_i}\left(w_e \Delta^i q_t + C_T V \Delta^s q_t + F_P(0) - z_i\left(\boldsymbol{v}\cdot\nabla_H q_t\right)\right), \tag{2.7c}$$

where $\Delta F_R^{BL} = F_R(z_i^+) - F_R(0)$ is the radiative flux divergence across the boundary layer.

In (2.7), the surface properties (SST and p_0), horizontal advection tendencies, subsidence rate, and free troposphere moisture and temperature profiles must be specified. The remaining subsections are devoted to calculating the terms on the right hand side of (2.7). The required steps are:

1. Extract relevant aspects of the STBL from z_i, h, and q_t. In particular, this requires the cloud base height z_b and the q_ℓ profile (needed in the following steps).

2. Calculate $F_R(z)$ and $F_P(z)$.

3. Use the entrainment parameterization to determine w_e.

2.1.1 STBL State

Determining z_b requires finding the LCL by solving

$$q^*(p(z_b), T(z_b)) = q_t \tag{2.8}$$

for z_b, where q^* is a specified saturation function[2]. The specifics of this calculation depend on which simplifications are made when evaluating moist thermodynamic quantities.

[2]For q^*, and many other moist thermodynamic functions and derived quantities, I use a set of thermodynamic scripts provided by Dr. Christopher S. Bretherton, based largely on formulas provided in Bolton (1980).

The current MLM supports two sets of choices, denoted as "linearized" and "full"[3] moist thermodynamics. Salient differences between the two are summarized in Table 2.1.

Using linearized thermodynamics, as in Bretherton and Wyant (1997), the calculation of cloud base follows Schubert et al. (1979a),

$$z_b(h, q_t) = \frac{1}{H}\left((1+\gamma)\Delta^s q_t - \frac{\gamma}{L}\Delta^s h\right), \tag{2.9}$$

where $H = (dq^*/dz)_u$ is the rate of change of q^* along a dry adiabat and $\gamma = \frac{L}{c_p}\frac{\partial q^*}{\partial T}$. The advantage to this expression is that z_b is determined as a linear combination of the surface fluxes, but a disadvantage is that any perturbation to SST results in an instantaneous jump in the cloud base.

Using full moist thermodynamics, $p(z_b)$ and $T(z_b)$ are analytically calculated by integrating the hydrostatic balance equation from the surface to z_b,

$$\frac{\partial p}{\partial z} = -\rho g \qquad \text{(Hydrostatic balance)}. \tag{2.10}$$

This requires using the equation of state to eliminate ρ from (2.10):

$$\begin{aligned} p &= \rho R_d T_v && \text{(Equation of state)} \\ &= \rho \frac{R_d}{c_p}(s_\ell - gz)(1+\delta q_t) && \text{(Valid up to LCL)}. \end{aligned} \tag{2.11}$$

Substituting (2.11) into (2.10) and integrating yields:

$$p(z) = p_0\left[\frac{s_\ell - gz}{s_\ell}\right]^{\frac{c_p}{R_d}\frac{1}{(1+\delta q_t)}} \qquad \text{for } z \le z_b. \tag{2.12}$$

Inserting $p(z_b)$ from (2.12) and $T(z_b) = (s_\ell - gz_b)/c_p$ into (2.8), this nonlinear equation can be numerically solved for z_b using a root-finding algorithm (e.g., using MATLAB's "fzero" algorithm of Forsythe et al., 1977). Because z_b is determined entirely based on the air temperature and pressure, an instantaneous perturbation to the surface or free troposphere

[3]This is not to suggest that the "full" moist thermodynamics option does not include simplifying assumptions, but only that it is slightly less idealized than the linearized assumptions.

does not result in a step-change in z_b.

The q_ℓ profile is determined from

$$q_\ell(z) = \int_{z_b}^{z_i} \left(\frac{dq^*}{dz}\right)_s dz, \tag{2.13}$$

where dq^*/dz_s is an expression for the rate of change of the saturation mixing ratio along a moist adiabat, following from the Clausius-Clapeyron relation combined with the moist adiabatic lapse rate. If using linearized moist thermodynamics, a constant rate for $\left(\frac{dq^*}{dz}\right)_s$ is assumed based on the reference density, pressure, and temperature. Otherwise, a height-dependent value is determined numerically. This height dependent value is, in practice, nearly constant, and (2.13) is generally well approximated to increase linearly from cloud base.

2.1.2 Precipitation and Sedimentation

The precipitation flux, in units mm s^{-1}, is calculated following Caldwell and Bretherton (2009) as

$$F_P(z) = \begin{cases} \exp\left[-k\left(\frac{z_b - z}{\overline{r}^{2.5}}\right)^{1.5}\right] F_P(z_b), & z < z_b, \\ \left[1 - \left(\frac{z - z_b}{z_i - z_b}\right)^3\right] F_P(z_b), & z_b \le z < z_i \\ 0 & z \ge z_i, \end{cases} \tag{2.14}$$

where $k = 320\,\mu\text{m}^{3.75}\,\text{m}^{-1.5}$, $\overline{r} = 40\,\mu$m, and

$$F_P(z_b) = -F_{b0}\left(\frac{LWP}{N_d}\right)^{\alpha_P}, \tag{2.15}$$

with F_{b0} and α_P depending on whether or not one is using LES-tuned precipitation ($F_{b0} = 2.6 \times 10^{-7}$, $\alpha_P = 3.25$, as in Uchida et al., 2010), or default precipitation ($F_{b0} = 4.3 \times 10^{-6}$, $\alpha_P = 1.75$). Eq. (2.15) assumes LWP has units of g m^{-2} and N_d has units of cm^{-3}.

Cloud droplet sedimentation follows Bretherton et al. (2007) and Ackerman et al. (2009)

as

$$P_{\text{sed}}(z) = c\left(\frac{3}{4\pi\rho_w N_d}\right)^{2/3}(\rho q_\ell)^{5/3}\exp\left(5\ln^2\sigma_g\right) \tag{2.16}$$

$$w_{\text{sed}} = \frac{P_{\text{sed}}(z_i^-)}{\rho q_\ell}, \tag{2.17}$$

where $\sigma_g = 1.2$ is the geometric standard deviation, ρ is the density of air, ρ_w is the density of liquid water, and $c = 1.19 \times 10^8$ m^{-1} s^{-1} (Rogers and Yau, 1989, p. 125).

2.1.3 Radiation

Radiation can be run using multiple configurations. Idealized longwave radiation follows Stevens et al. (2005), and idealized shortwave radiation follows the treatment in Chapter 5.6. An interface to the Rapid Radiative Transfer Model for GCMs (RRTMG, Iacono et al., 2008; Mlawer et al., 1997) package is also supported, and is used in Chapter 4.

2.1.4 Entrainment

Following Bretherton and Wyant (1997), be default we use a Turton-Nicholls (hereafter TN) style entrainment closure (Nicholls and Turton, 1986), with sedimentation included in the entrainment efficiency following Bretherton et al. (2007):

$$w_e = \frac{A w_*^3}{z_i \Delta^i b}, \tag{2.18}$$

where $\Delta^i b$ is the inversion jump of the buoyancy variable, A is a non-dimensional entrainment efficiency, and

$$w_*^3 = 2.5\int_0^{z_i}\langle w'b'\rangle dz, \tag{2.19}$$

with $\langle w'b' \rangle$ the horizontally averaged buoyancy flux. We use the virtual static energy

$$s_v = c_p T_v + gz \tag{2.20}$$

$$= \underbrace{h - \mu L q_t}_{s_{v\ell}} + (1 - (1+\delta)\varepsilon)\, L q_\ell \tag{2.21}$$

to define the buoyancy flux as

$$\langle w'b' \rangle (z) = \frac{g}{s_{v0}} \langle w' s_v' \rangle (z) \tag{2.22}$$

where $\varepsilon = c_p T_{\text{ref}}/L$, $\delta = 0.608$, and $\mu = 1 - \delta\varepsilon$, and s_{v0} is a reference virtual static energy. Due to the upward liquid water flux in the saturated cloudy air, there is a substantial jump in buoyancy flux at cloud base, and $\langle w' s_v' \rangle$ takes on the form

$$\langle w' s_v' \rangle (z) = \begin{cases} \langle w'h' \rangle - \mu L \langle w' q_t' \rangle, & 0 < z < z_b, \\ \beta \langle w'h' \rangle - \varepsilon L \langle w' q_t' \rangle, & z_b < z < z_i, \end{cases} \tag{2.23}$$

where $\beta \approx 0.5$ is a thermodynamic coefficient (Randall, 1980; Schubert et al., 1979a).

The entrainment efficiency, which includes terms to account for the evaporative enhancement of entrainment as well as sedimentation effects, is given by (see appendix B of Grenier and Bretherton, 2001)

$$A = a_1 \left(1 + a_2 \chi_s \left(1 - \frac{\Delta^i b_s}{\Delta^i b} \right) \exp\left(-a_{\text{sed}} w_{\text{sed}} / w_* \right) \right), \tag{2.24}$$

where

$$\Delta^i b_s = g\beta \left(\frac{\Delta^i h}{h} - \Delta^i q_t \right) \tag{2.25}$$

$$\Delta^i b = \frac{g}{s_{v0}} \Delta^i s_v, \tag{2.26}$$

and χ_s is the mixing fraction of above-inversion air that exactly saturates a mixture of cloudy and above-inversion air. It should be noted that the exponential term in (2.24) is not derived on physical grounds, but rather is chosen because it exhibits the required behavior

(i.e., larger sedimentation fall speed decreases the evaporative enhancement component of the entrainment efficiency).

In the case that $a_{\text{sed}} = 0$, the procedure from Appendix B of Bretherton and Wyant (1997) can be used to find w_e without resorting to iteration. However, with nonzero a_{sed}, w_* appears in the expression for A, and w_*^3 depends on w_e, so an iteration scheme is employed to ensure consistency between (2.18), (2.19), and (2.24). Be default, we choose $a_1 = 0.2$, $a_2 = 60$, and $a_{\text{sed}} = 9$.

2.1.5 Validity of MLM Assumptions

As in Turton and Nicholls (1987), the MLM self-diagnoses situations in which the underlying assumption of well-mixedness is likely to break down. The well-mixed assumption fails when negative subcloud buoyancy flux threatens to decouple the STBL. Following the physically realistic assertion that negative subcloud buoyancy will inhibit turbulent mixing across the full STBL, we define the buoyancy integral ratio, BIR, as

$$BIR = -\frac{\left(\int_0^{z_b} \langle w'b' \rangle dz\right)_{\langle w'b' \rangle < 0}}{\left(\int_0^{z_b} \langle w'b' \rangle dz\right)_{\langle w'b' \rangle \geq 0}}. \tag{2.27}$$

Decoupling is assumed to occur for BIR greater than some threshold, taken to be 0.15 following Bretherton and Wyant (1997).

2.1.6 Implementation

The MLM described in this section has been implemented in MATLAB. It consists of a collection of functions grouped together to form a "right-hand side" function, suitable for use with MATLAB's ODE solver functions. A MEX interface, provided by Dr. Peter Blossey, provides access to the RRTMG radiation code.

Rather than using a fixed grid for calculating precipitation, radiation, and entrainment, the needed grid is redefined at each time step and anchored such that there is always a grid point at the surface, z_b, and z_i. This sidesteps some of the numerical nuances discussed in the appendix of Bretherton and Wyant (1997). A number of logical switches are implemented to easily change the operating assumptions of the MLM. Most notable of these

is the option to use "full" moist thermodynamics in place of linearized thermodynamics. The primary differences between full and linearized thermodynamics are shown in Table 2.1. The use of the full moist thermodynamic expression is recommended when the goal is to compare against a high resolution model, or when perturbing the surface temperature. I have generally found it to be the case that using full moist thermodynamics in place of linearized thermodynamics does not qualitatively alter the model evolution, nor does it alter model *sensitivity* to perturbations, but it does somewhat affect the mean state, particularly the cloud base. Other available switches allow the use of LES-tuned cloud base precipitation and entrainment efficiency as described earlier. This MLM has been designed with the goal of allowing parameterizations to be swapped in and out easily. Thus, a new entrainment parameterization can be used by simply supplying the MLM "right hand side" function with the function handle of an alternate entrainment parameterization. This allows the comparison of a variety of entrainment closures with relative ease, as in Chapter 5.3.5.

The MLM was validated against the model of Uchida et al. (2010) using the DYCOMSII–RF01 test case. Appropriately configured, the model reproduces the results of Uchida et al. (2010). Unless otherwise noted, the MLM uses LES-tuned cloud base drizzle and full moist thermodynamics.

Table 2.1: Primary differences between linearized and full moist thermodynamic expressions in MLM.

Quantity	Linearized	Full
z_b	$\left(\frac{dq^*}{dz}\right)_u^{-1}\left((1+\gamma)\,\Delta^s q_t - \frac{\gamma}{L}\Delta^s h\right)$	$q^*(p(z_b), T(z_b)) = q_t$ (iteration)
χ_s	$\frac{q_{\ell i}}{-\Delta^i q_t + \gamma/(1+\gamma)\Delta^i h/L}$	Iteration
$\left(\frac{dq^*}{dz}\right)$	Constant, based on T_{ref},p_{ref}	Height-dependent[a]

[a] Height-varying p and ρ used to determine q_ℓ profile, but constant ρ_0 used in (2.7c).

2.2 SAMA LES

The LES used is version 6.7.5 of the System for Atmospheric Modeling (SAM), kindly supplied by Marat Khairoutdinov and documented by Khairoutdinov and Randall (2003) and Blossey et al. (2013). When referred to as "SAMA," the advection scheme of Blossey and Durran (2008) is used for the four advected scalars, liquid static energy $s_\ell = c_p T + gz - L(q_\ell + q_r)$, total non-precipitating water mixing ratio $q_t = q_v + q_\ell$, rain water mixing ratio q_r, and rain number concentration N_r. As noted by Blossey et al. (2013), the SAMA model version produces less numerical diffusion at the sharp, poorly resolved inversion that caps the STBL, resulting in higher and more realistic simulated stratocumulus liquid water paths. The cloud liquid water and temperature are diagnosed from the advected scalars using the assumption of exact grid-scale saturation in cloudy grid cells. The Khairoutdinov and Kogan (2000) scheme is used for conversion between cloud and rain water. Cloud droplet sedimentation is included following (2.16) with geometric standard deviation $\sigma_g = 1.2$. All LES runs presented in these studies were carried out by Dr. Peter Blossey.

2.3 CAM5

The National Center for Atmospheric Research (NCAR) Community Atmosphere Model (CAM), version 5.0 (hereafter referred to as CAM5) is the atmosphere model component of the state-of-the-art Community Earth System Model, version 1 (CESM1) coupled atmosphere-ocean GCM. Although our primary focus in the present work is on single-column modelling using CAM5 in it's single-column mode (SCAM5), a brief description of CAM5 is presented here. Further documentation is provided by Neale et al. (2010), with an implementation guide provided by Eaton (2010).

CAM5 couples a finite volume[4] dynamical core (represented by the operator D) to a physics parameterization suite (represented by the operator P). The dynamical core is responsible for time-evolving hydrostatic atmospheric flow prognostic equations for momentum, scalar advection, and hydrostatic balance. Subgrid physics processes are parameter-

[4] Also supported are spectral, Eulerian, and semi-Lagrangian dynamical cores, but they are not relevant to the current discussion.

ized, and are coupled to the dynamics through a "time-splitting" approach. For a generic variable ψ satisfying

$$\frac{\partial \psi}{\partial t} = D(\psi) + P(\psi), \tag{2.28}$$

a high-level representation of the time-split discretization and evolution process is to first apply the dynamic evolution equations to ψ at time t^n, then sequentially apply the physics parameterization:

$$\psi^{n+1} = \boldsymbol{P}(\boldsymbol{D}(\psi^n)), \tag{2.29}$$

where $\boldsymbol{P}$ and $\boldsymbol{D}$ are understood to be discretized operators corresponding to P and D that advance the state from ψ^n at t^n to ψ^{n+1} at t^n. Since P contains sources due to many physical processes, these are also time-split and applied sequentially. In CAM5, the physics parameterization suite consists of the following broad components (ordered by their order of operations within the model): Moist (precipitation) processes, clouds and radiation, surface modelling, and turbulent mixing. Each of these broad components are subdivided further. The processes most relevant to the current discussion are those relating clouds, radiation, and turbulence. The model physics components that bear most heavily on the present treatment[5] are listed below in order of how they are applied within the model.

1. **Asymmetric turbulence (Deep and shallow convection)**: Deep convection follows Zhang and McFarlane (1995), with additional modifications discussed in Neale et al. (2010). Shallow (cumulus) convection follows Park and Bretherton (2009), and operates after deep convection.

2. **Cloud macrophysics**: Cloud macrophysics computes the cloud fraction, determines the horizontal and vertical overlap of clouds, and converts water vapor to cloud condensate. At the current time, the only documented explanation of cloud macrophysics is in Section 4.7 of Neale et al. (2010), although further documentation is in preparation.

[5]Missing from this list is the treatment of aerosols, condensed phase optics, surface exchange formulations, dry adiabatic adjustment, and prognostic greenhouse gas treatment.

3. **Cloud microphysics**: The cloud microphysics scheme follows Morrison and Gettelman (2008) and Gettelman et al. (2008). This scheme provides diagnostic two-moment (i.e., both mixing ratio and number concentration) treatment of cloud condensate, rain, and snow. I discuss some details of the diagnostic precipitation scheme in Chapter 3.4.4.

4. **Radiative transfer**: Longwave and shortwave radiative transfer calculations use the RRTMG radiation code (Iacono et al., 2008; Mlawer et al., 1997).

5. **Moist turbulence (a.k.a., the PBL mixing scheme)**: Described in Bretherton and Park (2009a). This is a diagnostic TKE, first order K-diffusion scheme with entrainment parameterization. It explicitly represents cloud-radiation-turbulence interactions, and operates in any layer (not only the boundary layer) in which the moist Richardson number Ri is larger than a critical value Ri_c. In particular, this allows it to also handle decoupled boundary layers with separated turbulent regions driven from the surface and from the cloud top.

2.3.1 SCAM5

CAM5 supports operation in single-column mode, referred to as SCAM5. In this mode, the simulation occurs within a single, isolated vertical column, but using the full CAM5 physics suite. Boundary conditions that would be supplied by the evolution of neighboring columns in the full GCM must instead be supplied in the form of large scale forcings. For example, it is necessary to supply vertical profiles of the large scale vertical velocity, as well as relevant horizontal tendencies (e.g., s_ℓ and q_t), along with surface conditions[6]. In our implementation, horizontal winds, advective tendencies, vertical subsidence, SST and sea level pressure are held fixed. Furthermore, fixed LHF and SHF are used, though interactive surface fluxes may be used instead. An upwind differencing scheme is used for vertical advection.

[6] See Table 1 of Randall et al. (1996) for an illustrative list of data that must be specified in an SCM

For some classes of problems, the SCM provides an excellent analysis framework. It is computationally very cheap compared with a GCM, and hence allows many more simulations to be performed in a given time frame. It is a natural framework for making comparisons with LES, which can be forced identically (Zhu et al., 2005; Stevens et al., 2005; Zhang et al., 2013). Furthermore, because the dynamics are largely specified, it is useful for isolating the role of the physics parameterizations. These combine to make the SCM an ideal tool for model development and evaluation (Randall et al., 1996).

The aspects that make the SCM an excellent test for model development also mark its Achilles' heel. The SCM, by design, is unable to participate in column-to-column feedbacks that would occur in a full GCM. This can be particularly problematic when one is using the SCM to analyze a problem that is inherently tied to these feedbacks, and also means that parameterization testing in the SCM-framework is limited in its ability to diagnose such feedbacks. Thus, GCM tests are recommended before drawing conclusions about the global model behavior based solely on the SCM.

Two separate (but similar) versions of SCAM5 are used in Chapter 3. The first is `scamcpt_cam5_0_12`, branched from CAM5.0, and was supplied to us by Dr. Sungsu Park of NCAR. The second, `convect36_cam5_1_31`, branched off of CAM5.1, was supplied to us by Dr. Peter Caldwell of LLNL, in order to investigate the impact of additional sub-stepping of the macrophysics and microphysics schemes, as well as to analyze the behavior of the PDF-based macrophysics and microphysics.

Chapter 3

SENSITIVITY OF NEARLY NONDRIZZLING STRATOCUMULUS TO DROPLET CONCENTRATION IN SCAM

The sensitivity of LWP to cloud droplet concentration for a nondrizzling stratocumulus in SCAM5 is found to have the opposite sign to that expected based on LES and physically-motivated reasoning. This response is influenced by numerical and parametrization choices that modulate the strength of the underlying mechanisms responsible for the sensitivity.

Within the UW PBL scheme, the way in which cloud liquid is deduced internally to calculate the entrainment overstates the moisture in the top cloudy grid box and is insensitive to N_d. This results in a large evaporative enhancement to the entrainment efficiency that is relatively insensitive to the cloud top liquid water produced by the model as a whole. This can be corrected by using the q_ℓ profile input into the PBL scheme to calculate the turbulent mixing parameters, which results in decreased entrainment overall while allowing the modelled liquid water field to exert a stronger controlling influence on the derived entrainment rate.

Several additional issues, working together in concert, are also found to contribute to the overall incorrect sign of the SCAM5 LWP aerosol indirect effect. Model time-step and vertical resolution are both examined. With the relatively long default time step, the microphysics scheme excessively depletes liquid water. Coarse vertical resolution, particularly of cloud condensate, is also a contributing factor. However, neither increased vertical resolution nor a shorter time step is able to robustly correct the sign of the AIE in SCAM5 without also being coupled with the correction to the PBL scheme.

An inconsistency in the precipitation flux calculation in the microphysics scheme occasionally leads to a small amount of spurious surface precipitation, which acts as a moisture sink to the boundary layer and works against the expected LWP sensitivity. Correcting this can increase the LWP for lightly drizzling stratocumulus, particularly in cases where the

precipitation should all evaporate before reaching the surface. The numerical scheme used for vertical advection of the dynamics plays an important role in the mean-state behavior, which in turn affects the relative strengths of competing mechanisms. In this case, using a center-difference approach to vertical advection (the single-column default) results in a substantial increase in LWP, enhancing precipitation.

3.1 Introduction

Aerosols impact the Earth's radiation budget through both direct and indirect means. Aerosols directly impact the radiation budget by scattering and absorbing incoming solar radiation. Indirectly, aerosols impact the radiation budget through their influence on clouds.

The primary mechanism by which aerosol concentrations impact the microphysical structure of stratocumulus clouds is by altering the number of cloud condensation nuclei (CCN), and thereby the average cloud droplet concentration, N_d. For a given LWP, the average cloud droplet size is higher when N_d is lower. Since aerosols act as CCN, cloud droplet concentration can be used as a proxy for aerosol concentration, and the aerosol indirect effect (AIE) assessed by considering the radiative response of clouds to changes in N_d.

There are a number of compounding identified mechanisms that contribute to the AIE. These act in concert, and as they combine with different magnitudes and/or different signs, the net AIE is sensitive to the atmospheric conditions. It is no surprise, then, that the AIE is one of the leading uncertainties in the response of clouds to climate change (Randall et al., 2007).

The first identified AIE, is attributed to Twomey (1974, 1977). Two macrophysically identical clouds (i.e., clouds with the same LWP) but different droplet concentrations will have a different albedo. Higher N_d corresponds to a larger number of droplets with smaller size, increasing the net surface area of the liquid water within the cloud, thereby reflecting more incoming solar radiation resulting in net cooling relative to a cloud with lower N_d. This effect is commonly referred to as the first aerosol indirect effect, the Twomey effect, or the cloud albedo effect.

Another expression of aerosol indirect effects are the so-called "cloud lifetime effects[1]," in which microphysical physical differences lead to macrophysically different clouds (Randall et al., 2007). The most relevant of these to marine stratocumulus is the way in which precipitation and cloud droplet sedimentation are affected by droplet concentration. Generally, increasing N_d suppresses precipitation (Albrecht, 1989), while decreasing N_d enhances precipitation, due to the larger terminal fall speed of larger droplets (i.e., larger cloud droplets will precipitate more effectively due to enhanced accretion processes). Thus, a second AIE is due to the way in which aerosols impact precipitation, which in turn impacts the LWP and thereby the optical depth of a cloud.

On the global scale, Quaas et al. (2009) found that satellite measurements exhibit a positive relationship between LWP and aerosol optical depth (τ_a), as well as a positive relationship between cloud fraction and τ_a. When compared against a collection of GCMs, the GCMs were shown to drastically overestimate the LWP response to τ_a (generally by more than a factor of two), and to underestimate the cloud fraction response. Overall, GCMs were shown to overestimate the SW cooling effect of the AIE. Wang et al. (2011) showed that using a multi-scale modeling framework (MMF), which replaced the CAM5 GCM's traditional cloud parameterization suite with a cloud-resolving model, more than halved the SWCRE from -1.79 W m^{-2} to -0.77 W m^{-2} between pre-industrial and present-day forced climates relative to the default CAM5 model. This was attributed primarily to a much smaller LWP increase in the MMF than in the default CAM5. Thus, there is evidence that GCM parameterization of cloud-aerosol interactions over-emphasize the increase in LWP due to increased aerosol concentrations.

At the local level, the response of boundary layer LWP to increasing N_d is complicated, and may exhibit opposite sign depending on the circumstances. Coakley and Walsh (2002) showed using ship track observations that increased aerosols in ship-tracks could either increase or decrease the liquid water amount. Wood (2007) argued that cloud base height is a good predictor of the sign of the second AIE. Ackerman et al. (2004) demonstrated with a LES that the sign of the response of LWP to increasing N_d depends on the amount

[1]The cloud lifetime effect is also referred to as the second aerosol indirect effect, or the Albrect effect.

of surface precipitation and moisture contained in the overlying air. When precipitation is heavy enough that a sufficient amount reaches the surface, this acts as a sink of liquid water that, all else being equal, decreases the LWP and dries out the boundary layer. In this regime, LWP increased with N_d. However, once surface precipitation becomes negligible, LWP is seen to reach a maximum before *decreasing* with higher N_d. A mechanism invoking cloud droplet sedimentation was provided by Ackerman et al. (2004), and later refined by Bretherton et al. (2007).

The authors used a LES of a nondrizzling, nocturnal stratocumulus to show that increasing N_d decreased the cloud top sedimentation. This leaves the entrainment zone with additional moisture, thereby increasing the potential for mixtures of warm, dry air (from the free troposphere) with cool, moist cloudy air to sink more readily due to evaporative cooling. This increased potential for evaporative enhancement increases the nondimensional entrainment efficiency A, meaning that a given amount of turbulent kinetic energy (TKE) generates more entrainment mixing. For sufficiently dry overlying air, increased entrainment causes boundary layer to deepen, warm, and dry, resulting in a thinner cloud and decreased LWP.

This mechanism was explored further in Uchida et al. (2010), where it was demonstrated that a MLM with entrainment efficiency and vertical precipitation profile tuned to LES reproduced decreased LWP in response to increased N_d in a nocturnal, nondrizzling stratocumulus. It is this mechanism that is also the focus of the current chapter.

3.1.1 Aerosol Indirect Effects in SCAM

Simulations of a composite Lagrangian Sc-Cu transition (Sandu and Stevens, 2011) with fixed cloud droplet concentrations provide evidence that the AIE is not being captured correctly in SCAM5. This case was the subject of a recent, still unpublished, international SCM and LES comparison by the Global Atmospheric System Study (GASS). I compared SCAM5 simulations of this case with an identically forced LES. Consider the time-height plots of cloud fraction in the left panel of Figure 3.1. During the first day of simulation, the LES maintains a full stratocumulus deck (bottom row) with nearly 100% cloud cover, and

furthermore exhibits the classic LWP response (right panel). Using either of two different turbulence parametrization schemes, SCAM5 similarly maintains a stratocumulus deck and represents key features of the transition well, but shows the opposite sensitivity of LWP to N_d.

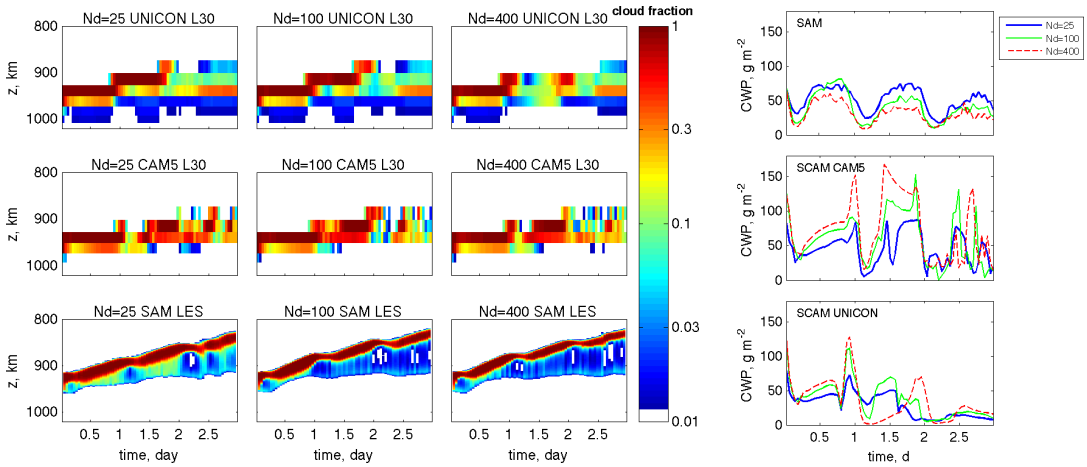

Figure 3.1: SAM LES and SCAM5 Lagrangian simulations of a Sc-Cu transition. SCAM5 simulations are performed with both standard CAM5 physics and with the UNICON convection parameterization. Left: Time-height series of cloud fraction. Right: Time series of LWP.

The goal of the current chapter is to analyze this phenomenon, and to determine relevant factors that contribute to the opposite sign of the LWP sensitivity to droplet concentration in SCAM5 relative to the LES. To isolate and explore the relevant factors, I use the DYCOMSII–RF01 test case, which allows me to hone in on the relevant entrainment-sedimentation feedback by simulating a cloud that is nearly non-precipitating at the surface. Fixed surface latent and sensible heat fluxes remove any possibility of surface flux feedbacks obscuring the entrainment-driven response, and the use of idealized radiation that is insensitive to cloud droplet size eliminates direct aerosol-cloud radiative feedbacks.

Sec. 3.2 provides a brief overview of the implementation of the DYCOMSII–RF01 test case. In Sec. 3.3 the LES results for the DYCOMSII–RF01 test case are discussed as a base line for identifying the desired behavior of SCAM. Sec. 3.4 explores the default behavior of SCAM5 for fixed droplet concentrations of 25 cm^{-3}, 100 cm^{-3}, and 400 cm^{-3}, along with a variety of additional simulations that demonstrate the many ways in which numerical and

parametrization features exert an influence on the feedback. The results are summarized in Sec. 3.6.

3.2 Simulation setup for DYCOMSII-RF01

The DYCOMSII–RF01 test case is derived from a nocturnal, non-drizzling stratocumulus, measured during a field campaign 300 km off the coast of San Diego (Stevens et al., 2003). This case study has been the subject of both LES (Stevens et al., 2005) and SCM (Zhu et al., 2005) intercomparisons. Here it is implemented both in SCAM5 and the SAM LES (both of which are described in Chapter 2) following the specifications of Zhu et al. (2005), to which the reader is referred for details not included here.

The case features idealized nocturnal radiation following (Zhu et al., 2005) that depends on the boundary layer liquid water content but is otherwise independent of temperature or water vapor. Specified $LHF = 115$ W m^{-2} and $SHF = 15$ W m^{-2} are used instead of interactive surface fluxes, and fixed N_d is used. To keep the overlying temperature and moisture profiles from drifting in SCAM5, moisture and temperature source terms were turned off for all levels for which $q_t < 6$ g kg^{-1}.

The SAM LES uses a doubly periodic horizontal grid with 128 points and 35 m grid spacing in each horizontal direction, and a vertical domain consisting of 256 points stretching from the surface to approximately 2270 m, with horizontal resolution of 5 meters within the region of the boundary layer where the inversion may lie, and gradually stretched near the surface and top of the domain.

3.3 Overview of LES results

The focus of this analysis is to interpret the AIE in SCAM5. In doing so, it is informative to first consider a similarly-forced LES. The LES used in this study is the System for Atmospheric Modelling (SAM), documented in Khairoutdinov and Randall (2003), and further described in Chapter 2.2. SAM was previously used by Uchida et al. (2010) in conjunction with a MLM to show that the sensitivity of a nocturnal stratocumulus to droplet concentration exhibited by the LES can be reproduced by an appropriately-tuned MLM. Thus, mixed-layer arguments are sufficient for explaining and interpreting the sedimentation-entrainment

feedback that drives the LWP sensitivity to droplet concentration.

Figure 3.2 shows the time-height series of cloud fraction using fixed droplet concentrations of $N_d = 25$ cm^{-3}, $N_d = 100$ cm^{-3}, and $N_d = 400$ cm^{-3}. In each case, the simulated boundary layer is fully cloud-covered (i.e., the integrated cloud fraction is nearly 1). The cloud top increases as a function of N_d, indicating that $N_d = 25$ cm^{-3} has the smallest average entrainment rate while $N_d = 400$ cm^{-3} sustains the largest entrainment rate, in line with the physically-motivated argument that cloud droplet sedimentation drives the entrainment sensitivity to droplet concentration. Similarly, the cloud thickness decreases with increasing N_d, which is also consistent with increasing entrainment rate.

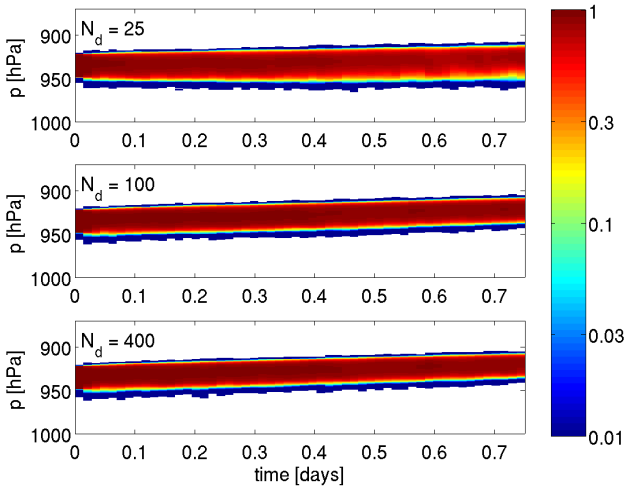

Figure 3.2: Cloud fraction from LES DYCOMSII–RF01 simulation.

This is reflected in Figure 3.3, which shows the mean LWP for each simulation, compared with the default SCAM simulations. For the LES, the mean LWP diverges amongst the three cases very early, with the $N_d = 25$ cm^{-3} LWP substantially higher than the $N_d = 100$ cm^{-3} and $N_d = 400$ cm^{-3} cases. By contrast, the SCAM simulations show the opposite sensitivity of LWP to N_d. The $N_d = 25$ cm^{-3} LES simulation is the only one with significant cloud base precipitation (Figure 3.4), and even in this case the surface precipitation is negligible.

The LES 4–8 hour vertical mean profiles shown in Figure 3.4 shed further light on the boundary layer structure. The right column shows that the moist-adiabatically conserved

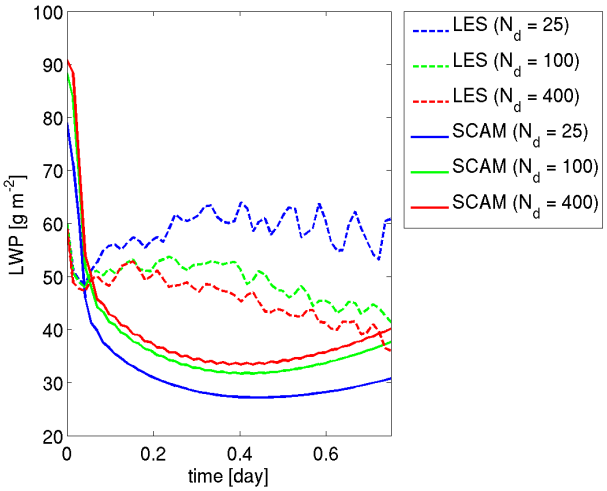

Figure 3.3: LWP from LES (dashed) and SCAM5 (solid) DYCOMSII–RF01 simulations.

variables θ_ℓ and q_t are nearly uniform below the capping inversion, indicating the boundary layer can be well-approximated by a mixed layer.

3.4 SCAM aerosol indirect effect simulations

In the native CAM GCM, the horizontal grid spacing in the subtropics is approximately 100 km (1 degree latitude by 1 degree longitude). Due to the coarse nature of the grid, many of the physical processes (e.g., cloud macrophysics, cloud microphysics, and turbulent mixing) are parametrized. These parametrizations are responsible for a substantial amount of the uncertainty and intermodel spread in global climate sensitivity to a given greenhouse gas increase (Bony and Dufresne, 2005). Recently there has been growing appreciation for the role played by interactions between parametrizations in this uncertainty (e.g., see Zhang and Bretherton, 2008).

I will show, similarly, that several parametrizations bear on the magnitude and sign of the aerosol indirect effects for nondrizzling stratocumulus. SCAM5 simulations presented here use two different versions of the model. The first configuration, branched off of CAM5.0, is `scamcpt_cam5_0_12` and was provided for use in this analysis by Dr. Sungsu Park. A second version, `convect36_cam5_1_31`, branched from CAM5.1, was provided by Dr. Peter

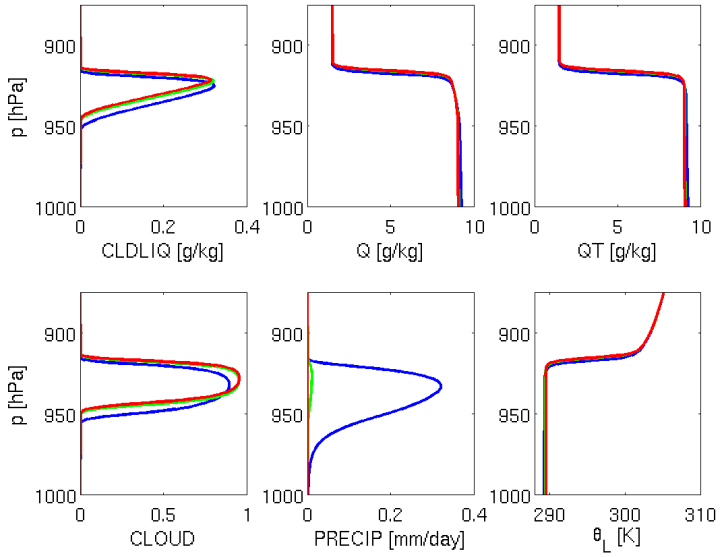

Figure 3.4: Select 4–8 hour vertical mean profiles of LES-simulated fields. The color-scheme is as in Figure 3.3. Top left: cloud liquid water mixing ratio. Top center: water vapor mixing ratio. Top right: total water mixing ratio. Bottom left: Cloud fraction. Bottom middle: Precipitation flux. Bottom right: Liquid potential temperature.

Caldwell in order to investigate the impact of additional sub-stepping of the macrophysics and microphysics, as well as to analyze the behavior of the PDF-based macrophysics and microphysics.

I refer to CAM5 variable names throughout this chapter. For clarity and convenience, these are listed in Table 3.1.

3.4.1 Default Configuration

In its default configuration, SCAM5 uses a grid with 30 vertical levels (hereafter denoted as "L30"), and operates with a time step of $\Delta t = 1200$ s. Seven layers are below 850 hPa, with grid spacing of approximately 140 meters closest to the surface that gradually stretches. The vertical grid below 700 hPa is shown in Figure 3.5.

As in the LES, SCAM5 simulates full cloud cover for each of the three fixed droplet cases (Figure 3.6). Due to the coarse resolution, it is harder to see that the $N_d = 25$ cm^{-3}

Table 3.1: CAM5 model output fields that are referred to in the text. For further information, consult Eaton (2010).

Field	Description [units]
CLDLIQ[a]	Liquid water content (LWC) [kg/kg]
CLOUD	Cloud fraction
LWCF	Longwave cloud forcing [W m^{-2}]
MGFLXPRC[b]	Diagnostic precipitation flux at cell interfaces [kg m^{-2} s^{-1}]
PRECT	Total surface precipitation [m s^{-1}]
PRECTFLX	Precipitation flux at cell interfaces calculated following (3.9)
ql_aft_PBL	LWC after PBL scheme [kg/kg]
Q	Specific humidity [kg/kg]
QT[c]	Total water mixing ratio [kg/kg]
SL	Liquid static energy [J/kg]
SWCF	Shortwave cloud forcing [W m^{-2}]
TGCLDLWP	Total grid-box cloud liquid water path [kg m^{-2}]
UW_ql	LWC internally diagnosed within PBL scheme [kg/kg]

[a] CLDLIQ is the LWC just before the execution of the PBL scheme.

[b] MGFLXPREC at interface k is given by $\rho_k q_r'(k) V_q(k) F_{\mathrm{cld}}(k)$ (see Sec. 3.4.4).

[c] Note, QT = ql_aft_PBL + Q $\neq$ Q + CLDLIQ.

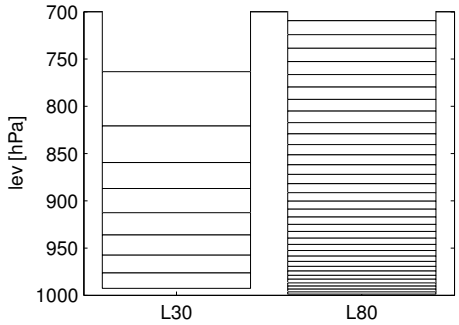

Figure 3.5: Vertical resolution in both the 30 level (L30) and 80 level (L80) configurations of SCAM5.

case is entraining at the slowest rate, while $N_d = 400$ cm^{-3} entrains at the highest rate, since the cloud layer is deepening slowly enough that it does not jump to the next grid level. However, since entrainment is associated with heating and drying the boundary layer, it is clear that the $N_d = 25$ cm^{-3} entrains slowest of the three because the lowest layer of the cloud (in the $p = 976$ hPa level) persists the longest, and at any given time the cloud amount in the $p = 957$ hPa layer is the largest in the top panel.

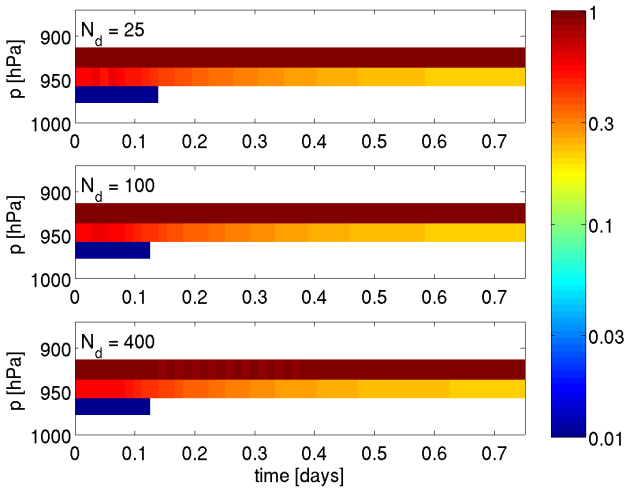

Figure 3.6: Cloud fraction from SCAM5 DYCOMSII–RF01 simulation.

Although the $N_d = 25$ cm^{-3} case is entraining at the slowest rate, the LWP is *smallest*

for that case, and increases with droplet concentration (Figure 3.3), opposite to the expected sensitivity. Thus, we are presented with a paradox – how does SCAM5 simulate less cloud condensate despite generating lower entrainment for low droplet concentrations?

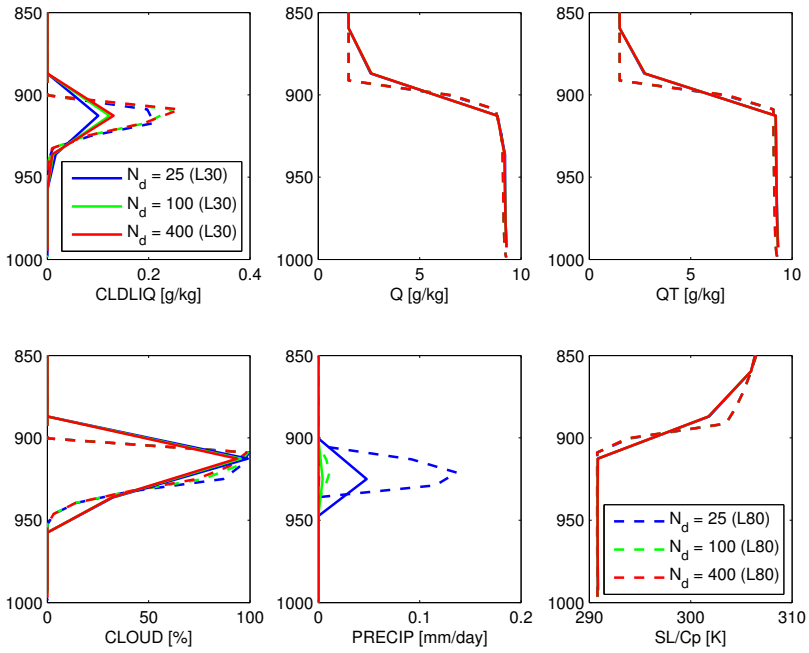

Figure 3.7: Select 4–8 hour vertical mean profiles of SCAM-simulated fields. The color-scheme is as in Figure 3.3, with solid lines showing the default L30, $\Delta t = 1200$ s simulations and dashed lines showing the L80, $\Delta t = 300$ s profiles. *Top left:* cloud liquid water mixing ratio (CLDLIQ). *Top center:* specific humidity (Q). *Top right:* total water mixing ratio (QT). *Bottom left:* Cloud fraction (CLOUD). *Bottom middle:* Diagnostic precipitation flux (MGFLXPRC). *Bottom right:* Liquid static energy (SL).

The vertical profiles averaged from 4–8 hours of simulation time are shown in Figure 3.7 for both L30 and L80 simulations. The right column shows that the total water mixing ratio q_t and the liquid static energy s_ℓ are both exceptionally well-mixed, suggesting that mixed-layer arguments (see Chapter 2.1) should apply.

Closer inspection reveals that the boundary layer q_t is (slightly) higher for lower droplet concentration, consistent with lower entrainment, but s_ℓ is slightly higher, which is *not* consistent with lower entrainment. Despite the slightly higher q_t for $N_d = 25$ cm^{-3}, the cloud shown in the top left panel of Figure 3.7 contains significantly less liquid water.

Furthermore, the cloud cover is highest for the case with the least cloud liquid, since cloud cover is tied to the specific humidity in the model. The combination of these features indicates that mixed-layer arguments, though they apply conceptually, are not the only factors at play in the context of the CAM5 parametrization.

The $N_d = 25$ cm^{-3} case is the only one which precipitates significantly (top center panel), and even in this case the precipitation does not reach the surface. The cloud base precipitation is also somewhat weaker than in the LES. Thus, although precipitation acts as a sink of cloud water, it is not an overall moisture sink in the boundary layer, and should not dominate the overall entrainment-sedimentation feedback.

The remaining subsections detail a series of investigations intended to shed light on the parametrization issues responsible for the incorrect modelling of aerosol indirect effects in SCAM5 for weakly-drizzling stratocumulus.

3.4.2 Evaporative Enhancement Coefficient in the PBL Scheme

The argument presented by Bretherton et al. (2007) states that cloud droplet sedimentation impacts the LWP primarily through its impact on the entrainment efficiency by decreasing the evaporative enhancement factor. In the CAM5 PBL scheme, the evaporative enhancement coefficient, `evhc`, is calculated as

$$\text{evhc} = 1 + \exp\left(-a_{\text{sed}} w_{\text{sed}}/w^*\right) a_2 a_3 L_v \frac{q_\ell^{\text{eff}}}{\Delta^i s_\ell}. \tag{3.1}$$

By default, $a_{\text{sed}} = 0$, $a_2 = 30$, $a_3 = 0.8$, q_ℓ^{eff} the liquid water in the top grid level beneath a capping inversion, and $\Delta^i s_\ell$ the inversion jump of s_ℓ across two grid levels. It is clear from the solid lines in Figure 3.8 that the entrainment efficiency is surprisingly insensitive to droplet concentration in the default configuration of SCAM, despite the substantial differences in the q_ℓ profiles shown in Figure 3.7.

The cause of this insensitivity can be traced to the representation q_ℓ^{eff} within the PBL scheme that is used to calculate `evhc`. As described in Bretherton and Park (2009b), turbulent diffusivities, including an effective "entrainment diffusivity," are determined iteratively for use in an implicit backward-Euler scheme. Specifically, "final state" profiles of the moist-

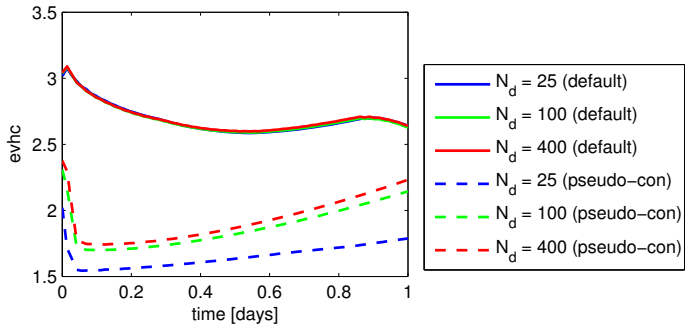

Figure 3.8: Evaporative enhancement coefficient in SCAM default configuration (solid) and using pseudo-conservative diffusion (dashed).

adiabatic conserved s_ℓ and q_t variables are predicted from the incoming (initial) state, and diffusivities are deduced from the final state. This procedure is iterated several times until the diffusivities and final states are considered to have converged.

The diffusivity coefficients, as well as the entrainment efficiency, depend on q_v, q_ℓ, and q_i which mush be backed out from the final s_ℓ and q_t profiles because they are *not* individually conserved quantities. In the default implementation of the PBL scheme, this internally specified q_ℓ is deduced at each grid level as the amount of q_t in excess of the saturation vapor pressure q^*, where q^* is determined from s_ℓ by assuming either 100% or 0% cloud fraction. This approach has the benefit of being straightforward to implement with minimal added computational cost, but comes with a substantial downside: it does not necessarily bear any resemblance to the procedure used in the other physical parametrization packages (e.g., cloud macrophysics and microphysics). This can (and does, in the present study) introduce a substantial bias.

The essential entrainment-sedimentation feedback necessarily depends on the behavior of multiple physical parametrizations working in concert. To correctly produce the desired behavior, the parametrizations should make consistent assumptions whenever possible. Figure 3.9 shows the time-height series of the cloud condensate before, during, and after the application of the PBL turbulence scheme for both the $N_d = 25$ cm^{-3} and $N_d = 100$ cm^{-3} cases. The top row shows CLDLIQ, which is q_ℓ directly after the cloud microphysics scheme has been applied but before the PBL scheme has acted. This is also the CLDLIQ that is

recorded in the SCAM5 model output history file. The second row shows UW_ql, which is the q_ℓ used internally within the PBL scheme to calculate the diffusivities and entrainment rate. By comparing this against the top row, we see that UW_ql is concentrated at one grid level. Furthermore, that grid level contains more condensate than CLDLIQ by a factor of almost three. Despite the differences in CLDLIQ between the $N_d = 25$ cm^{-3} (left column) and $N_d = 100$ cm^{-3} (right column) cases, UW_ql is nearly identical, showing that the assumed moisture profile is insensitive to droplet concentration. This is because UW_ql is deduced from s_ℓ and q_t without any reference to quantities that depend on droplet concentration, the only way N_d is able to feed back into the process is by inducing a difference in s_ℓ or q_t. From Figure 3.7, such differences are slight despite the substantial role precipitation (which *does* depend on N_d) plays in setting q_ℓ. The intention of UW_ql is to represent the cloud condensate of the final, diffused state. However, the bottom row of Figure 3.9 shows that the resulting q_ℓ after applying the PBL scheme (ql_aft_PBL) bears little resemblance to either CLDLIQ or UW_ql.

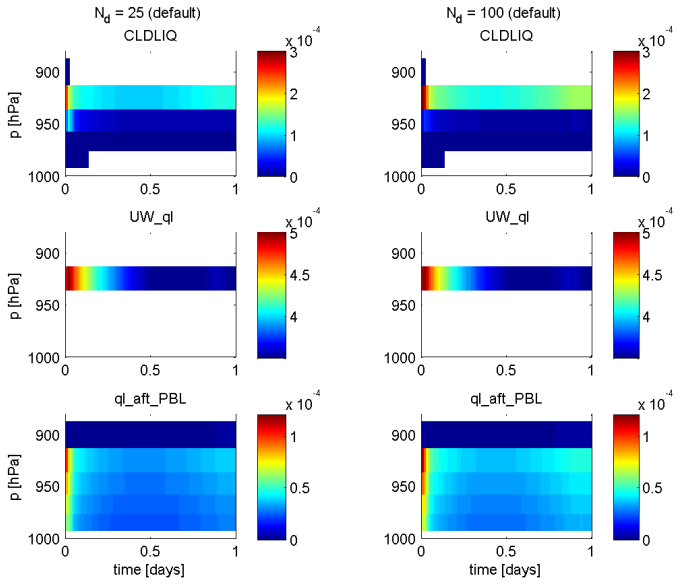

Figure 3.9: Cloud liquid profiles before the PBL scheme operates (top), during the PBL scheme for calculating evhc (middle), and after the PBL scheme operates for the default $N_d = 25$ cm^{-3} and $N_d = 100$ cm^{-3} cases.

To test the role the choice of UW_ql plays in the entrainment efficiency, I perform a simulation using "pseudo-conservative" diffusion, in which q_ℓ is not diffused – i.e., the tendency of q_t in the PBL scheme is equal to that of q_v, and q_ℓ is held constant throughout the PBL scheme. This entrainment efficiency is shown as the dashed lines in Figure 3.8.

This highlights two consequences of the standard implementation. First, the additional liquid water in the top layer during the default operation results in a substantially higher entrainment efficiency than would be sustained by the incoming q_ℓ. Second, since N_d plays a substantial role in the formation of precipitation, using q_ℓ from the microphysics translates into a significant difference in the entrainment efficiency between $N_d = 25$ cm^{-3} and $N_d = 100$ cm^{-3} that is more in line with expectations from the LES.

Considering the failing of the current implementation, the most direct and straightforward solution is to use the pseudo-conservative diffusion assumption to specify diffusivities in the PBL. Practically speaking, this amounts to leaving q_ℓ untouched by the PBL scheme, so that CLDLIQ, UW_ql, and ql_aft_PBL are identical. This is an imperfect solution, but in the absence of a clear, consistent way to specify the cloud fraction and cloud water content in accordance with the other physical parametrizations to determine UW_ql, it offers a clear improvement in capturing the underlying sensitivity of entrainment rate to cloud LWC.

3.4.3 Sensitivity to spatial and temporal resolution

Model behavior is somewhat exacerbated by the coarse resolution required by global model runs. Since the parameterizations utilize a process-splitting approach, a uniformly large time step introduces large discretization errors for processes that act on a fast time scale[2] To assess the role of spatial and temporal resolution in modelling the sensitivity of non-drizzling stratocumulus to droplet concentration, I vary the time step and vertical resolution in a variety of simulations, described in the following subsections.

[2]It should be noted that some processes, such as cloud microphysics, use a substepping approach to reduce errors resulting from long time step (Morrison and Gettelman, 2008).

Vertical Resolution

To investigate the role of vertical resolution in the SCAM5 AIE, I perform each of the L30 simulations with 80 vertical levels (hereafter denoted by "L80") and 300 s time step. The 80 levels are preferentially spaced to increase resolution in the boundary layer. See Figure 3.5 for a visual representation of the L30 vs. L80 resolution.

Of perhaps greatest relevance to this study, one would expect that coarse resolution would result in smaller LWP[3] and less cloud top water, since q_ℓ increases approximately linearly from cloud base for typical boundary layer clouds (Wood, 2012). Smaller q_ℓ at cloud top implies less evaporative enhancement in the entrainment efficiency, as well as smaller droplets and less sedimentation at cloud top. Thus, one would expect that the higher resolution runs would better capture the role of cloud droplet sedimentation in depleting q_ℓ in the top cloud layer.

Mean profiles for the L80 simulations are shown as dashed lines in Figure 3.7. The top left panel shows more mean cloud liquid in the L80 simulations than their L30 counterparts, but the sensitivity is the same, with $N_d = 25$ cm^{-3} showing the lowest LWP and $N_d = 400$ cm^{-3} the highest. The right two panels show that both the L80 and L30 simulations remain well-mixed, with very similar mixed-layer values of s_ℓ and q_t. The larger LWP in the L80 case supports higher precipitation (bottom middle panel), with $N_d = 25$ cm^{-3} again the only one showing any significant drizzle, all of which evaporates well above the surface. Thus, higher resolution does little to alter the sensitivity of LWP to N_d, and simulates a qualitatively similar boundary layer. Although not shown here, the L80 simulations generate a small amount of spurious surface precipitation that contributes minimally to the overall LWP sensitivity. This will be discussed in detail in Sec. 3.4.4.

Time step

Figure 3.10 shows the 6-12 hour mean LWP for a range of time steps with L30 resolution, both in the default SCAM5 configuration (left) and using psuedo-conserved diffusion (right).

[3]Imagine two identical clouds with a grid superimposed on them, and simply interpolate q_ℓ to the grid points. A coarse grid will over emphasize liquid water below cloud base and undercount cloud top water content, while higher resolution will better capture the water near the cloud top.

Generally, the mean LWP increases with decreasing time step. The sensitivity of the mean LWP to time step is quite substantial. Presumably, this is due primarily to the relatively short time scale on which cloud microphysics operate. Using a long time step will tend to remove a larger amount of liquid water than would a series of smaller time steps. This was verified through a series of simulations with greater microphysical substepping that showed an increase in LWP with additional substeps, despite using the same dynamics time step.

In the default configuration, the sensitivity of LWP to N_d maintains the same incorrect sign regardless of time step (with the unexplained exception of the 100 s time step). Using pseudo-conservative diffusion, however, the sensitivity improves systematically and robustly with decreased time step, and is able to recover the correct sign of the sensitivity with short enough time steps. Other model configurations that do not include turning off q_ℓ diffusion are able to sporadically recover the appropriate sign, but not robustly – there are only isolated combinations that produce the correct AIE (see Table 3.2), suggesting that the mechanisms by which they are able to affect that change are not fundamental.

Thus, a shorter time step is necessary, but not sufficient, to uncover the correct sign of the AIE for the present case.

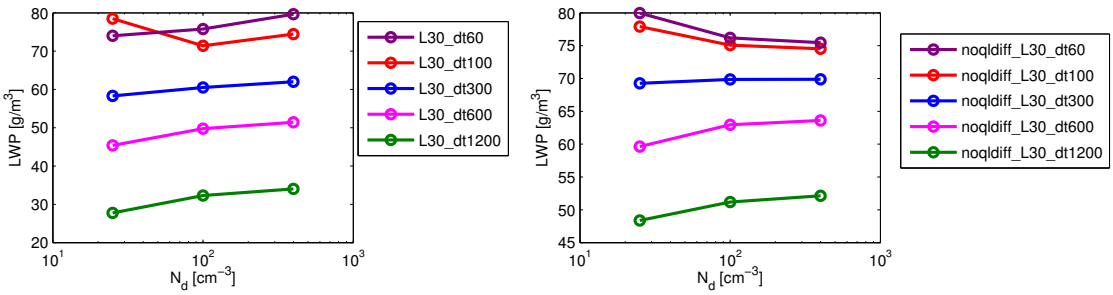

Figure 3.10: Impact of model time step on SCAM5-simulated LWP in the L30 configuration. *Left:* Default configuration. *Right:* Using pseudo-conservative diffusion.

3.4.4 Role of spurious surface precipitation

The Morrison-Gettelman microphysics scheme (hereafter referred to as MGM) uses an implicit, backward-Euler-like predictor-corrector scheme to diagnose the column precipitation

profile (Morrison and Gettelman, 2008). In 80 level runs, it was discovered that there was unphysical surface precipitation being recorded in the PRECT model output variable while the diagnosed precipitation flux was zero well above the surface. The magnitude of this unphysical spurious precipitation was on the order of less than 0.1 mm/day, but this is able to account for a loss of several g m^{-2} of LWP in precipitating cases during the simulation, an amount that is significant for the effect being investigated.

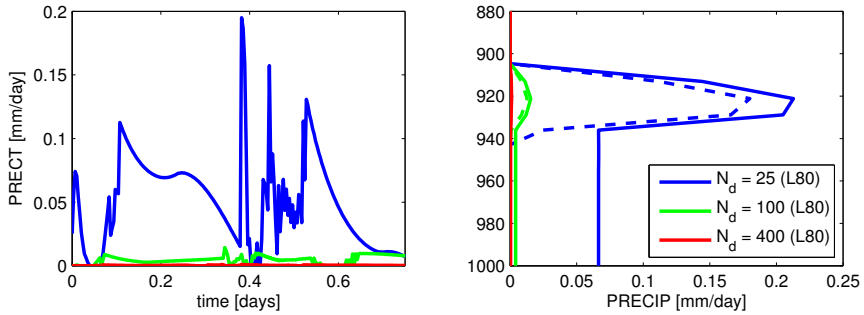

Figure 3.11: *Left:* Surface precipitation flux for the L80, dt300 EntrSed simulation with $a_{\text{sed}} = 9$ in (3.1). *Right:* Mean precipitation flux profile during 4–8 hours of model simulation time. Dashed lines indicate the diagnostic flux MGFLXPRC, and solid lines show PRECTFLX, the precipitation flux deduced from integrating the precipitation flux tendencies, determined at each interface k as the partial sum from 1 to k of (3.9).

This is illustrated by Figure 3.11, which shows L80 simulations for which $a_{\text{sed}} = 9$ in (3.1)[4]. The surface precipitation measures nonzero throughout much of the simulation for the $N_d = 25$ cm^{-3} case (left panel), but this is not reflected by the diagnosed mean vertical precipitation flux profile (MGFLXPRC) in the right panel, which goes to zero at the surface. MGFLXPRC (dashed lines) is evaluated directly by diagnosing the flux at interface k from $\rho_k q_r(k) V_q(k)$, where ρ_k is air density in cell k, q_r the rain mixing ratio, and V_q the fall speed. This differs from PRECTFLX (solid lines), calculated in the same manner as PRECT by integrating the precipitation source and sink terms, which is seen to be nonzero at the surface. The difference between these two profiles provides the clue to the root of the problem, as discussed in the remainder of this section.

[4]This so-called EntrSed simulation is discussed further in Sec. 3.4.6. Similar spurious surface precipitation occurs in the default L80 case, but is more clearly demonstrated with the EntrSed simulation.

Rain microphysics

To understand the origin of the spurious precipitation signal, I must briefly outline the way that precipitation is diagnosed in the CAM5 MGM, which is somewhat different than the presentation in Morrison and Gettelman (2008). Following the convention of CAM5, I assume throughout that the vertical index k increases *downward* from the top of atmosphere. The starting point for the rain mixing ratio q_r and number concentration N_r are the budget equations

$$\frac{\partial q_r}{\partial t} = \frac{1}{\rho}\frac{\partial \left(V_r \rho q_r\right)}{\partial z} + S_r \tag{3.2a}$$

$$\frac{\partial N_r}{\partial t} = \frac{1}{\rho}\frac{\partial \left(V_N \rho N_r\right)}{\partial z} + S_N, \tag{3.2b}$$

where z is the height, V_r the mass-weighted terminal fall speed of rain droplets, V_N the number-weighted terminal fall speed of rain droplets, and S_q and S_N the sum of all source and sink terms for q_r and N_r, respectively. These source and sink terms can, in general, depend on q_r and N_r at the cell interfaces or cell-center. In CAM5, the precipitation is diagnostic, so the left hand sides of (3.2) are taken to be zero, and the problem reduces to spatially integrating (3.2) downward from the top model level.

Furthermore, the assumed Marshall-Palmer (Marshall and Palmer, 1948) size distribution provides the following constraint relation for q_r and N_r:

$$\phi(D) = N_0 e^{-\lambda D}, \tag{3.3}$$

where the slope parameter λ and intercept parameter N_0 are given by

$$\lambda = \left(\frac{\pi \rho_w N_r'}{q_r'}\right)^{1/3} \tag{3.4}$$

$$N_0 = N_r' \lambda. \tag{3.5}$$

Here D is the rain droplet diameter, $\rho_w = 1000$ kg m^{-3} the density of liquid water, and

primes indicate local values (as opposed to grid-mean values) of N_r and q_r, such that $N_r = F_{\rm cld} N_r'$ and $q_r = F_{\rm cld} q_r'$ for cloud overlap fraction $F_{\rm cld}$. From the distribution (3.3), the mass- and number- weighted terminal fall speed are calculated as

$$V_q = c_q \lambda^{-b} \tag{3.6a}$$

$$V_N = c_N \lambda^{-b}, \tag{3.6b}$$

where c_q and c_N are given by equations (17) and (18) in Morrison and Gettelman (2008) and $b = 0.8$ is an empirically chosen parameter. The discretization of (3.2) at grid level k is written as

$$\rho_k q_r'(k) V_q(k) F_{\rm cld}(k) = \rho_{k-1} q_r'(k-1) V_q(k-1) F_{\rm cld}(k-1) + \rho_k \Delta z_k S_q(k) \tag{3.7a}$$

$$\rho_k N_r'(k) V_N(k) F_{\rm cld}(k) = \rho_{k-1} N_r'(k-1) V_N(k-1) F_{\rm cld}(k-1) + \rho_k \Delta z_k S_N(k). \tag{3.7b}$$

Equation (3.7) forms an implicit scheme where the source terms $S_{q,N}$ are computed based on estimates of $q_r'(k)$ and $N_r'(k)$. The updating scheme can be summarized by the following steps:

1. Calculate $F_{\rm cld}(k)$, and assume $V_{(q,N)}(k) = V_{(q,N)}(k-1)$.

2. Estimate $S_q^*(k)$ and $S_N^*(k)$ from $q_r'(k-1)$, $N_r'(k-1)$.

3. Use (3.7) with $S = S^*$ to estimate $q_r^*(k)$ and $N_r^*(k)$.

4. Use (3.4) to calculate estimated fall speed $V_q^*(k)$ and $V_N^*(k)$.

5. Calculate the final value of $S_q(k)$ and $S_N(k)$ from $q_r^*(k)$ and $N_r^*(k)$.

6. Use (3.7) to calculate $q_r'(k)$ and $N_r'(k)$:

$$q_r'(k) = \frac{\rho_{k-1} q_r'(k-1) V_q(k-1) F_{\rm cld}(k-1) + \rho_k \Delta z_k S_q(k)}{\rho_k V_q^*(k) F_{\rm cld}(k)} \tag{3.8a}$$

$$N_r'(k) = \frac{\rho_{k-1} N_r'(k-1) V_N(k-1) F_{\rm cld}(k-1) + \rho_k \Delta z_k S_N(k)}{\rho_k V_N^*(k) F_{\rm cld}(k)} \tag{3.8b}$$

Note that the provisional fall speeds V_q^* and V_N^* are used to determine $q_r'(k)$ and $N_r'(k)$.

7. Use (3.4) to calculate the final fall speeds at level k.

In order to ensure that moisture budget is closed, the surface precipitation P_{surf} is calculated using S_q rather than q_r as

$$P_{\text{surf}} = \sum_{k=1}^{n} S_q(k)\rho_k \Delta z_k, \tag{3.9}$$

where n is the number of vertical levels, and I've ignored the contribution from snow. The contribution from snow throughout follows analogously and has been suppressed for clarity.

Origin of the surface precipitation bias

There are two components that allow nonzero P_{surf} despite $q_r = 0$ at the surface. The first is a simple bug due to a threshold requirement. If $q_r^*(k) = 0$ in step 3 of the procedure, and there is no new auto-conversion occurring within the cell, then steps 5 and 6 are bypassed and reduce to $S_q(k) = 0$ and $q_r'(k) = 0$. Consider the case where k_0 refers to a grid cell below the lowest cloud base in which the predictor step predicts that all of $q_r'(k_0 - 1)$ evaporates, leaving $q_r^*(k_0) = 0$. The net result should be zero surface precipitation. However, since $S_q(k_0) = 0$ is incorrectly calculated to be zero despite $\sum_{k<k_0} S_q(k)\rho_k \Delta z_k > 0$, there is a net positive surface precipitation recorded. Furthemore, since $q_r(k) = 0$ for $k \geq k_0$, there is no way for the scheme to remove this spurious precipitation source through further evaporation since the model doesn't "see" any rain present.

My solution for this problem is simply to force $S_q(k)$ and $S_N(k)$ to be calculated when $q_r^*(k) = 0$ and $q_r^*(k-1) \neq 0$, by artificially choosing $q_r^*(k) \approx q_r'(k-1)$. The rationale for this is to allow the scheme to proceed as it otherwise would be expected to, under the assumption that, if the prediction step evaporates enough moisture to deplete the rain, then so will the correction step.

The second source of a precipitation bias is understood by rewriting (3.9) in terms of q_r

with the help of (3.8):

$$\begin{aligned} P_{\text{surf}} &= \sum_{k=1}^{n} \rho_k q_r(k) V_r^*(k) - \rho_{k-1} q_r(k-1) V_r(k-1) \\ &= \rho_n q_r(n) V_r^*(n) + \sum_{k=1}^{n-1} \rho_k q_r(k) \left(V_r^*(k) - V_r(k) \right). \end{aligned} \tag{3.10}$$

In the case $V_r^*(k) = V_r(k)$, then the sum in (3.10) is equal to zero and the desired surface precipitation term is recovered: $P_{\text{surf}} = \rho q_r V_r$ evaluated at the surface. However, if $V_r^*(k) \neq V_r(k)$, which is possible in the current implementation, then there can be a net bias in the surface precipitation. In practice, it is unclear how often this occurs. In the DYCOMSII–RF01 case, the amount of spurious surface precipitation was on the order of less than 0.1 millimeter per day, and even then only when the LWP was large enough to produce precipitation within the cloud (primarily the L80 simulations). At any rate, it is undesirable for $V_r^*(k) \neq V_r(k)$, since that means the precipitation profile is not in agreement with the assumed droplet size distribution given by (3.3).

My solution for this problem is to eliminate the need for the provisional V_r^* and V_N^* fall speeds and instead partition the rain number and mixing ratio fluxes into q_r and V_r (or N_r and V_N) in a way that is consistent with (3.3) from the outset. This is accomplished by first dividing the equations in (3.7). With help from (3.4) and (3.6), this ratio allows me to solve for λ:

$$\lambda = \left[\pi \rho_w \frac{c_q}{c_N} \left(\frac{\rho_{k-1} N_r'(k-1) V_N(k-1) F_{\text{cld}}(k-1) + \rho_k \Delta z_k S_N(k)}{\rho_{k-1} q_r'(k-1) V_q(k-1) F_{\text{cld}}(k-1) + \rho_k \Delta z_k S_q(k)} \right) \right]^{1/3}. \tag{3.11}$$

Once λ is known, the rest follows. V_r and V_N are calculated from (3.6), and then (3.7) are solved for $q_r'(k)$ and $N_r'(k)$.

In order to make as few changes as possible to existing parametrizations so that the single column tests remain as close as possible to CAM5 parameterizations, I implement the above approach only during the "corrector" step. This is not intended to act as a full fix, but rather the simplest approach to correct the discrepancy for warm, low clouds. Further refinement of this approach would be required if it was to be implemented in the full model.

Figure 3.12 shows that the fixes described above eliminate much of the surface precipitation in the L80, dt300 model runs for the $N_d = 25$ cm^{-3} case, and produces a more reasonable precipitation flux. Removing this unphysical sink of cloud water and boundary layer moisture is capable of increasing the LWP by a few grams per meter-squared. Although modest, it is not altogether negligible, and when integrated in the global model may have a non-trivial impact, since it is a feature that can only produce a negative moisture bias (i.e., too much surface precipitation). In terms of the aerosol indirect effect, the signal would most likely be seen as increasing the LWP of clouds in conditions of low aerosol concentrations while making little difference to those formed under high aerosol concentrations.

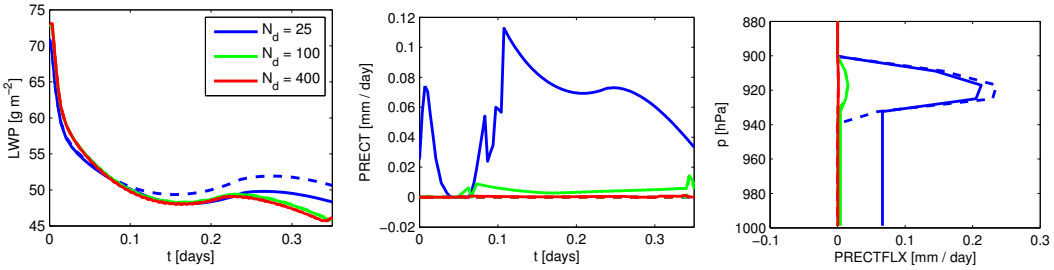

Figure 3.12: LWP (left), surface precipitation (center), and 4–8 hour mean precipitation flux (right) for L80 EntrSed simulations. Dashed lines indicate the version with my precipitation fixes applied.

Since spurious surface precipitation is not a factor in the default L30 simulations, it is clear that this effect is not *responsible* for the sign of the AIE in SCAM5, but it it certainly has the potential to contribute. For example, turning on the entrainment-sedimentation feedback factor by setting $a_{\text{sed}} = 9$ alone is not enough to reverse the sign of the AIE in the default L80 simulations, but when combined with removing the unphysical surface precipitation *is* enough to reverse the sign.

3.4.5 Dynamical Controls on LWP: Vertical advection scheme

One of the most surprising controls on LWP is the numerical scheme used for vertical advection. This is an example where the numerical choice made for a dynamical process has a strong impact on the resulting cloud fields. Consider Figure 3.13. The primary

difference between the default operation of SCAM 5.1 and SCAM 5.0 used in this analysis is that SCAM 5.1 uses a centered difference scheme by default for vertical advection. The result is a widely divergent LWP between the $N_d = 25$ cm^{-3} and $N_d = 100$ cm^{-3} cases in SCAM 5.1 (left panel) compared with SCAM 5.0. Changing to an upwind scheme (right panel), however, eliminates the bulk of the difference (compare with the LWP evolution for SCAM5.0 shown in Figure 3.3).

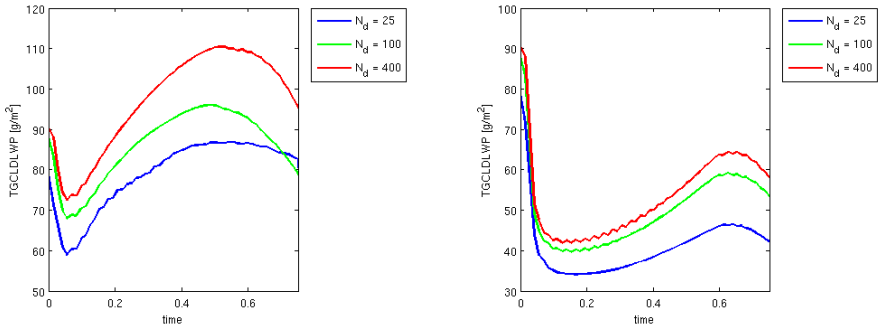

Figure 3.13: Time series of LWP for DYCOMSII–RF01 in the default configuration in SCAM5.1 using a center-difference (left) and upwind (right) scheme for vertical advection.

Conceptually, this could be expected from the presence of the capping inversion above the boundary layer. As a thought experiment, consider a moisture profile that is constant and dry above the inversion (q^+) and well-mixed and moist below (q_M), in a region of subsidence (i.e., $w < 0$). The advective tendency is given by $\frac{\partial q}{\partial t} = -w\frac{\partial q}{\partial z}$. Consider the grid point directly above the inversion. Using an upwind scheme, this tendency is clearly zero, since $q = q^+$ for $z > z_i$ means that $\Delta q/\Delta z = 0$ for any consistent upwind scheme. On the other hand, a centered difference scheme will include a contribution from below the inversion, so that $\Delta q/\Delta z < 0$, leading to a *negative* $\frac{\partial q}{\partial t}$ due to advection – i.e., additional drying above the boundary layer, and a larger inversion jump of moisture. A similar result holds for temperature, where the grid layer immediately above the inversion will produce enhanced warming using a simple center difference scheme.

If two simulations are otherwise identical except for the advection scheme, then, one would expect larger inversion jumps from the centered difference scheme. All else being

equal, this will suppress entrainment, resulting in a higher LWP under the center difference scheme than the upwind. This is supported by Figure 3.13, where the only difference between the two SCAM5.1 simulations is that one set uses the centered difference scheme for vertical advection (left) while the other uses upwind advection (right).

Somewhat ironically, neither choice is what is used in the global model, which uses a Lin-Rood finite volume scheme for advection that does the vertical advection implicitly using a remapping algorithm designed to maintain mass conservation (Neale et al., 2010; Lin and Rood, 1996). In SCAM, using the upwind scheme is preferable, since it reduces unphysical warming and drying above the boundary layer.

3.4.6 Additional sensitivity studies

In the course of this study, several other sensitivities were considered. Table 3.2 summarizes the mean LWP for fixed droplet concentrations in DYCOMSII–RF01, subject to the changes in model configuration described in this chapter. Entries colored blue indicate a greater LWP than for $N_d = 400$ cm^{-3}, and those that are red indicate a smaller LWP than for $N_d = 400$ cm^{-3}. In each row, the $N_d = 25$ cm^{-3} and $N_d = 100$ cm^{-3} columns present the difference in LWP from the $N_d = 400$ cm^{-3} simulation, somewhat arbitrarily using the 6-12 hour mean.

Setting $a_{\text{sed}} = 9$ in (3.1), based on Bretherton et al. (2007), explicitly enhances the contribution of sedimentation to the entrainment efficiency. One justification for this is to correct for the under-prediction of q_ℓ^{eff} at the cloud top due to under-resolution. In both L30 and L80 simulations, designated EntrSed in Table 3.2, this factor behaves as designed, decreasing entrainment preferentially more for lower N_d and increasing LWP accordingly. However, this factor alone is not strong enough to reverse the sign of the AIE in DYCOMSII–RF01.

The role of using pdf-based macrophysics was also considered. The motivation for this test was the discrepancy between CLDLIQ and CLOUD in Figure 3.7, in which the column with the highest total cloud fraction corresponded to the lowest LWP and vice versa. Although configurations were found in which the use of pdf-based macrophysics (denoted as

Table 3.2: Summary of mean LWP response to droplet concentration in a variety of SCAM simulations. The mean LWP for hours 4-8 of the simulations for $N_d = 400$ cm^{-3} are shown. The mean LWP response for $N_d = 25$ cm^{-3} and $N_d = 100$ cm^{-3} are shown as differences from $N_d = 400$ cm^{-3}. Cells have been color-coded, so that red cells denote simulations where the response has the opposite expected sign, while blue cells denote simulations with the correct sign of the AIE. For comparison, LES results are included as well. Simulations that were not performed are marked by a dash. Brief descriptions of the case abbreviations in the left column are provided in footnotes.

	L30, dt = 1200s			L80, dt = 300s		
	25 cm^{-3} Δ	100 cm^{-3} Δ	400 cm^{-3} LWP [g m^{-2}]	25 cm^{-3} Δ	100 cm^{-3} Δ	400 cm^{-3} LWP [g m^{-2}]
Default[a]	-6	-2	34	-5	-2	50
Default, dt100[b]	+4	-3	74	-7	-10	56
EntrSed[c]	-4	-1	35	≈ 0	≈ 0	52
PrecMod[d]	-	-	-	-2	-1	46
EntrSed, PrecMod	-4	-1	35	+3	≈ 0	52
pdf mac[e]	-9	-2	45	-4	-1	56
pdf mac, dt100	+7	+1	71	-5	≈ 0	57
PseudoCon[f]	-4	-1	52	+4	+1	64
PseudoCon, dt100	+3	≈ 0	74	-	-	-
PseudoCon, EntrSed	≈ 0	≈ 0	53	-	-	-
PseudoCon, EntrSed, dt100	7	2	76	-	-	-
SAM (LES)	+9	+2	50			

[a] Default configuration, described in text.
[b] Time step $\Delta t = 100$ s.
[c] Explicit entrainment-sedimentation feedback ($a_{\text{sed}} = 9$).
[d] Modified precipitation following Sec. 3.4.4.
[e] Using pdf-based macrophysics.
[f] Assuming pseudo-conservative diffusion (i.e., no diffusion of q_ℓ).

pdf_macro in Table 3.2) recovered the correct sign of the AIE, this was only achieved with short time steps. Though it corrected the CLOUD – CLDLIQ problem, it did not robustly improve the LWP response to N_d.

3.5 Global CAM5 Runs

To assess the degree to which these changes impact the AIE in the global CAM5 GCM, a set of 10-year pre-industrial (PI) and present day (PD) simulations were run in each of the following configurations:

1. CTL: Default CAM5 simulation for comparison.

2. D1a: Using CLDLIQ for UW_ql in the PBL scheme.

3. D1b: As in D1a, but with no diffusion of q_ℓ in the PBL scheme (i.e., "pseudo-conservative" diffusion).

4. D1c: As in D1a, but with $a_{\text{sed}} = 9$ in (3.1).

5. D2: As in CTL, but with my precipitation modifications.

Table 3.3 summarizes the global mean statistics for the PD simulations. The CTL simulation results are broadly consistent with the CAM5 results presented in Wang et al. (2011). As expected, each of the D1 simulations increases the low cloud amount and thus results in a larger negative SWCF than the CTL. The low cloud increase is primarily in the Sc-Cu transition region. There is an unexpectedly large decrease in the LWCF associated with changes in the high cloud cover and optical depth. This is surprising, since the only changes made were to the PBL turbulent mixing scheme. Presumably this indicates that the optical depth of high clouds is affected by turbulent mixing, either directly during deep convection where the PBL scheme is active, or indirectly through the amount of moisture transported aloft from the surface.

Despite the significant mean state sensitivity of SWCF and CLDLOW exhibited by the D1 simulations relative to CTL, the AIE deduced from the difference between PD and PI

simulations (Table 3.4) is rather modest. The D1a and D1b SWCF changes are 0.12 W m^{-2} and 0.03 W m^{-2} more positive than the CTL, respectively. The D1c simulation actually exhibits an *enhanced* SWCF response (-0.15 W m^{-2}). This last result is puzzling, particularly because explicitly representing the entrainment-sedimentation feedback by modifying the evaporative enhancement parametrization should enhance the entrainment response under higher aerosol loading.

One possible reason that the impact of the D1a and D1b changes on the AIE is muted is that the regions responsible for the largest AIE signal are regions where the aerosol loading is highest, particularly southeast Asia. The CCN over SE Asia can increase by a factor of 4 or more (e.g., see Wang et al., 2011, Fig. 9). The changes made in the D1 simulations target the AIE induced by nearly non-precipitating stratocumulus, which are most prevalent over the oceans where CAM5-simulated CCN concentrations increase more modestly (10-50% over much of the tropical ocean, and 70-150% directly offshore to the west of the Americas). Thus, the potential impact of these changes is limited because they don't target the regions that exhibit the strongest aerosol changes in CAM5, which occur in regions that exhibit deep convection as well.

Table 3.3: Global means for selected quantities from each of the CAM5 simulations discussed in Sec. 3.5. For each of the tests, the difference from the CTL (first column) is shown. CAM5 output field names appearing in this table are listed in Table 3.1.

	CTL	$\Delta D1a$	$\Delta D1b$	$\Delta D1c$	$\Delta D2$
CLDLOW [%]	45.3	1.9	1.6	2.2	-0.1
SWCF [W m^{-2}]	-54.9	-1.7	-0.9	-2.3	-0.04
LWCF [W m^{-2}]	25.4	-1.2	-1.6	-1.1	-0.1

The D2 simulations show that the precipitation fixes make very little impact on the global model behavior. This is not surprising, since the changes affect only a very small amount of surface precipitation, and only under conditions where there should be no surface precipitation at all. Even in the SCAM5 DYCOMSII–RF01 simulations, this made a rather small impact on LWP of a few g m^{-2} at most. It is encouraging, however, that my changes

Table 3.4: Global mean differences between PD and PI simulations. Here the net difference in cloud forcing can roughly be thought of as an estimate for the CAM5 simulated AIE.

	CTL	D1a	D1b	D1c	D2
Δ CLDLOW [%]	0.09	-0.01	0.14	0.16	0.08
Δ SWCF [W m^{-2}]	-1.76	-1.64	-1.73	-1.91	-1.75
Δ LWCF [W m^{-2}]	0.60	0.54	0.42	0.57	0.62
Δ Net CF [W m^{-2}]	-1.16	-1.10	-1.31	-1.34	-1.13

did not induce large, unintended changes across the globe. There is a troubling increase in the average rain number concentration by up to an order of magnitude (not shown). Whether this is due to a failing in my implementation or is simply a consequence of (3.3) would require further analysis, which at the current time is unwarranted. However, if these precipitation modifications were to be pursued further in the future, a more careful implementation of the changes, as well as more detailed analysis of the consequences, would be necessary.

3.6 Conclusions

Aerosol indirect effects are born through interactions of quantities determined by several independent parameterizations in CAM5. For weakly drizzling stratocumulus, a potentially important mechanism is the entrainment efficiency (calculated by the PBL scheme). This, in turn, depends partially on the cloud droplet sedimentation, which itself is determined by the cloud macrophysics and microphysics parametrizations. For the overall model to effectively represent sensitivities that rely on such cross-parametrization effects requires a degree of consistency across parametrizations that is difficult to achieve in practice. Further, one must appreciate that changes in the implementation of one parametrization may have unintended consequences further down the stream.

There are several contributing factors that impact the response of non-drizzling Sc LWP to cloud droplet concentration in SCAM5, supported by simulations summarized in Table 3.2. The representation of q_ℓ internally within the PBL scheme used for calculation of

entrainment rate makes a substantial impact on how sensitive the entrainment efficiency is to droplet concentration. Simply assuming pseudo-conservative diffusion is an entirely justifiable parametrization choice, and alleviates the difficulty of representing the diffused condensate final state within the PBL scheme (used to calculate the diffusivities) in a manner that is computationally cheap and consistent with the behavior of the rest of the physics parametrization suite. Since aerosol-cloud interactions span a range of physical processes by their nature (Stevens and Feingold, 2009), capturing this response requires consistency across the parametrizations when possible.

Increased resolution, particularly temporal resolution, mitigates excessive depletion of LWP through drizzle. Improved vertical resolution within the boundary layer, particularly near cloud top, better captures q_ℓ^{eff}, which impacts the entrainment efficiency and turbulent mixing within the boundary layer.

Explicitly including the entrainment-sedimentation feedback into the entrainment efficiency further increases the negative LWP relationship with increasing droplet concentration. Including this factor, particularly in the L30 simulations, is a reasonable way to correct for under-estimating q_ℓ^{eff} at cloud top due to under-resolution. One could make this more scale-aware by tying the strength of the evaporative enhancement correction coefficient to the vertical grid spacing.

3.6.1 Recommendations for CAM5

This study suggests several recommendations to improve the representation of boundary layer clouds in CAM, and which also make modest contributions to better representing the AIE.

The most important recommendation is to assume the pseudo-conservative diffusion in the PBL scheme. This allows the cloud fields from the rest of CAM5's physics parametrization suite to be utilized by the PBL scheme, preserving as much consistency as possible with the rest of the model. Furthermore, this change is easy to implement and has the most robust impact on the SCAM5 AIE for non-drizzling Sc.

A second simple change that is easily justified is to include the explicit entrainment-

sedimentation feedback term to the evaporative enhancement of the entraiment efficiency by choosing positive a_{sed} in (3.1). Some care and tuning of this parameter may be required, and if this is to be implemented further analysis of the global model simulations should be performed, particularly in light of the D1c simulations that showed this change unexpectedly increased the magnitude of ΔSWCF between the PI and PD.

The vertical advection scheme makes a dramatic impact on the modelled mean LWP in single-column mode, which in turn modulates the strength of LWP-related feedback mechanisms. In SCAM5, using an upwind vertical advection scheme is recommended to avoid the unphysical warming and drying directly above the capping inversion that is induced by a centered difference scheme.

Running the global model with a shorter time step is almost certain to provide improvements, provided the use of a shorter time step does not violate assumptions made within the parameterizations[5]. These single column studies indicate this, combined with the q_ℓ diffusion recommendation, would likely weaken the AIE due to nondrizzling Sc. To the extent that running the model with shorter time step is feasible given computing resources, there is little reason *not* to do it. Indeed, if CAM5 (once properly retuned) operating with a shorter time step *doesn't* improve model performance, then such a lack of convergence indicates serious deficiencies in the current modelling framework.

Finally, although the D2 simulation suggests the global impact is minimal, implementing my modifications to the framework for diagnosing precipitation droplet size and number distributions in the microphysics scheme is desirable, as it removes a small positive surface precipitation bias and also ensures that precipitation mixing ratio and number concentration adhere to the underlying assumed precipitation distribution, all while adding no meaningful computational cost. Such implementation is unlikely to be pursued further, however, considering that the microphysics scheme is due to be overhauled in favor of a prognostic precipitation scheme in the future version of CAM currently under development.

[5]For example, diagnostic precipitation implicitly assumes that time steps are long relative to the characteristic time scale for precipitation formation.

Chapter 4

MECHANISMS OF MARINE LOW CLOUD SENSITIVITY TO IDEALIZED CLIMATE PERTURBATIONS: AN MLM AND LES EXPLORATION OF THE CGILS S12 CASE

Climate change sensitivities of subtropical cloud-topped marine boundary layers are analyzed using a mixed-layer model (MLM) of the CGILS S12 well-mixed stratocumulus case and compared against LES. A steadily forced control simulation is run to steady-state, as are simulations with forcings perturbed by changes in temperature, free-tropospheric relative humidity, CO_2 concentration, subsidence, inversion stability, and wind speed. Cloud responses to combined forcings superpose approximately linearly.

For the $2\times CO_2$ forcing perturbations estimated from the CMIP3 multimodel mean, the MLM predicts a positive shortwave cloud feedback, like most CMIP3 global climate models. The cloud remains overcast but thins in the warmer, moister, CO_2-enhanced climate, due to the combined effects of an increased lower-tropospheric vertical humidity gradient and an enhanced free tropospheric greenhouse effect that reduces the radiative driving of turbulence. Reduced subsidence due to weakening of tropical overturning circulations partly counteracts these two factors by raising the inversion and allowing the cloud layer to deepen. These compensating mechanisms may explain the large scatter in low cloud feedbacks predicted by climate models. CMIP3-predicted changes in wind speed, inversion stability, and free-tropospheric relative humidity have lesser impacts on the cloud thickness. MLM and LES agree remarkably well in cases where the LES does not decouple.

4.1 Introduction

This chapter details the application of an LES and MLM to evaluating the sensitivity of a stratocumulus-topped boundary layer to climate-change perturbations. Much of this material is featured in Bretherton et al. (2013), which details the large-eddy simulation (LES) sensitivity analysis of the Cloud Feedback Model Intercomparison Project (CFMIP)

- Global Atmosphere System Study Intercomparison of Large-Eddy Simulation and Single Column Models (CGILS) cases. Bretherton et al. (2013) is, in turn, a companion to Blossey et al. (2013), which describes the broader LES intercomparison component of CGILS, and to Zhang et al. (2013), which provides an overview of CGILS.

The goal of CGILS was to develop prototype cases for comparing the response of subtropical cloud topped boundary layers to idealized climate perturbations in both single-column models and LES. Cases were set up for three different cloud regimes—well-mixed stratocumulus, cumulus rising into stratocumulus, and shallow cumulus—corresponding to typical summer conditions at three different locations called S12, S11 and S6 along a transect across the northeast Pacific Ocean extending from near San Francisco past Hawaii.

For each location, a pair of steadily forced simulations was performed with each model. Each pair consisted of a control (CTL) simulation corresponding to July 2003 monthly-mean boundary conditions and advective forcings, and a P2S simulation with perturbed forcings and boundary conditions. The perturbations represented an idealized large scale climate change nominally corresponding to a uniform 2 K warming of the sea-surface temperature (SST) locally and over the entire tropics. They also included a moist-adiabatic increase of the free tropospheric temperature profile that might accompany such an SST increase, a moistening of the free troposphere to maintain constant relative humidity, and an 11% reduction in the tropospheric profile of mean subsidence (weakening of the downward branch of the Walker circulation). The temperature increase had a vertical structure that did not significantly change the Estimated Inversion Strength (EIS) of Wood and Bretherton (2006). In the S12 case, the intercomparison also included a P2 case like P2S but with no mean subsidence reduction. Each LES simulation was run out at least 10 days to achieve a near steady-state. The P2S - CTL difference was interpreted as a cloud response to that climate change.

Blossey et al. (2013) found that, to a considerable extent, the participating LESs produce similar responses to the idealized climate change in all of the different cloud regimes. This motivated Bretherton et al. (2013), which analyzed the simulated cloud and boundary layer sensitivity to a broader set of climate-related perturbations with a single LES and interpreted these in terms of physical mechanisms of cloud response in order to develop a better

and perhaps more observationally testable understanding of subtropical cloud feedbacks.

The current chapter applies the MLM described in Chapter 2 to the CGILS S12 case to further analyze and interpret the LES subtropical stratocumulus sensitivities presented in Bretherton et al. (2013). As in the published study, I consider the response of the stratocumulus cloud regime cloud regimes to changes in CO_2 concentration, humidity, subsidence, inversion stability, and wind speed in addition to the P2S change that was the focus of CGILS. Simulations to test the linearity of the cloud response to combinations these different climate perturbations are also performed.

The setup and some of the sensitivity studies are analogous to a study of Caldwell and Bretherton (2009), who analyzed the sensitivity of the steady-state behavior of a Sc-capped mixed layer model to changes in CO_2, local SST and an "ITCZ" SST that generates a moist adiabat that controls the free-tropospheric temperature profile. They found that increasing local and ITCZ SSTs comparably (as in a greenhouse-induced global warming) tends to weaken subsidence, raise the inversion and thicken the cloud layer, while increasing CO_2 without changing either SST tends to lower the inversion and slightly thin the cloud layer. With a simplified version of their mixed-layer model, they were able to physically explain both of these responses. On balance, their analysis suggested a thickening of the stratocumulus in a warmer climate, which induces a negative contribution to cloud feedback on greenhouse warming in regions of subtropical coastal stratocumulus. The current MLM and LES results provide an interesting comparison to their findings.

Sec. 4.2 discusses the detailed configuration of the sensitivity cases. Sec. 4.3 documents salient features of the MLM and LES. Sec. 4.4 provides results and interpretation for the S12 case. Further discussion and conclusions are presented in Sec. 4.6.

4.2 Setup of simulations

The climate perturbations considered are given in Table 4.1. Perturbations that do not involve changes in the SST or free-tropospheric temperature profiles are named in terms of the key parameter that is changed, except for the dCMIP3 case described below. All other perturbations include a "P2," indicating that the free troposphere has been moist-adiabatically warmed assuming a 2 K warm-pool SST increase. These perturbations also

include a 2 K local SST increase unless otherwise indicated. Other name modifiers indicate additional changes ("S" for reduced subsidence, "FT" for only warming the free-troposphere, not the local SST). The setup of the control simulation and cases P2S and P2 are described in Blossey et al. (2013). In case dRH the relative humidity of the reference state is decreased uniformly in the free troposphere. In case dWS the wind speed is uniformly decreased, changing the surface fluxes, but leaving the prescribed horizontal advection of heat and moisture unchanged. In all cases the free-tropospheric horizontal advective tendencies are chosen to balance the steady-state heat and moisture budgets for the reference profiles. Following Blossey et al. (2013) the boundary-layer advective tendencies are equal to the control or P2S case, depending on the SST, and a ramp function between 800 and 900 hPa is used to interpolate between the boundary layer and free tropospheric advective tendencies.

In Phase 3 of the World Climate Research Program Coupled Model Intercomparison Project (CMIP3) (Meehl et al., 2007), a large ensemble of global climate models (GCMs) archived output from a standardized set of climate change simulations in support of the Fourth Assessment of the Intergovernmental Panel on Climate Change. From various studies that analyzed the CMIP3 model output, Bretherton et al. (2013) estimated CMIP3 multimodel mean changes and intermodel scatter in each of the above perturbations. Table 4.2 reproduces Table 1 of Bretherton et al. (2013), which provides these representative perturbations and intermodel ranges for CMIP3 slab-ocean simulations run to climate equilibrium with doubled CO_2, or in some cases for the A1B scenario between 2000 and 2100, during which time CO_2 approximately doubles. The dCMIP3 case simultaneously changes each of the parameters in Table 4.2 to reflect their CMIP3 multimodel mean responses to CO_2 doubling.

4.3 Description of models used

The MLM and SAMA LES are configured following the CGILS LES specifications described by Blossey et al. (2013), which include a bulk surface flux formulation, a cloud droplet concentration $N_d = 100$ cm^{-3}, and diurnally-averaged cloud-interactive longwave and shortwave radiation. The solar constant is rescaled consistently with the choice of solar zenith angle so that downwelling shortwave flux equals the diurnal average of the down-

Table 4.1: Description of sensitivity studies

Name	Description
CTL	Control
CTLD	CTL with diurnal cycle of insolation
4CO2	CO_2 concentration quadrupled from CTL
dRH	5% free-tropospheric relative humidity decrease
dWS	5% wind speed decrease
P2	2 K local SST increase; free-troposphere moist-adiabatically warmed by 2 K remote boundary-layer warming
P2D	P2 with diurnal cycle of insolation
P2S	P2 with 10% subsidence decrease
P2SFT	P2S but no warming of SST
dCMIP3	CTL with doubled CO_2 and other parameters perturbed as in Table 4.2

welling insolation at the CGILS location and time of year. As per the CGILS specifications, the cosine of the solar zenith angle is uniformly averaged across all times between sunrise and sunset. In hindsight, a more accurate approach would be to use an insolation-weighted average of the cosine of the zenith angle, which reduces the imposed zenith angle from approximately 50° to 40°. This approach would somewhat reduce the cloud albedo (see Chapter 2 of Hartmann (1994) and Sec. 4.4.1).

In both models, radiation is calculated using the Rapid Radiative Transfer Model - GCM version (RRTMG) scheme (Mlawer et al., 1997) by extending the model grid up into the stratosphere to allow specification of thermodynamic profiles throughout the entire atmospheric column. Horizontal winds are nudged to a specified profile in the LES with a 10 minute timescale.

The free-tropospheric column in both models experiences interactive radiative heating, CGILS-specified subsidence and horizontal advection profiles and thermodynamic relaxation to specified CGILS profiles above a relaxation height of 1200 m.

Table 4.2: CMIP3 forcing changes associated with CO_2 doubling.[a]

Perturbation	Description	Reference
δSST(15-35N)	2.5±0.5 K	IPCC (2007) Fig. 10.6 and Box 10.2
$\delta\omega$(500 hPa)	-5±3%	Vecchi and Soden (2007) Fig. 1; Webb et al. (2013) Fig. 7f/9f
δEIS	0.6±0.2 K	Webb et al. (2013) Fig. 7e/9e
δRH	-1.5±1%	Richter and Xie (2008) Fig. 10; Sherwood et al. (2010) Fig. 2
δWS	-1.5±1.5%	Lu and Cai (2009) Table 3 (Tropical)

Estimated changes in selected forcing and boundary conditions associated with CO_2 doubling at climate equilibrium, based on CMIP3 model studies, for the subtropical stratocumulus and transition regions. These are defined as the 80-100 percentile regimes of 30°N-30°S oceanic monthly-mean lower tropospheric stability (the approximate range spanned by the CGILS study locations). Where necessary, published values have been rescaled from published units assuming a 3 K equilibrium climate sensitivity. The change of mid-tropospheric vertical pressure velocity $\delta\omega$ has been further scaled into a relative change by dividing by the mean ω(500 hPa)$\approx$ 30 hPa d^{-1} for this lower tropospheric stability range.

[a] Reproduced from Table 1 of Bretherton et al. (2013).

4.3.1 SAMA LES

The LES used in this study is version 6.7 of the System for Atmospheric Modeling (SAM), kindly supplied by Marat Khairoutdinov and documented by Khairoutdinov and Randall (2003) and Blossey et al. (2013). The advection scheme of Blossey and Durran (2008) is used for the four advected scalars, liquid static energy $s_\ell = c_p T + gz - L(q_\ell + q_r)$, total nonprecipitating water mixing ratio $q_t = q_v + q_\ell$, rain water mixing ratio q_r, and rain number concentration N_r. Here c_p is the specific heat of dry air at constant pressure, T is temperature, g is the acceleration due to gravity, z is height, L is the latent heat of vaporization, q_ℓ is cloud liquid water mixing ratio, and q_v is the vapor mixing ratio. As noted by Blossey et al. (2013), this model version, referred to as SAMA, produces less numerical diffusion at the sharp, poorly resolved inversion that caps the stratocumulus cloud layers being simulated, resulting in higher and more realistic simulated stratocumulus liquid water paths. The cloud liquid water and temperature are diagnosed from the advected scalars

using the assumption of exact grid-scale saturation in cloudy grid cells. The Khairoutdinov and Kogan (2000) scheme is used for conversion between cloud and rain water. Cloud droplet sedimentation is included following Eq. (7) of Ackerman et al. (2009), based on a log-normal droplet size distribution with a cloud droplet number concentration $N_d = 100\text{cm}^{-3}$ and a geometric standard deviation $\sigma_g = 1.2$.

Following Blossey et al. (2013), the domain is doubly-periodic in the horizontal, and the vertical grid spacing is 5 m near the trade inversion while the horizontal resolution is 25 m. All of the LES runs in this study were carried out by Dr. Peter Blossey.

4.3.2 Mixed-layer model

The MLM is described in great detail in Chapter 2.1, but a brief summary is provided here. The formulation of the MLM equations follows Uchida et al. (2010) and Caldwell and Bretherton (2009). The MLM includes representations of precipitation and cloud droplet sedimentation. It uses the Nicholls and Turton (1986) entrainment parameterization modified to include LES-tuned parameterization of sedimentation effects on entrainment efficiency (Bretherton et al., 2007). As in Uchida et al. (2010), the evaporative enhancement coefficient a_2 and the cloud base drizzle rate power law have been adjusted to match the SAMA LES. This allows the MLM to simulate a mean cloud thickness and boundary layer properties that are comparable to the LES, permitting more meaningful comparison of sensitivities of the MLM and LES to climate-relevant perturbations.

As in Caldwell and Bretherton (2009), the MLM is coupled to a time-dependent model of the free troposphere column evolving due to radiative heating and CGILS free-tropospheric advective forcings. The model uses 40 grid layers between the inversion and 1600 m and a fixed nonuniform grid above 1600 m to resolve the radiative heating profile. The radiative fluxes and thermodynamic values in the lowest free-tropospheric level (typically 20 m or so above the inversion) are used as the upper boundary condition for the MLM. The MLM uses the CGILS-specified near-surface wind with a bulk surface transfer coefficient of 10^{-3} applied to differences between mixed layer and sea-surface values of s_ℓ and q_t for calculation of surface fluxes; this produces fluxes similar to the more sophisticated CGILS-specified

LES approach (Blossey et al., 2013) that is based on assuming a surface log-layer profile of wind and conserved scalars.

4.4 Simulation results

4.4.1 The S12 control simulation and diurnal cycle sensitivity

Fig. 4.1 shows the time-height evolution of the S12 control (CTL) and diurnal cycle (CTLD) simulations for both the LES and MLM. The top panels show the hourly-mean cloud fraction for the LES, while the bottom panel shows the cloud top (z_i) and cloud base (z_b) from the MLM evolution. The LES control simulation has a stratocumulus layer of almost 100% cloud fraction and approaches a quasi-steady state in 10 days. The MLM, of course, assumes 100% cloud cover implicitly, but also approaches a quasi-steady state in the same time frame.

The diurnal cycle simulations have nearly identical mean cloud-top height and liquid water path (LWP) averaged over days 8-10 in both the MLM (46.8 g m^{-2} for CTL versus 45.3 g m^{-2} for CTLD) and SAMA LES (49.1 g m^{-2} for CTL versus 47.2 g m^{-2} for CTLD). The MLM was initialized at a different starting time of day. Figure 4.2 plots the LWP for the CTL and CTLD simulations in LES and MLM shifted in time so that $t = 0$ corresponds to the maximum insolation. From this we see that the time shift between the driving insolation and the LWP is remarkably similar between the LES and MLM CTLD simulations. However, the LWP in the MLM is less responsive to the diurnal cycle than the LES is, with a smaller peak-to-peak amplitude in the MLM. The LWP in the MLM also reaches its smaller night time maximum and begins to decline somewhat sooner than the LES.

In both LES and MLM, the daily-mean shortwave cloud radiative effect (SWCRE[1]) in CTLD is somewhat weaker[2] (26–29 W m^{-2}) than that in CTL. Offline radiation calculations imply that 20 W m^{-2} of this difference is an avoidable bias due to the CGILS specification to use the daytime mean rather than insolation-weighted cosine of the solar zenith angle. The remaining 10 W m^{-2} is due to the diurnally-varying clouds being thinner during the day

[1]SWCRE is defined as the top of atmosphere net incoming shortwave radiation difference between all-sky (with clouds) and clear-sky (no clouds) conditions.

[2]Throughout this chapter, "weaker (or stronger)" SWCRE means "less (or more) negative."

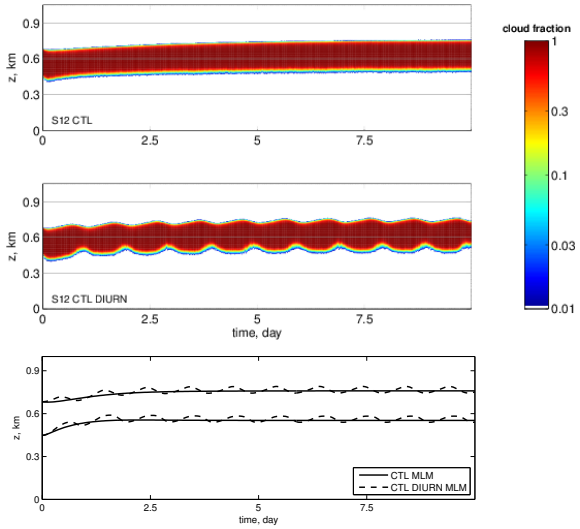

Figure 4.1: Time-height profiles of horizontal-mean cloud fraction for the S12 control (CTL, top) and diurnal cycle (CTLD, middle) LES simulations, and cloud top and cloud base for corresponding MLM simulations (bottom).

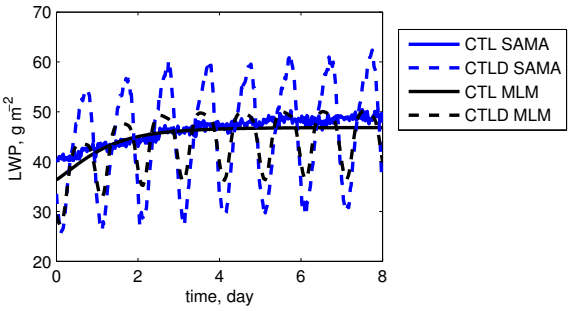

Figure 4.2: LWP for CTL and CTLD simulations for both SAMA LES and MLM. Time coordinate has been shifted such that $t = 0$ corresponds to peak insolation in both MLM and SAMA to account for differing initial time of day between LES and MLM simulations.

than the night. We conclude that diurnally-averaged insolation is a plausible simplification.

Compared to the observed summertime climatology at location S12 (Lin et al., 2009), CTL has a slightly higher cloud top, smaller LWP, larger cloud fraction, and stronger SWCRE. Quantitative agreement with climatology is not expected, because the simulations do not include transient forcing variability, and also because of the possible model biases in specified forcings, entrainment, microphysics, and radiation. Qualitative agreement with observations is taken to be an adequate basis for regarding these sensitivity experiments as meaningful indicators of cloud response in the coastal well-mixed stratocumulus regime. The MLM could, in principle, could be tuned through the entrainment and drizzle parametrizations to match the observed mean state more closely[3] (with the exception of cloud fraction), but the present goal is to compare the MLM with the LES. It should also be noted, following Caldwell et al. (2012), that cloud feedbacks may also reflect changes in the distribution of different cloud types, e. g. in the relative frequency of well-mixed stratocumulus, for which this study does not fully account.

4.4.2 Summary of S12 sensitivity study results in LES

Table 4.3, reproduced from Table 3 of Bretherton et al. (2013), gives salient statistics from the LES runs. Fig. 4.3 shows thermodynamic and vertical velocity variance profiles for the day 8-10 averages from the LES, which we take as adequate approximations to steady states of the S12 runs. The near-coincidence of cloud base z_b and near-surface lifted condensation level (LCL), and the uniformity of s_ℓ/c_p and q_t below the inversion, are characteristics of a stratocumulus-capped mixed layer. One slight exception is P2S, in which mean cloud base is 32 m above the LCL, compared to half or less as much in all other runs. The LWP in the runs varies from 36-64 g m^{-2}, corresponding to a cloud thickness range of 202-254 m. Even the maximum LWP leads to insignificant precipitation at both cloud base and the surface in all S12 simulations.

The inversion height z_i (computed as the height where the mean relative humidity first decreases to 50%; also a good proxy for the mean stratocumulus top) varies by more than

[3]See Figure 4.7 for one such controlling parameter, a_2, though note that decreasing the cloud top also tends to strengthen the SWCRE in the CTL MLM.

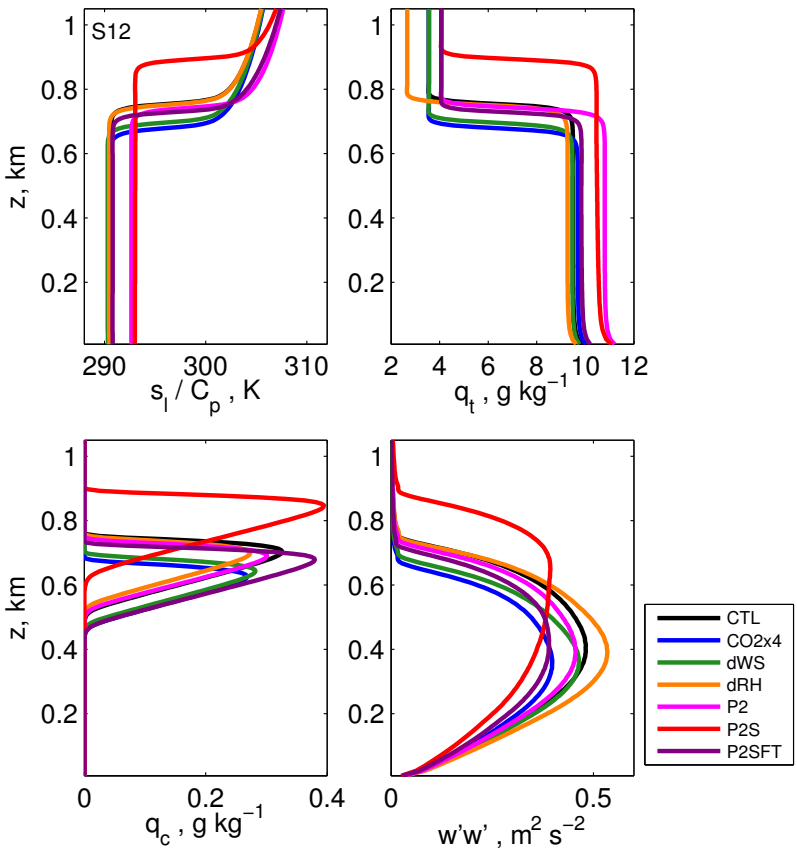

Figure 4.3: Steady-state profiles of s_l/c_p, q_t, q_l, and $\overline{w'w'}$ for LES control and sensitivity simulations

Table 4.3: Summary of steady-state LES S12 results[a]

S12 Run	z_i [m]	z_b [m]	LCL [m]	w_e [m s^{-1}]	SHF [W m^{-2}]	LHF [W m^{-2}]	ΔR [W m^{-2}]	Δb [m s^{-2}]	LWP [g m^{-2}]	SWCRE [W m^{-2}]
CTL	755	526	516	4.1	3.7	83	43	0.34	49	-152
CTLD	747	523	511	4.0	3.9	82	42	0.33	47	-123
4CO2	679	477	469	3.6	4.4	77	38	0.32	36	-133
dWS	696	487	482	3.8	6.8	77	42	0.33	39	-138
dRH	751	545	538	4.1	5.8	90	46	0.34	38	-137
P2	742	531	522	4.0	3.6	93	41	0.33	42	-139
P2D	736	531	520	4.0	3.5	92	40	0.33	40	-111
P2S	894	640	608	4.3	-0.3	97	39	0.34	63	-164
P2SFT	729	479	463	3.5	2.0	72	37	0.36	62	-164
dCMIP3	740	536	526	3.8	3.3	94	38	0.34	39	-134

Based on mean over days 8-10. All simulations have no surface precipitation and 99-100% cloud fraction. Here, z_i is the inversion height (defined as the lowest height at which horizontal-mean relative humidity drops below 50%, z_b is the cloud-base height (defined as the lowest level at which the fractional cloud cover exceeds half of its maximum value), LCL is the horizontal mean lifted condensation level of air 100 m above the surface, w_e is the entrainment rate, calculated as the difference of the z_i tendency and the collocated subsidence rate, SHF and LHF are the surface sensible and latent heat fluxes, ΔR is the net radiative flux divergence between the surface and 50 m above z_i, Δb is the inversion buoyancy jump measured from 50 m below to 50 m above z_i, and LWP is liquid water path.

[a] Reproduced from Table 3 of Bretherton et al. (2013).

200 m across the runs; those with higher cloud top also tend to have higher cloud base.

In steady state, the entrainment rate must balance the subsidence rate at the inversion height. All runs but P2S, P2SFT and dCMIP3 have the same subsidence profile, and the tabulated entrainment rate is proportional to the inversion height. The P2S and P2SFT runs have weaker subsidence at a given height; thus P2SFT has a 12% weaker entrainment rate than P2, but has nearly the same inversion height.

The sensible heat fluxes vary from 0-7 W m^{-2} across the runs, corresponding to an air-sea temperature difference of 0-1 K between runs. These fluxes are small, but do affect the heat budget and surface buoyancy flux in some of the runs. The latent heat fluxes vary by 25% across the runs.

Sensitivity of SWCRE and z_i

The left panel of Fig. 4.4 shows the SWCRE and z_i across the runs. Each color corresponds to a different added process. The dWS, dRH, 4CO2, and P2 runs are anchored off the control run. The P2S run is differenced with P2 to show the effect of reduced subsidence. The P2SFT run is differenced with P2S to show the effect of increased EIS. Aubsidence and EIS are the biggest drivers of z_i changes, but increases in the humidity gradient between the sea-surface and free troposphere (dRH and P2) can help drive cloud thinning (weaker SWCRE).

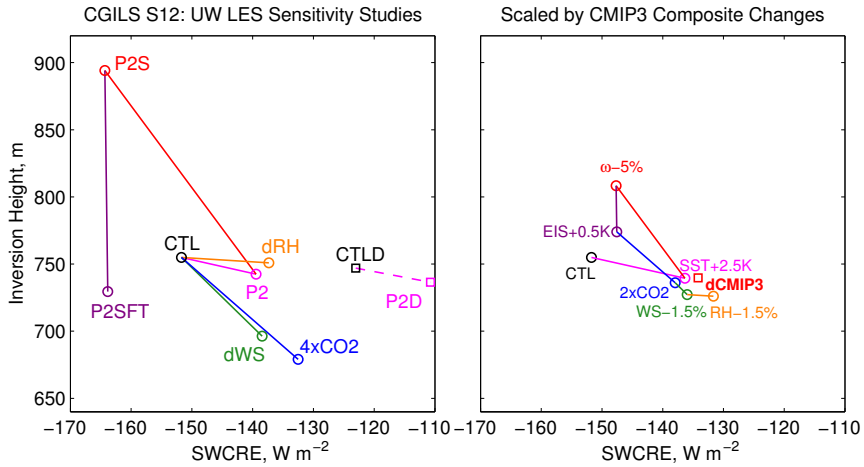

Figure 4.4: (a) Scatterplot of steady-state SWCRE and z_i for the LES control and sensitivity runs. Each sensitivity run is linked by a line segment to a run from which it is perturbed. Circles indicate diurnally-averaged runs; squares indicate runs including a diurnal cycle. (b) As in (a), but with perturbations sequentially added to the control run scaled to match their CMIP3 multimodel mean estimates from Table 1. The difference between the orange RH-1.5% circle and the black CTL circle shows the cumulative effect of all perturbations, assuming linear response. The red square shows the steady-state of the dCMIP3 run, in which all forcing perturbations have been added to the LES. The difference between the red square and the orange circle is a measure of the nonlinearity of the cloud response to the CMIP3 2xCO_2 combined climate perturbation.

In the right panel of Fig. 4.4, the changes due to each process have been rescaled by the CMIP3 multimodel mean estimate for CO_2 doubling given in Table 4.2. Assuming linearity, the cumulative effect of all perturbations is to move from the control (black circle) state, sequentially adding the scaled effects of SST increase, subsidence decrease, EIS increase, CO_2 doubling, decreased wind speed, and decreased free-tropospheric relative humidity, to

arrive at the orange circle, at which SWCRE is 20 W m^{-2} weaker and the inversion is 25 m lower than for the control. The increased absolute humidity gradient (due mainly to the Clausius-Clapeyron effects of the P2 warming at fixed relative humidity, with a minor additional contribution from the slight RH decrease) is seen to be the most important driver of the cloud radiative response, and the CO_2 increase is also a substantial contributor. The subsidence decrease is its most important counterbalance. The small inversion height decrease results from a balance between increases in CO_2 and EIS, which shallow the inversion, and reduced subsidence, which deepens it.

The red square labelled dCMIP3 in Fig. 4.4b shows the steady-state reached by the LES with the combined CMIP3 forcing perturbations added to the control case. The distance on the plot between the red square and the orange circle is a test of the linearity of the cloud and boundary layer depth responses to the full CMIP3 set of forcings. Since this distance is much smaller than between the red square and the control case, we conclude the linearity assumption is reasonable for S12, even though some of the individual perturbations were much larger than their dCMIP3 analogues.

4.4.3 Comparison of LES with MLM

Since the LES gives a well-mixed boundary layer, there is hope that a MLM will exhibit similar cloud responses for the S12 cases. This is not guaranteed, because the MLM response depends on its entrainment closure, whose sensitivities may not be the same as the LES, and because even subtle perturbations from well-mixedness can affect cloud thickness. Caldwell and Bretherton (2009) compared the MLM cloud response to analogous perturbations in a fairly similar stratocumulus regime using two rather different entrainment closures, and found it was not highly sensitive to which closure was selected. Uchida et al. (2010) showed that the sensitivity of the SAM LES to perturbations in cloud droplet number concentration was well predicted by a MLM very similar to the one used in this study, as long as two adjustable parameters governing the sensitivity of the entrainment closure to evaporative enhancement and droplet sedimentation were appropriately chosen. Both of these studies lend hope that the MLM and LES responses will be comparable.

Figure 4.5 shows steady-state thermodynamic and buoyancy flux profiles from the MLM, emphasizing their similarity to the LES profiles shown in Fig. 4.3. The radiatively-driven enhancement in stratification of s_ℓ/c_p above the inversion is evident in Fig. 4.5a, and the moist-adiabatic MLM q_ℓ profiles in Fig. 4.5d look remarkably like their LES counterparts. Table 4.4 summarizes relevant statistics from the MLM simulations that are analagous to the LES results in Table 4.3. Each simulation had a buoyancy integral ratio (BIR; see Bretherton and Wyant, 1997) of zero, indicating that the boundary layer remained well-mixed throughout. Compared to the LES, the MLM simulates a nearly identical buoyancy jump across the inversion. The LHF in the MLM tends to be 3–5 W m^{-2} higher than the LES, while the SHF is 0–2 W m^{-2} higher. This discrepancy could be partly corrected by making a different choice for the surface transfer coefficient, but this does not appreciably alter the findings.

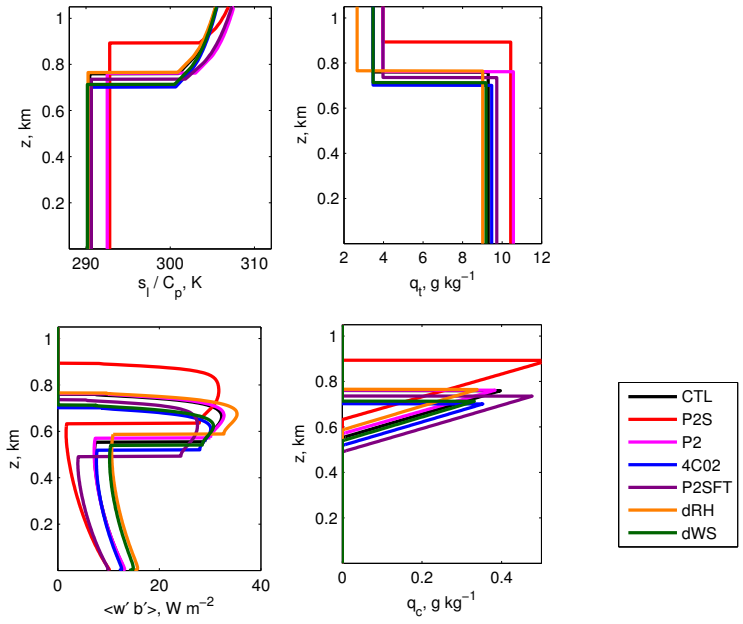

Figure 4.5: Steady-state profiles of s_ℓ/c_p, q_t, bouyancy flux in energy units, and q_ℓ for MLM control and sensitivity simulations, for comparison with Fig. 4.3.

Table 4.5 distills results from Table 4.3 and Table 4.4 into a comparison of the inversion height, LWP and SWCRE responses for the two models. The control states are quite

Table 4.4: Summary of steady-state MLM results.

S12 Run	z_i [m]	z_b [m]	w_e [m s^{-1}]	SHF [W m^{-2}]	LHF [W m^{-2}]	ΔR [W m^{-2}]	Δb [m s^{-2}]	LWP [g m^{-2}]	SWCRE [W m^{-2}]
CTL	760	553	4.0	5.2	86	44	0.34	47	-147
CTLD	766	562	4.1	4.7	86	44	0.34	45	-121
4CO2	701	518	3.8	5.1	82	40	0.33	37	-133
dWS	713	539	3.8	7.2	80	43	0.34	33	-128
dRH	765	587	4.1	7.0	93	47	0.35	34	-132
P2	762	570	4.1	4.4	97	43	0.34	42	-138
P2D	768	580	4.1	3.9	97	42	0.34	40	-111
P2S	893	632	4.2	1.5	100	40	0.34	75	-172
P2SFT	735	490	3.5	3.3	75	38	0.37	67	-165
dCMIP3	768	578	3.9	3.7	98	40	0.34	41	-138

As in Table 4.3, but for the MLM rather than LES. Based on mean over days 8-10. Here, z_i is the inversion height, z_b is the cloud-base height (equal to the LCL), w_e is the entrainment rate, SHF and LHF are the surface sensible and latent heat fluxes, ΔR is the net radiative flux divergence between the surface and 50 m above z_i, Δb is the inversion buoyancy jump measured from 50 m below to 50 m above z_i, and LWP is the liquid water path.

Table 4.5: Comparison of steady-state S12 MLM and LES results

	z_i [m]		LWP [g m^{-2}]		SWCRE [W m^{-2}]	
Run	MLM	LES	MLM	LES	MLM	LES
CTL	**760**	**754**	**47**	**49**	**-147**	**-152**
	Δ		Δ		Δ	
4CO2	-58	-76	-10	-13	14	19
dRH	5	-4	-12	-11	15	14
dWS	-47	-54	-14	-10	20	14
P2RAD0	-16		-3		4	
P2	2	-12	-5	-7	9	12
P2S	133	139	29	14	-25	-13
P2SFT	-24	-25	20	13	-18	-12
dCMIP3	8	-15	-6	-8	9	18

Based on mean over days 8-10. Except for CTL, values are *differences* of each simulation from CTL.

similar, and the sensitivities to all the perturbations have the same sign, and in most cases a similar magnitude, for the LES as for the MLM. The important implication is the LES cloud response to the climate perturbations tested for S12 should largely be explainable using mixed-layer mechanisms.

The most notable quantitative discrepancy is for the P2S case, in which the LWP increase is twice as large for the MLM as for the LES; in the P2SFT case the LWP of the MLM cloud also increases 50% more than in the LES. This reflects a very slight decoupling of the LES-simulated boundary layer in these cases. From Table 4.3, the mean cloud base is 5-10 m higher than the mean lifted condensation level (LCL) at 100 m altitude, except for the P2S and P2SFT cases, for which this difference rises to 30 m and 15 m, respectively. This difference is indicative of a slight drying of the boundary layer with height not included in the mixed-layer approximation, and corresponds to a decrease of LES cloud thickness and LWP compared to the MLM prediction. Thus, even in this most ideal of well-mixed boundary layer regimes, the cloud response of an LES to some forcing perturbations can deviate quantitatively from mixed layer behavior.

Within the MLM, decoupling would be indicated by a region of negative buoyancy flux below the cloud base (Bretherton and Wyant, 1997). Figure 4.5c shows that this does not occur for any case in this study, but it is notable that P2S and P2SFT have the smallest subcloud buoyancy minima of these studies, adding further evidence to the decoupling-induced discrepancy between MLM and LES in these cases.

Fig. 4.6 shows the MLM inversion height and SWCRE sensitivities of the MLM for comparison with its LES counterpart, Fig. 4.4. As in the LES, the dCMIP3 run is in reasonable agreement with the appropriately scaled linear superposition of each individual sensitivity, though the discrepancy is somewhat larger for the MLM, and the inversion deepens slightly in the dCMIP3 case whereas the linear superposition of forcings would suggest a shallowing.

By varying a_2, the MLM can be tuned to produce a range of steady-state LWPs and inversion heights for the S12 control case, as shown in Fig. 4.7. The choice $a_2 = 60$ approximately matches SAMA, and the range $a_2 = 30 - 120$ spans the range of LWP produced by the CGILS LES models in Blossey et al. (2013). The figure also shows that the

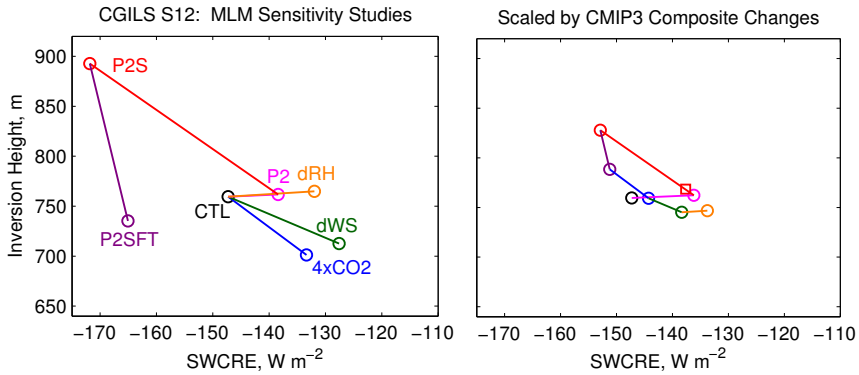

Figure 4.6: As in Fig. 4.4, except for MLM.

warming response, as measured by the P2 - CTL difference in inversion height, SWCRE, and liquid water path, is rather insensitive to a_2, suggesting that the MLM sensitivities to climate perturbations do not strongly depend on details of the entrainment closure.

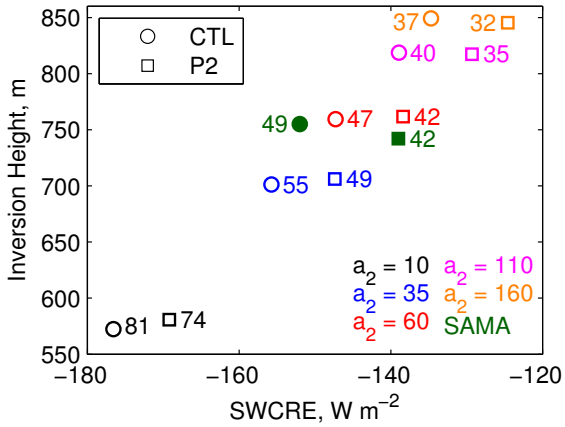

Figure 4.7: Sensitivity of MLM-simulated S12 steady state SWCRE and z_i to evaporative enhancement parameter a_2 in the entrainment closure for CTL (circles) and P2 (squares). The numbers by each symbol show the corresponding liquid water paths in g m^{-2}. Green filled symbols show the SAMA LES results for comparison.

4.5 Discussion of sensitivities to different processes

This section develops a mechanistic understanding of the responses of boundary layer depth and cloud thickness to the climate-change relevant perturbations probed by the different sensitivity studies. Fig. 4.8 presents a brief synthesis of these findings.

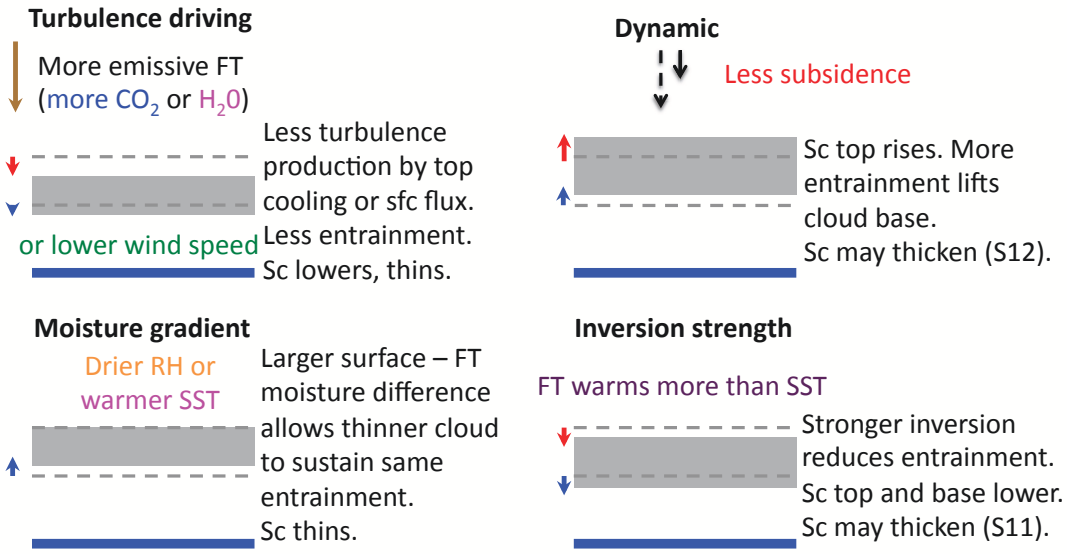

Figure 4.8: Schematic description of response of a stratocumulus-capped boundary layer to several forcing perturbations that might accompany global warming: (a) Changed driving of turbulence due to less radiative cooling ($4xCO_2$) or lower wind speed, (b) Changed humidity gradient between the sea-surface and the free troposphere, due to tropics-wide surface warming and constant free-tropospheric relative humidity, or due to reduced free-tropospheric relative humidity, (c) Subsidence decrease, (d) Increased inversion strength.

4.5.1 CO_2 quadrupling

In experiment 4CO2, the concentration of CO_2 is quadrupled from the control simulation. The horizontal temperature advection in the free troposphere is modified to maintain a steady-state radiation-advection balance that keeps the above-inversion reference temperature profile similar to the control simulation. The increased CO_2 adds about 10 W m^{-2} to the downwelling longwave radiation at the inversion, which reduces the radiative cooling and turbulence levels of the stratocumulus-topped mixed layer both in the LES and the

MLM. This decreases the entrainment rate, leading to a gradual lowering of the inversion and a thinning of the cloud layer (Table 4.5). A schematic of this mechanism is shown in Fig. 4.8a. Section 4.5.4 includes a more detailed MLM analysis of how the cloud thickness and turbulence generation respond to a change in downwelling radiation. A satellite-based study of the effects of overlying cirrus on stratocumulus cloud layers by Christensen et al. (2013) provides observational support for this mechanism. They found that under optically thick cirrus, which increase downwelling longwave radiation, stratocumulus cloud cover, inversion height, and precipitation all decrease.

4.5.2 Reduced wind speed

Sensitivity study dWS shows the effect of a 10% reduction in the imposed wind speed at all heights. This reduces the LHF. The boundary layer also cools slightly, such that the SHF actually increases (Webb and Lock, 2012, found the opposite result in their full-GCM simulation, perhaps due to compensating effects from other regional forcing changes). The reduced LHF must be balanced by reduced entrainment drying; indeed steady-state entrainment is reduced 7% and the inversion drops 59 m in the LES (47 m in the MLM). As the inversion drops, the cloud thins. The reduced surface driving of turbulence in dWS has a similar effect as the reduced radiative driving of turbulence in 4CO2, as indicated in Fig. 4.8a, acting mainly on the slow adjustment timescale of the inversion height.

From the perspective of the MLM, the mechanism can be understood by considering the steady-state CTL solution that is then subject to decreased wind-speed. This decreases the LHF and SHF initially by the same fraction. The decreased LHF reduces the size of the cloudy contribution to the integrated buoyancy flux (and thus w_*), and the rise in cloud base thins the cloud and contributes to decreasing the entrainment rate until the decreased moisture flux is again balanced by a compensating decrease in entrainment drying. The decreased entrainment lowers the cloud top on the slow inversion adjustment timescale (Chapter 5), thus supporting a shallower, thinner cloud.

In dWS the profiles of horizontal advection of temperature and humidity are unchanged from the control case. If horizontal SST gradients and boundary layer temperature and

moisture gradients remained fixed, a wind speed reduction would cause horizontal cold and dry advection to decrease within the boundary layer. That would further reduce boundary layer turbulence and might amplify the cloud thinning.

4.5.3 Free-tropospheric RH decrease

In many climate models, there is a slight free-tropospheric decrease in mean relative humidity in the subtropical subsidence regions in a CO_2-warmed climate. Experiment dRH assesses the possible consequences of this effect on boundary layer stratocumulus, by reducing the free tropospheric relative humidity from 30% to 25% in the S12 control simulation. In both the LES and the MLM, the steady-state response is a significant (10%) cloud thinning associated with a rise of cloud base and much less change of cloud top (see Tables 4.3 and 4.4). The entrainment rate is unchanged, but entrainment drying increases.

The drier boundary layer in dRH also has a nearly 10% larger LHF and a slightly larger SHF. The increased surface fluxes drive stronger subcloud turbulent buoyancy production. The larger LHF also helps drive larger in-cloud buoyancy fluxes compared to CTL (See Bretherton and Wyant, 1997, and also Sec. 4.5.4). In combination, these allow a 10% thinner cloud in dRH to support as much turbulence as in the control case. These effects are both reflected in the MLM buoyancy flux profiles shown in Figure 4.5c. A schematic of this mechanism is shown in Fig. 4.8b. It is fundamentally driven by an increased humidity difference between dry free-tropospheric air and saturated air at the sea-surface temperature.

The drier free troposphere is also less emissive, so the net radiative cooling of the boundary layer slightly increases. This extra cooling is not compensated by more entrainment warming, but instead lowers the boundary layer temperature and slightly increases sensible heat fluxes.

4.5.4 Tropics-wide 2 K SST increase

Blossey et al. (2013) compared the S12 response of several LESs to a 2 K warming of both local and ITCZ SST with unchanged subsidence (P2) and strongly reduced subsidence (P2S). Here the SAMA simulations and MLM are used to gain further insight into their

behavior.

Unchanged subsidence (P2)

With unchanged subsidence, SAMA and the MLM simulate a reduction in cloud thickness and LWP with little change in inversion height or entrainment rate. This sensitivity is important because it is a strong contributor to the overall dCMIP3 change in cloud properties, but it proves subtle to fully understand.

We attribute the cloud thinning in P2 to a combination of reduced radiative driving of turbulence and Clausius-Clapeyron driven effects of the larger absolute humidity jump across the inversion. The warmer P2 free troposphere contains more water vapor, and hence is somewhat more emissive. This reduces the net radiative cooling of the cloud-topped boundary layer by approximately 2 W m^{-2}, or 5%, compared to the control (Tables 4.3 and 4.4). The absolute humidity in the boundary layer increases rapidly as it warms, while the absolute humidity of the free troposphere increases much less, inducing a 12% increase in the inversion humidity jump.

The MLM can be used to separate these effects and analyze their consequence for the cloud-topped boundary layer. To this end, an intermediate case, RAD0, is constructed with only the radiative driving reduced to match P2. This is done by inserting an elevated free-tropospheric moist layer into the control case that artificially increases the downwelling radiation on the boundary layer top in the control case by 2 W m^{-2}. Table 4.5 compares the equilibrium LWP and equilibrium inversion height of RAD0 and P2 to the control case. All three simulations have the same mean subsidence profile, so changes in equilibrium inversion height between these simulations are a proxy for changes in entrainment rate. RAD0 has a slightly lower inversion than CTL and P2, and its LWP reduction from CTL is half that of P2. We conclude that the reduced radiative driving and the thermodynamic (non-radiative) effects of warming contribute comparably to the cloud thinning in P2.

The changes in LWP and inversion height from CTL to RAD0 are approximately 25% as large as for 4CO2. This is expected, because quadrupling CO_2 increases downwelling longwave radiation at a fixed reference inversion height by approximately four times as

much as imposed in RAD0.

P2 cloud thinning, entrainment, and buoyancy flux profiles

Both the radiative and thermodynamic effects work in part by changing the entrainment rate, because there are strong feedbacks between entrainment rate and cloud thickness, mediated by buoyancy production of boundary-layer turbulence (Zhu et al., 2005). The result is a boundary layer in which the cloud thinning tendency due to entrainment warming and drying is in approximate balance with the cloud thickening tendency driven by other forcings such as radiation, surface fluxes and horizontal advection. The interplay between perturbations of forcings, buoyancy production of turbulence, entrainment and cloud thickness can usefully be explored within the simplicity of the MLM. The MLM entrainment closure is

$$w_e = A\langle\overline{w'b'}\rangle/\Delta b, \tag{4.1}$$

where A is a nondimensional entrainment efficiency that depends on thermodynamic jumps and liquid water content at the inversion, Δb is the inversion buoyancy jump, $\overline{w'b'}(z)$ is the horizontally averaged turbulent buoyancy flux, and angle brackets denote a vertical average over the boundary-layer depth. Changes in A only play a minor role in explaining differences between the three cases, so that Δb and the boundary-layer average buoyancy flux $\langle\overline{w'b'}\rangle$ are the main controls on entrainment.

Fig. 4.9 compares the MLM equilibrium buoyancy flux profiles and gives $\langle\overline{w'b'}\rangle$ for the CTL, RAD0, and P2 cases. The buoyancy flux profiles are all very similar below cloud base; differences in $\langle\overline{w'b'}\rangle$ between the cases are mainly due to the cloud layer, where there is an additional contribution to the buoyancy flux proportional to the upward liquid water flux. Either a thinning of the cloud layer or a decrease in $\overline{w'b'}$ within the cloud layer will produce lower $\langle\overline{w'b'}\rangle$. Comparing RAD0 to CTL , both effects are evident in response to the reduced cloud-top radiative cooling , but the cloud thinning is more important in reducing $\langle\overline{w'b'}\rangle$ by 1%. Comparing P2 to RAD0, the in-cloud $\overline{w'b'}$ increases, but further thinning of the cloud layer more than compensates to reduce $\langle\overline{w'b'}\rangle$ by 1% more. In both cases, boundary-layer average turbulence generation is reduced mainly through cloud thinning.

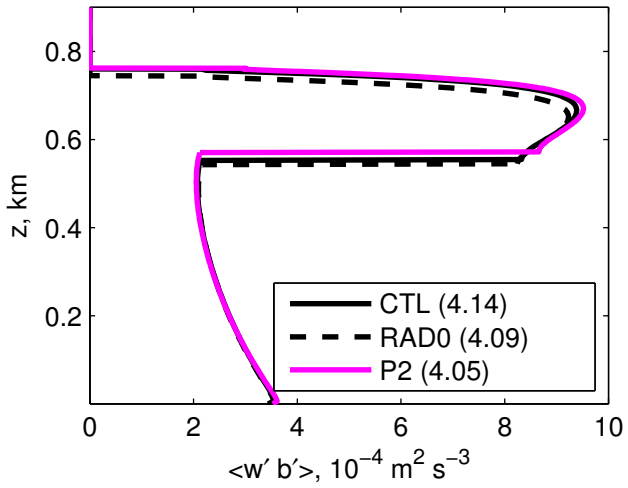

Figure 4.9: Steady-state MLM profiles of $\overline{w'b'}$ for S12 control, RAD0, P2 simulations. The number in the legend for each case is the vertically-averaged buoyancy flux $\langle\overline{w'b'}\rangle$.

Thermodynamic cloud-thinning mechanisms in P2

The comparison of P2 to RAD0 isolates the thermodynamic effects of the 2 K warming of the profile, with no change in radiative driving. As noted above, due to Clausius-Clapeyron scaling the P2 case has a larger inversion humidity jump than CTL and RAD0 (Fig. 4.5). This helps thin the cloud in two ways. First, the "virtual" effect of this humidity jump on air density contributes to a 1–2% reduction of the inversion buoyancy jump Δb in P2 compared to RAD0. Hence P2 recovers to the same entrainment rate as CTL, which is larger than for RAD0. This increases entrainment drying and warming compared to RAD0, which helps thin the cloud and also counteracts more of the cloudtop radiative cooling, reducing turbulence generation $\langle\overline{w'b'}\rangle$.

A second cloud thinning mechanism is associated with the slight increase of buoyancy flux averaged across the cloud layer in P2 compared to RAD0 that can be seen in Fig. 4.9. This allows a given vertically-integrated buoyancy production of turbulence to be accomplished by a thinner cloud layer. Specifically, assuming no change in subcloud buoyancy flux, $\overline{w'b'}$ in the cloud layer can be tied to a scaled cloud-base latent heat flux which increases in P2 due to the larger humidity difference between the sea-surface and the free troposphere in a

warmer climate. Following Eq. (9) of Bretherton and Wyant (1997),

$$\overline{w'b'}(z_b^+) = \beta\overline{w'b'}(z_b^-) + \frac{g\sigma}{s_{v0}}L\overline{w'q_t'}, \tag{4.2}$$

where z_b^+ is a height just above the cloud base, z_b^- is a height just below the cloud base, s_{v0} is a reference value of boundary-layer virtual static energy, and

$$\sigma = \beta\mu - \epsilon \approx 0.35 \tag{4.3}$$

is a nondimensional temperature-dependent thermodynamic coefficient defined by Bretherton and Wyant (1997). Here $\epsilon = c_pT/L$, $\mu = 1 - 0.608\epsilon$ and $\beta = (1 - 1.608\epsilon)/(1 + [L/c_p]\partial q_s/\partial T)$, where $q_s(p, T)$ is the saturation water vapor mixing ratio.

The first term on the right-hand side of (4.2), proportional to the subcloud buoyancy flux, is nearly identical in the three runs. Differences between the simulated $\overline{w'b'}$ above cloud base derive from the second term, which is a scaled cloud-base latent heat flux. As predicted by Clausius-Clapeyron scaling, P2 has an 12% latent heat flux increase in the cloud layer compared to RAD0 or CTL (similar to the P2-CTL increases in humidity jump in Fig. 4.5b and in the surface latent heat flux from Table 4.3). This is partly compensated by decrease of 4% per kelvin in σ, yielding a 3% cloud-layer mean buoyancy flux increase from RAD0 to P2.

The two mechanisms described above, resulting from the larger vertical humidity gradient due to Clausius-Clapeyron scaling in a warmer climate, allow a thinner cloud layer to drive a given entrainment rate through an inversion with a given temperature jump. That is, the humidity gradient mechanism for stratocumulus cloud response shown in Fig. 4.8b for the dRH case also applies to the differences between P2 and RAD0, and explains the thermodynamically-driven half of the LWP decrease between CTL and P2.

Reduced subsidence (P2S)

With reduced subsidence, the cloud top and base rise and the cloud thickness and LWP *increase*, in both SAMA and the MLM. This is consistent with the subsidence-lapse-rate

mechanism discussed by Caldwell and Bretherton (2009). Reduced subsidence thickens the cloud relative to the P2 case because of the cloud top rise; as the cloud thickens it entrains slightly more, which adds to the cloud top rise and also lifts cloud base. A steady state is achieved once subsidence and entrainment balance. A schematic of this mechanism is shown in Fig. 4.8c. Myers and Norris (2013) find observational support for enhanced low-latitude boundary-layer cloud cover under reduced subsidence after controlling for EIS, based on several datasets, lending further plausibility to this mechanism.

Decoupling in P2 and P2S

Bretherton and Wyant (1997) performed a mixed layer model analysis of the conditions that would favor persistent decoupling of a stratocumulus-capped mixed layer. Their analysis suggests that decoupling is favored by smaller values of the ratio of boundary-layer radiative flux divergence ΔR to $\sigma \cdot$LHF, and by a larger ratio of the LCL to the inversion height (a nondimensional measure of well-mixed stratocumulus thickness).

In a warmer climate, we have argued that LHF increases faster than the thermodynamic coefficient σ decreases, and ΔR slightly decreases. Together, these factors favor decoupling. However, in P2 they are counteracted by the slight thinning of the cloud layer, which favors well-mixedness. Hence, P2, like CTL, remains well-mixed in both LES and MLM. This can also be seen in the MLM buoyancy flux profiles for CTL and P2 in Fig. 4.9, which show a positive buoyancy flux minimum below cloud base (consistent with a well-mixed boundary layer) in both cases. Run P2S, on the other hand, develops a slight (32 m) difference between the LCL and the mean cloud base in the LES, an indicator of nascent decoupling also visible in the flattening of the maximum in its vertical velocity variance profile shown in Fig. 4.3d. The thicker cloud layer induced by the inversion deepening in P2S favors decoupling, reinforcing the thermodynamic effects of the warming.

Although the MLM remains well-mixed in all cases, the buoyancy flux profiles in Figure 4.5c exhibit the trend toward decoupled conditions for P2S and P2SFT described here. Further sensitivity studies in which the a_2 parameter of the entrainment efficiency is systematically varied find that increasing a_2 to 110 generates a negative subcloud buoyancy

flux in both P2S and P2SFT, though not for the other runs.

4.5.5 Response to EIS increase

In experiment P2SFT, the free troposphere is warmed and subsidence is reduced as in P2S, but local SST is not increased. Hence the inversion strengthens and shallows compared to P2S, while entrainment is reduced. The reduced entrainment drying drops the steady-state cloud base, leaving the cloud thickness almost unchanged, and reduces decoupling as measured by the cloud base-LCL difference. A schematic of this mechanism is shown in Fig. 4.8d. This is different than observed climatology in the subtropical marine stratocumulus regimes, perhaps due to episodes of broken cloud, clearing or non-mixed layer behavior whose frequency is correlated with EIS, effects not included in the S12 case setup. Combining Figs. 1 and 2 of Klein and Hartmann (1993), with Fig. 6b of Wood and Bretherton (2006), our observational estimate is that SWCRE increases by 5 W m^{-2} for every 1 K EIS increase over the subtropical and midlatitude oceans.

4.5.6 Synthesis of responses

Of the four types of stratocumulus response shown in Fig. 4.8, these simulations suggest that subsidence reduction thickens a well-mixed Sc layer, an EIS increase has little impact on well-mixed Sc thickness, while reduced radiative or surface driving of turbulence and increased humidity gradients thin the cloud in a CO_2-warmed climate. Since there are several offsetting cloud response mechanisms, all involving turbulent processes not resolved in climate models, it is not surprising that low cloud feedbacks are a challenging problem for climate models, even in the conceptually simplest case of a well-mixed stratocumulus layer.

4.6 Discussion and conclusions

We have systematically examined climate change sensitivities of subtropical stratocumulus-topped boundary layers using both an LES and MLM. This study is built around the CGILS model intercomparison S12 case, and complements SAMA LES results shown in Bretherton

et al. (2013), as well as those of Blossey et al. (2013) from an international group of LES on a much more limited set of cases. The control simulation evolves into a quasi-steady state, which can take 10 days or more. The forcings are then perturbed in various ways that might accompany climate change, including changes in temperature, CO_2 concentration, relative humidity, subsidence, inversion stability, and wind speed. By separating these changes and assuming they can be approximately linearly superposed to predict the cloud radiative response to multiple forcing changes, we can infer the MLM- and LES-predicted cloud response to a broad range of possible climate change forcings. In particular, we can estimate the cloud response to a CMIP3 multimodel mean forcing change for some particular greenhouse gas emissions scenario, e. g. CO_2 doubling. Our LES responds similarly to other LESs for the smaller set of forcing perturbations considered in CGILS (Blossey et al., 2013); this adds credibility to its simulated cloud response for the broad suite of forcings that we consider. Furthermore, the MLM generally responds similarly to the LES, which allows the use of mixed-layer arguments to explore and explain the observed sensitivities.

These models predict a reduction in shortwave cloud radiative effect (positive shortwave cloud feedback) for the CMIP3 $2\times CO_2$ forcing perturbations. The simulated CTL mean SWCRE is approximately 150 W m^{-2} and the $2\times CO_2$ SWCRE reduction induced by the CMIP3 forcing changes is more than 10 W m^{-2}, and somewhat larger in the LES. The mean SWCRE is somewhat overestimated compared to observed climatology, due largely to biases in the CGILS solar zenith angle specification, neglect of the diurnal cycle of insolation, and neglect of transient forcing variability.

This approach allows the CMIP3 response to be partitioned into effects from individual forcing changes, which combine approximately linearly. The positive feedback from SWCRE reduction comes mostly from cloud thinning due to the overall warming of the profile induced by higher tropical SSTs, together with the direct radiative effect of increased CO_2. Reduced subsidence due to weakening of tropical overturning circulations partly counteracts these two factors. Changes in wind speed, inversion stability, and free-tropospheric relative humidity have smaller, but non-negligible, impacts on the cloud thickness. The competition between reduced subsidence, which tends to lift the inversion in a warmer climate, and increased inversion stability and CO_2, which causes the inversion to shallow, is reflected in a slight

predicted reduction in stratocumulus-top height in the LES, but slight increase in the MLM.

We identified several physical mechanisms of cloud sensitivity to the climate change perturbations that we investigated. These included changes in radiative driving of cloud-topped boundary layer turbulence associated with a more emissive free troposphere, thinning of stratocumulus layers in the presence of an enhanced humidity gradient between the surface and free troposphere, a general thickening of stratocumulus due to lifting of the cloud top if subsidence is reduced, and a lowering of the inversion and possible thickening of the cloud layer if the inversion is strengthened. These mechanisms apply both to LES of the well-mixed and cumulus-under-stratocumulus boundary layers (see Bretherton et al., 2013, for the decoupled boundary layer mechanisms), with some quantitative differences, and they also apply to mixed layer model simulations of the well-mixed stratocumulus layer. Of these mechanisms, the increased lower-tropospheric humidity gradient (also noted by Brient and Bony, 2013, for shallow cumulus) and reduced radiative driving (noted by Caldwell and Bretherton (2009) for well-mixed stratocumulus) seem to be most important in explaining the cloud thinning and positive cloud feedbacks simulated in both stratocumulus locations.

As mentioned in Sec. 4.1, Caldwell and Bretherton (2009) found using a mixed layer model that a warmer climate would favor stratocumulus thickening due to weaker mean subsidence and a stronger inversion. Xu et al. (2010) used an LES for climate-change sensitivity studies that were prototypes for the CGILS CTL and P2S cases, and simulated increased cloud and negative cloud feedbacks for the P2S case at the S12 location. We use a nearly identical MLM and a comparable LES approach but reach the opposite conclusion that the cloud feedbacks are positive.

One reason is that the P2S case also does not include the effect of increased CO_2 radiative forcing, which we find erodes cloud. Another reason is that the CMIP3 models predict a subtropical-mean subsidence decrease in the warmer climate that is only half as large as the northeast Pacific value assumed by Xu et al. (2010) and the standard P2S case on which CGILS focused. Note that in reality, the dynamics governing mean subsidence over the low-latitude oceans are a complex mixture between locally and nonlocally driven processes, including radiative cooling in and above the boundary layer, land-ocean temperature contrast, eddy heat and moisture fluxes in the Hadley circulation, etc. These dynamics appear

to also help modulate subtropical boundary layer cloud feedbacks.

Xu et al. (2010) also used profiles of horizontal temperature and moisture advection that do not produce realistic drying and cooling within the boundary layer, which has spurious effects on the sensitivity of the inversion height and cloud structure to climate perturbations. The appropriate specification of horizontal advective forcing and its sensitivity to climate perturbations remains a major challenge to Eulerian LES-based studies of boundary-layer cloud feedbacks, because there is a strong interaction between the advective forcings (which must be specified), the inversion height (which must be predicted) and the horizontal slope of the inversion.

Our findings are broadly consistent with the subtropical low cloud feedbacks simulated by the CMIP3 suite of global climate models, which were found to mostly be positive, though with large intermodel scatter in amplitude (Bony and Dufresne, 2005; Soden and Vecchi, 2011). We speculate that the scatter is in part due to competing physical mechanisms, some of which decrease cloud thickness and fraction, and some of which increase them. Our SWCRE changes in the stratocumulus regimes are larger than the CMIP3 multimodel mean, but we have given reasons why they might be expected to be overestimates; in particular transient forcing variability (Zhang et al., 2013; Brient and Bony, 2013) is likely to smear the cloud responses across geographical regimes and thus dilute local maxima and minima.

The CGILS experiment and the sensitivity studies we have presented highlight the multifaceted nature of cloud feedbacks on climate, involving compensating physical processes. Past LES-based studies of boundary layer cloud responses to climate change have used a range of approaches and idealizations for specifying climate change forcing perturbations, with major impacts on their results. Predicted cloud feedbacks would be much more negative with the setup of Zhang and Bretherton (2008) and Xu et al. (2010), due to their strong subsidence reduction and lack of CO_2 radiative forcing, than for the CMIP3 forcing perturbations. Our LES sensitivity studies, augmented by further MLM analysis, provide a firmer physical basis for climate model predictions that subtropical stratocumulus feedbacks on climate are positive. However, it is important to devise further observational tests of the physical mechanisms of cloud response that LES suggest are most important to climate change, especially the potential roles of reduced radiative driving and enhanced humidity

differences in thinning clouds in a warmer climate.

Chapter 5

STRATOCUMULUS RESPONSE TIMESCALES IN MLM AND LES

I use a mixed-layer model (MLM) and the SAMA large eddy simulation (LES) to analyze the timescales of response in a stratocumulus-topped boundary layer. Using the MLM, I find three separate timescales: a slow adjustment timescale associated with boundary layer deepening (several days), an intermediate thermodynamic timescale (approximately 1 day), and a fast time scale (6-12 hours) for cloud water path adjustment associated with internal entrainment rate feedbacks. The thermodynamic and inversion-deepening timescales are well-established in the literature (e.g., Schubert et al., 1979b; Bretherton et al., 2010), so the focus of this chapter is in the interpretation of the fast timescale. Two separate case studies are analyzed using both MLM and LES to explore the fast timescale.

First, the idealized DYCOMSII–RF01 case study (Zhu et al., 2005) is used to establish and physically motivate the nature of the fast timescale with the MLM. The role of the entrainment closure is investigated by repeating the analysis with several different closures. With the exception of the "minimal" (energy balance) closure (Lilly, 1968; Bretherton and Wyant, 1997), each closure considered exhibits a short timescale. Applying a perturbation to the free troposphere relative humidity shows that this fast adjustment occurs also in LES.

Temperature and CO_2 perturbations are applied to the CGILS S12 case in both the MLM and SAMA LES. The CO_2 perturbation does not project strongly onto the fast scale, suggesting that purely radiative perturbations do not elicit a fast response. Perturbing the surface and atmosphere temperatures by 2K does project strongly onto the fast scale, and much of the difference in LWP between the control and warmed climate is established within the first 12 hours of simulation. We propose this is due to an entrainment-liquid flux adjustment, and suggests a cloud-thinning feedback mechanism in response to a uniformly warmed climate.

5.1 Introduction

In order to understand how a stratocumulus-topped boundary layer (STBL) will respond to changing large scale conditions, it is important to understand the characteristic time scales on which aspects of the STBL respond. Indeed, since real STBLs are subject to large scale forcings across a range of time scales, it is important to consider how quickly a STBL responds to changing conditions – i.e., to what extent it retains "memory" of its history.

Traditionally the MLM has been interpreted to admit only two timescales. Schubert et al. (1979b) used a mixed-layer model (Schubert et al., 1979a) to analyze perturbations in SST and large scale subsidence to a STBL starting from steady-state, and observed that the thermodynamic variables (i.e., h, q_t, and z_b) adjusted with an e-folding time of approximately 4 hours, while the inversion approached steady state on a much slower timescale of approximately 80 hours. They identified that the thermodynamic adjustment was driven primarily by the surface flux, and argued that the thermodynamic adjustment timescale could be approximated as $z_i/C_T V \approx 1$ day, while the inversion deepening adjustment timescale is determined entirely by the large scale divergence as

$$\tau_i = D^{-1}. \tag{5.1}$$

It is relevant to note that the observed cloud base adjustment time of 4 hours that the authors observe is quite a bit faster than the suggested surface-driven fast scale, hinting at the existence of a scale faster than the thermodynamic adjustment scale, even in this early study.

Bretherton et al. (2010) expanded on this notion of a "fast" thermodynamic timescale,

$$\tau_{\text{th}} = \frac{z_i}{w_e + C_T V}, \tag{5.2}$$

and a "slow" inversion-deepening timescale, and exploited this scale separation to perform a slow manifold analysis in both MLM and LES. On the so-called "slow manifold" the dynamics can be simplified by assuming the trajectory is controlled by the evolution of z_i. The thermodynamic variables remain in local quasi-equilibrium, their evolution slaved to

the inversion through the slowly-varying entrainment rate that can be approximated as a function of z_i alone along the slow manifold.

Recently, further attention has been given to boundary layer adjustment timescales, particularly the fast timescale. van Driel and Jonker (2010) applied a timescale analysis to dry convective boundary layers driven by specified surface flux. Their analysis is similar in spirit to that undertaken in this chapter. They used a MLM of the dry convective boundary layer and extracted the timescales by solving for the steady-state, linearizing the system about that steady state, and calculating the eigenvalues. They then subjected the linearized equation, an MLM, and an LES to sinusoidally-varying perturbations in the surface flux, and compared the resulting z_i amplitude and phase lag relative to the input forcing. They noted that the timescales were dependent on the entrainment efficiency, and showed good agreement between the predicted linearized analysis and the LES provided the forcing frequency wasn't too high. When they coupled in an equation for turbulent kinetic energy (TKE) and used a w_*-type entrainment closure, they found good agreement even when the forcing frequency was high.

Bellon and Stevens (2012) analyze the timescales in response to a sudden perturbation in SST for a trade-wind cumulus-topped boundary layer (CuBL) using LES, a MLM, and a mixing-line model (XML). They linearize both the MLM and XML in order to derive the eigenvalues (and thereby the characteristic timescales), and find that the XML admits three timescales, including a fast timescale, that also agrees well with LES. The MLM, however, using a particularly simple entrainment closure,[1] shows no scale separation between the two fastest scales. The authors conclude from the XLM that the three scales correspond to the adjustment of sub-cloud buoyancy, the thermodynamic adjustment, and boundary-layer deepening.

The goal of this chapter is to address the transient response of a STBL to large scale forcing using both an MLM and an LES. In particular, I wish to understand on what timescales the cloud base, cloud top, and liquid static energy adjust as they approach steady state. Special emphasis is placed on the fast timescale, which is the least discussed

[1]The closure used, which is not suitable the STBL, is $w_e = k\langle w's'_v\rangle_0/\Delta^i s_v$, where the subscript "0" denotes the surface.

in the literature.

The MLM and SAMA LES models are both described in Chapter 2. In Sec. 5.2 I present the linearization approach that is used to extract and interpret the timescales in the MLM. Sec. 5.3 applies this linearization in the MLM for the DYCOMSII–RF01 case study, and I show that the fast scale exists as a result of an entrainment–LWP feedback. A comparison is made with LES to show that the fast scale operates similarly in the LES as well. Sec. 5.5 shows that the fast scale again is in effect when the CGILS S12 case is subjected to a sudden increase in temperature, but that it does not feature prominently when CO_2 is increased. The findings are summarized in Sec. 5.7.

5.2 Linearization of the MLM

Consider a generic system of ordinary differential equations given by:

$$\dot{\boldsymbol{x}} = \boldsymbol{f}(\boldsymbol{x}; \boldsymbol{\alpha}), \tag{5.3}$$

where $\boldsymbol{x} = (x_1, x_2, \ldots, x_n)$ are the n prognostic variables, $\boldsymbol{\alpha} = (\alpha_1, \alpha_2, \ldots, \alpha_m)$ are m parameters, t is the independent variable, $\dot{\boldsymbol{x}} = \frac{\partial \boldsymbol{x}}{\partial t}$, and $\boldsymbol{f}$ is the specified "right hand side" function governing the evolution of $\boldsymbol{x}$. The internal adjustment timescales on which this system adjusts to a perturbation in either the forcing or the mean state are determined by linearizing this system of equations. Details of the process can be found in any elementary ordinary differential equations (ODEs) or dynamical systems text (e.g. Boyce and DiPrima, 2008; Strogatz, 2001), but can be readily summarized as follows.

Starting with a trajectory given by $\boldsymbol{x_1}(t)$ passing through an arbitrary point $\boldsymbol{x}_0$ at $t = 0$, consider a small perturbation applied at $t = 0$ either to the forcing parameters ($\boldsymbol{\delta\alpha}$) or to the trajectory ($\boldsymbol{x_2}(t) = \boldsymbol{x_1(t)} + \boldsymbol{\delta x}(t)$). Linearizing (5.3) about ($\boldsymbol{x_0}$,$t = 0$) yields:

$$\frac{d}{dt}\boldsymbol{\delta x}(t) \approx \boldsymbol{J}(\boldsymbol{x_0}; \boldsymbol{\alpha})\boldsymbol{\delta x} + \boldsymbol{\delta F}, \tag{5.4}$$

where $\boldsymbol{J}$ is the Jacobian matrix whose i^{th} row and j^{th} column is given by

$$J_{ij} = \frac{\partial f_i}{\partial x_j}, \tag{5.5}$$

evaluated at $\boldsymbol{x_0}$, and

$$\boldsymbol{\delta F} = \sum_k \frac{\partial \boldsymbol{f}}{\partial \alpha_k} \delta\alpha_k \tag{5.6}$$

is the perturbation to the forcing. Eq. (5.4) is the linearized approximation governing the evolution of $\boldsymbol{\delta x}(t)$. The solution can be written in matrix form as

$$\boldsymbol{\delta x}(t) = e^{\boldsymbol{J}t}\boldsymbol{\delta x_0} + \left(e^{\boldsymbol{J}t} - \boldsymbol{I}\right)\boldsymbol{J}^{-1}\boldsymbol{\delta F}, \tag{5.7}$$

where $\boldsymbol{I}$ is the identity matrix. Provided $\boldsymbol{J}$ is diagonalizable, it can be decomposed as

$$\boldsymbol{J} = \boldsymbol{V}^{-1}\boldsymbol{\Lambda}\boldsymbol{V}, \tag{5.8}$$

where $\boldsymbol{\Lambda}$ is the diagonal matrix of eigenvalues (i.e., $\Lambda_{ii} = \lambda_i$) and $\boldsymbol{V}$ is the matrix with the corresponding eigenvector $\boldsymbol{v}_i$ in the ith column. For the linear system (5.4), the eigenvalues and eigenvectors of $\boldsymbol{J}$ determine the solution. This can be seen clearly by using the diagonalization (5.8) in (5.7) to express the solution in terms of the eigenvalues and eigenvectors:

$$\boldsymbol{\delta x}(t) = \sum_j \left((a_j + b_j)e^{\lambda_j t} - b_j\right)\boldsymbol{v}_j \tag{5.9}$$

for constants a_j, b_j satisfying

$$a_j = \sum_k V^{-1}_{jk}\delta x_{0,k}, \qquad\qquad b_j = \frac{1}{\lambda_j}\sum_k V^{-1}_{jk}\delta F_k.$$

In this analysis I apply the above formalism in two different ways. In the first case, I treat $\boldsymbol{x_1}(t) = \boldsymbol{x^*}$ to be a fixed point of the system satisfying $\boldsymbol{0} = \boldsymbol{f}(\boldsymbol{x^*};\boldsymbol{\alpha})$, with $\boldsymbol{\delta F} = \boldsymbol{0}$ and $\boldsymbol{\delta x}(0) \neq 0$. The eigenvalues of $\boldsymbol{J}$ then determine the linear stability of the fixed point to perturbations in the state variables $\boldsymbol{x}$. If the real component of all eigenvalues is negative, then small perturbations about $\boldsymbol{x^*}$ decay in time and the fixed point is considered

asymptotically stable. The time scale τ_j for the decay of eigenvector $\boldsymbol{v_j}$ is then given by

$$\tau_j = -\frac{1}{\Re[\lambda_j]}. \tag{5.10}$$

Thus, we need only know the steady state (which can be obtained by evolving the model to equilibrium or an appropriate nonlinear solving routine) and the specified form of $\boldsymbol{f}$ to extract the timescales on which a perturbation will decay to the steady state. This approach is the prototypical way to analyze fixed point stability, and is the approach used to initially derive the timescales. However, such an approach is not well-suited to making direct comparison with LES. The more natural approach for comparison with LES is to consider a trajectory that is subject to a perturbation in the forcing at $t = 0$, for which $\boldsymbol{\delta F} \neq 0$ and $\boldsymbol{\delta x_0} = \mathbf{0}$. In this case, the timescales indicate how rapidly two trajectories diverge from one another when subjected to a change in forcing. If the real part of each eigenvalue is negative, then the time scales of (5.10) indicate how quickly $\boldsymbol{\delta x} \to -\boldsymbol{J}^{-1}\boldsymbol{\delta F}$.

The MLM, written terms of z_i, h, and q_t, is governed by the following system of equations[2]:

$$\dot{z_i} = w_e + \overline{w_s(z_i)} \tag{5.11a}$$

$$\dot{h} = \frac{1}{z_i}\underbrace{\left(w_e\Delta^i h + C_T V \Delta^s h - \Delta F_R^{BL}/\rho_0 - z_i \boldsymbol{v}\cdot\nabla_H h\right)}_{f_h} \tag{5.11b}$$

$$\dot{q_t} = \frac{1}{z_i}\underbrace{\left(w_e\Delta^i q_t + C_T V \Delta^s q_t + F_P(0) - z_i \boldsymbol{v}\cdot\nabla_H q_t\right)}_{f_q} \tag{5.11c}$$

For the MLM defined by (5.11), the Jacobian is given by

$$\boldsymbol{J} = \boldsymbol{J}_0 + \boldsymbol{J}_\mathrm{e} + \boldsymbol{J}_\mathrm{R} + \boldsymbol{J}_\mathrm{P}, \tag{5.12}$$

[2]See Chapter 2.1 for further discussion of the MLM and the notation.

where

$$\boldsymbol{J}_0 = \begin{bmatrix} \frac{d\overline{w_s}}{dz_i} & 0 & 0 \\ \frac{w_e}{z_i}\frac{dh^+}{dz_i} - \boldsymbol{v}\cdot\nabla_H h - \frac{f_h}{z_i} & \frac{-(w_e+C_T V)}{z_i} & 0 \\ \frac{w_e}{z_i}\frac{dq_t^+}{dz_i} - \boldsymbol{v}\cdot\nabla_H q_t - \frac{f_q}{z_i} & 0 & \frac{-(w_e+C_T V)}{z_i} \end{bmatrix}, \tag{5.13a}$$

$$\boldsymbol{J}_{\mathrm{e}} = \boldsymbol{u}_{\mathrm{e}}\hat{\nabla} w_e, \qquad \boldsymbol{u}_{\mathrm{e}} = \begin{bmatrix} 1 \\ \Delta h/z_i \\ \Delta q_t/z_i \end{bmatrix}, \tag{5.13b}$$

$$\boldsymbol{J}_{\mathrm{R}} = \boldsymbol{u}_{\mathrm{R}}\hat{\nabla}\left(\Delta^{BL} F_R/\rho_0\right), \qquad \boldsymbol{u}_{\mathrm{R}} = \begin{bmatrix} 0 \\ -1/z_i \\ 0 \end{bmatrix}, \tag{5.13c}$$

$$\boldsymbol{J}_{\mathrm{P}} = \boldsymbol{u}_{\mathrm{P}}\hat{\nabla} F_P(0), \qquad \boldsymbol{u}_{\mathrm{P}} = \begin{bmatrix} 0 \\ 0 \\ 1/z_i \end{bmatrix}. \tag{5.13d}$$

Here the $\hat{\nabla}$ operator is defined as the row vector representation of the gradient with respect to the model variables–i.e.,

$$\hat{\nabla} F \equiv \left[\ \frac{\partial F}{\partial z_i}, \frac{\partial F}{\partial h}, \frac{\partial F}{\partial q_t}\ \right]. \tag{5.14}$$

$\boldsymbol{J}_0$ represents the "essential" timescales assuming there are no additional entrainment, radiative, or precipitation feedbacks. $\boldsymbol{J}_R$ is the contribution from radiative feedbacks, $\boldsymbol{J}_P$ the contribution from precipitation feedbacks, and $\boldsymbol{J}_e$ the contribution from entrainment feedbacks. The traditional τ_i and τ_{th} timescales come from $\boldsymbol{J}_0$. As a lower triangular matrix, the eigenvalues appear on the diagonal. For a fast timescale to arise requires a contribution from one of the feedbacks.

In general, the linear expansion of $\boldsymbol{J}$ in (5.12) is not useful for determining its eigenstructure. However, it is convenient here for two reasons. First, this expansion allows us to isolate individual feedback components. Second, in the case that only one of the forcings is present (e.g., when considering radiative flux divergence concentrated at the cloud top and no precipitation), then the lower triangular nature of $\boldsymbol{J}_0$, combined with the outer product

nature of each of the individual forcings, does provide some additional insight, as discussed in Sec. 5.3.

5.3 MLM DYCOMSII–RF01 timescale analysis

The DYCOMSII–RF01 case study, based on Stevens et al. (2003) and further described in Zhu et al. (2005), provides an excellent framework for the analysis of the internal timescales of a well-mixed STBL. The idealized case specification utilizes a simplified analytic representation of the radiative flux vertical profile for a nocturnal stratocumulus, and the case is essentially non-precipitating[3].

The DYCOMSII–RF01 case here is implemented in both the MLM and SAMA LES as in Uchida et al. (2010), and is described only briefly here. The subsidence is specified in terms of the large scale divergence, $\overline{w_s(z_i)} = -Dz_i$, with $D = 3.75 \times 10^{-6}$ s^{-1}. As a Lagrangian study, there is no horizontal advection tendency in q_t or h. The free troposphere profile of h increases with a constant lapse rate of $dh^+(z_i)/dz_i = 6$ kJ kg^{-1}, while $q_t^+ = 1.5$ g kg^{-1} is constant in the free troposphere. Fixed droplet concentration of $N_d = 150$ cm^{-3} is used throughout.

As in Uchida et al. (2010), idealized LW radiative cooling is implemented as

$$F_R(z) = F_0 e^{-Q(z,\infty)} + F_1 e^{-Q(0,z)}, \tag{5.15}$$

where

$$Q(a,b) = \kappa \int_a^b \rho q_\ell dz, \tag{5.16}$$

ρ is the density of dry air, $\kappa = 85$ m^2 kg^{-1}, $F_0 = 70$ W m^{-2}, and $F_1 = 22$ W m^{-2}. Equation (5.15) is the same expression that appears in Zhu et al. (2005), except it neglects the term accounting for additional radiative cooling above the boundary layer. For the LES, a minimum boundary-layer averaged cooling rate of 2 K day^{-1} is enforced to compensate

[3]Precipitation was identified as one of the factors that can violate the slow-manifold approximation of Bretherton et al. (2010). It is reasonable to assume that substantial precipitation could also wreak havoc on the fast timescale.

for the lack of radiative cooling in clear air columns in (5.15).

The MLM is used to evolve (5.11) from the initial condition $z_i(0) = 840$ m, $z_b(0) = 610$ m, and $q_t(0) = 9$ g kg^{-1}. In this section, the MLM is used in three configurations. First, the default configuration, described in Chapter 2.1, which uses the TN-type entrainment closure with $a_2 = 60$ and includes an explicit entrainment-sedimentation feedback ($a_{\text{sed}} = 9$ following Bretherton et al., 2007). Precipitation is parameterized following Caldwell and Bretherton (2009). A minimal version of the MLM, denoted as "RP," follows the default configuration except that it includes no precipitation effects (i.e., $F_P(z) = 0$), and assumes that the radiative flux divergence is all concentrated at cloud top (i.e., $F_R(z) = 0$ for $z < z_i$, while ΔF_R^{BL} is held constant). The MLM is also run using a specified constant entrainment rate equal to the steady-state entrainment rate from the default configuration.

Time series of cloud top and cloud base are shown in Figure 5.1. Both the default and RP configurations evolve similarly, though the RP configuration exhibits a somewhat higher entrainment rate throughout the first several days. Using fixed entrainment, z_i evolves nearly identically to the RP configuration, but the evolution of the cloud base during the first few days differs markedly. In particular, both the RP and default configuration exhibit an initial rapid increase in z_b that reduces substantially within the first day, whereas the cloud base rises more steadily for fixed w_e.

To extract the timescales, the MLM is run for 10 days of simulation time to reach near-steady-state, and then an iterative nonlinear solving routine (MATLAB's `fsolve` function) is used to determine the steady state. The Jacobian matrix is evaluated at steady-state using a second order accurate finite difference approximation. The eigenvalues and associated timescales are given in Table 5.1.

The slowest timescale (τ_3) is consistent with the inversion deepening timescale $\tau_i = D^{-1}$ of (5.1) for all three configurations. Similarly, the intermediate timescale τ_2 is approximately given by τ_{th} in (5.2). Both the default and RP configurations also admit a fast timescale of approximately 7.5 h (τ_1). Thus, internal w_e–boundary layer response mechanisms are sufficient for introducing the fast scale. The fast timescale is eliminated by the constant w_e simulation (which maintains both the precipitation and radiative structure of the default configuration), showing that entrainment feedbacks are also a necessary condition to gen-

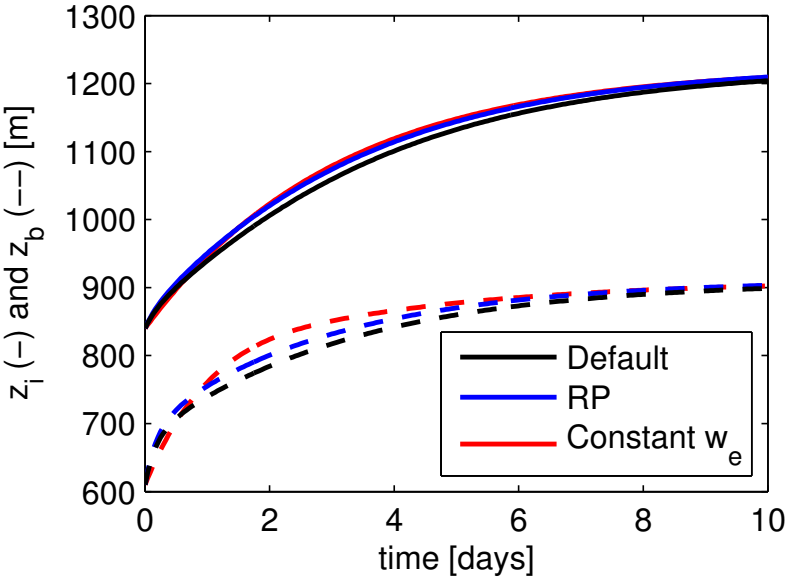

Figure 5.1: Time series of cloud top (z_i, solid) and cloud base (z_b, dashed) for MLM DYCOMSII–RF01 simulations. The default MLM configuration is shown in black. The RP configuration, in which the radiative flux divergence is concentrated at cloud top and precipitation is turned off, is shown in blue. The constant entrainment rate configuration, which is identical to the default configuration except constant w_e equal to the steady-state entrainment rate is used in place of the standard entrainment closure, is shown in red.

erate a fast timescale. The remainder of this section is devoted to further interpreting the nature of the fast entrainment-induced response.

5.3.1 Isolating the impact of entrainment in the 2D (thermodynamic) limit

Before considering the full MLM, it is useful to consider the limit where z_i is held fixed. Because z_i adjusts on a much slower timescale than the fast scale being sought here, such a simplification is reasonable[4]. This two-dimensional system also exhibits a fast scale associated with entrainment feedbacks.

The left panel of Figure 5.2 shows the evolution of the two dimensional system defined by

[4]This limit could also be obtained through formal asymptotic expansion techniques by replacing (5.11a) with $\dot{z_i} = \varepsilon(w_e + \overline{w_s(z_i)})$ and expanding z_i as a power series in ε:

$$z_i(t) = z_{i,0} + \varepsilon z_{i,1}(t) + \varepsilon^2 z_{i,2}(t) + \dots$$

To zeroth order, $z_i(t) = z_{i,0}(t) + \mathcal{O}(\varepsilon)$ is constant.

Table 5.1: Eigenvalues (timescales) from MLM DYCOMSII–RF01 steady-state.

Run	λ_1 (τ_1)	λ_2 (τ_2)	λ_3 (τ_3)
Default	-37.4 (7.4 h)	-9.76 (28.5 h)	-3.61 (77 h)
RP	-36.9 (7.5 h)	-9.74 (28.5 h)	-3.87 (72 h)
Constant w_e	-10.3 (26.9 h)	-9.78 (28.4 h)	-3.75 (74 h)

Eigenvalues (in 10^{-6} s^{-1}) from the MLM steady-state for the DYCOMSII–RF01 case. The timescale in hours is shown in parentheses.

(5.11b)–(5.11c) with $z_i = 840$ m held fixed. Contours of the entrainment rate are shown in color, hourly snapshots of the position in phase space for a sample trajectory are shown by circles. Instead of using h and q_t for the thermodynamic variables, I have transformed to a coordinate system defined by the cloud base z_b and the air-sea virtual temperature difference $\Delta T_{v0} = (s_{vl} - s_{vl,0})/c_p$ as in Bretherton et al. (2010). The eigenvectors of the steady-state Jacobian matrix are also shown, along with the vector field denoting the direction of the "entrainment" eigenvector $\boldsymbol{v}'_1$ of $\boldsymbol{J}'_e$, defined below. Trajectories are shown for the default (full entrainment, radiation, and precipitation parametrizations, shown in blue) and the RP configuration (shown in red). As in the previous section, the evolution is qualitatively similar between the two model configurations, though the steady state differs somewhat.

From the w_e contours in Figure 5.2, we see that w_e varies most strongly with z_b. This is due to the TN entrainment closure that scales w_e proportional to the integrated buoyancy flux,

$$w_e = \frac{A w_*^3}{z_i \Delta b} \tag{5.17}$$

Since there is a large jump in buoyancy flux at cloud base, a change in z_b can have a large impact on w_*^3. On physical grounds, a thicker cloud generates more vigorous turbulence and drives higher entrainment. Higher entrainment, in turn, dries and warms the boundary layer, causing the cloud base to rise, decreasing the LWP and eventually halting further entrainment increases. Figure 5.2 confirms that during the first several hours there is

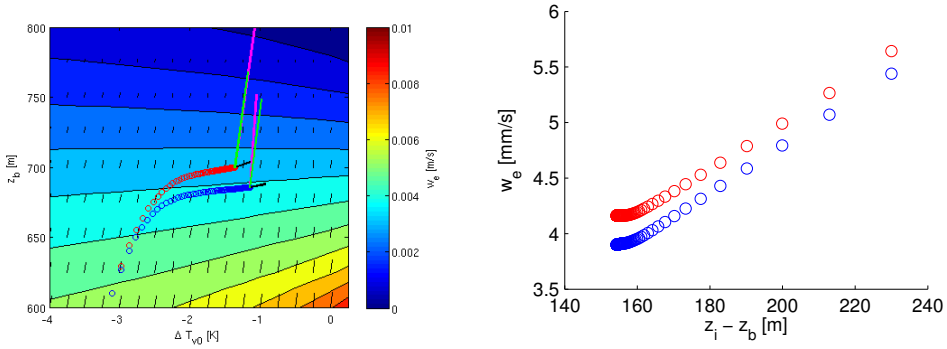

Figure 5.2: Evolution of the 2D MLM. *Left panel:* Contours of entrainment rate as a function of z_b and ΔT_{v0} for $z_i = 840$ m. Short black lines indicate the contribution to $(\dot{z}_b, \Delta\dot{T}_{v0})$ from entrainment. Hourly snapshots from two sample trajectories are shown by circles. The trajectory shown in red is for the RP configuration. The blue trajectory includes both precipitation and DYCOMSII–RF01 idealized radiation profile. Eigenvectors of the Jacobian evaluated at the (approximate) steady state are shown by the magenta (fast) and black (slow) vectors. The green vector indicates the direction of $\boldsymbol{u}_e$, which is the eigenvector with no radiative or precipitation feedbacks. *Right panel:* Snapshots of the entrainment rate for each of the trajectories described above versus the cloud thickness $z_i - z_b$. During the initial (fast) evolution of the trajectory, the relationship is nearly linear.

substantial change in the cloud base that rapidly adjusts the entrainment rate along the "fast" direction. Once this eigenvector has decayed, the slower thermodynamic evolution that projects primarily in the ΔT_{v0} direction dominates the evolution. Analytically, we proceed by considering the Jacobian for the 2D RP configuration,

$$\boldsymbol{J}_{2D} = \underbrace{\begin{bmatrix} -(w_e + C_T V)/z_i & 0 \\ 0 & -(w_e + C_T V)/z_i \end{bmatrix}}_{\boldsymbol{J}'_0} + \underbrace{\begin{bmatrix} \Delta^i h/z_i \\ \Delta^i q_t/z_i \end{bmatrix} \begin{bmatrix} \frac{\partial w_e}{\partial h} & \frac{\partial w_e}{\partial q_t} \end{bmatrix}}_{\boldsymbol{J}'_e}. \tag{5.18}$$

Since $\boldsymbol{J}'_0$ is diagonal with repeated eigenvalue λ_{th}, any vector is an eigenvector of $\boldsymbol{J}'_0$. As an outer product, $\boldsymbol{J}'_e$ has eigenvalues and eigenvectors

$$\lambda'_1 = \lambda_e = \frac{1}{z_i}\left(\frac{\partial w_e}{\partial h}\Delta^i h + \frac{\partial w_e}{\partial q_t}\Delta^i q_t\right) \qquad \boldsymbol{v}'_1 = \begin{bmatrix} \Delta^i h/z_i \\ \Delta^i q_t/z_i \end{bmatrix} \tag{5.19}$$

$$\lambda'_2 = 0 \qquad \boldsymbol{v}'_2 = \begin{bmatrix} \frac{\partial w_e}{\partial q_t} \\ -\frac{\partial w_e}{\partial h} \end{bmatrix}. \tag{5.20}$$

These matrices share eigenvectors so the eigenvalues add:

$$\lambda_1 = \lambda_{\text{th}} + \lambda_e \tag{5.21a}$$

$$\lambda_2 = \lambda_{\text{th}}. \tag{5.21b}$$

The degree to which λ_1 corresponds to a "fast" timescale depends on how responsive w_e is to changes along the direction $\boldsymbol{v}_1'$. With the TN-type entrainment closure, this response is quite powerful, since perturbations away from the steady-state entrainment rate will tend to result in a thicker (or thinner) cloud that will increase (or decrease) the entrainment rate and push the cloud thickness back toward maintaining a local balance. Proceeding along direction $\boldsymbol{v}_1'$ with this closure rapidly adjusts the cloud thickness, and therefore w_e, while the surface buoyancy flux adjusts on the slower thermodynamic timescale associated with λ_2.

5.3.2 Entrainment response due to fast cloud base adjustment

The simplicity of (5.21), combined with the strong projection of the fast scale in the z_b-direction, suggests a relatively simple (albeit non-rigorous) argument that relates the fast timescale to the cloud base adjustment. The right panel of Figure 5.2 shows w_e vs $z_i - z_b$ for the trajectories plotted in the left panel of Figure 5.2. During the fast adjustment period, the entrainment rate scales linearly with $z_i - z_b$. Considering the entrainment closure (5.17), w_e can be written as

$$\begin{aligned} w_e &= \frac{2.5A}{z_i \Delta b} \left(\overline{\langle w'b' \rangle}_{SC} z_b + \overline{\langle w'b' \rangle}_{C} (z_i - z_b) \right) \\ &= \frac{2.5A}{\Delta b} \left(\overline{\langle w'b' \rangle}_{SC} + \left(-\overline{\langle w'b' \rangle}_{SC} + \overline{\langle w'b' \rangle}_{C} \right) \left(1 - \frac{z_b}{z_i} \right) \right), \end{aligned}$$

where $\overline{\langle w'b' \rangle}_{SC}$ denotes the average of $\langle w'b' \rangle$ across the subcloud layer, and $\overline{\langle w'b' \rangle}_{C}$ the average over the cloud layer. Bretherton and Wyant (1997) showed that the cloud base jump in buoyancy flux is proportional to the turbulent liquid water flux at the cloud base,

which in turn is proportional to the latent heat flux in a well-mixed STBL, yielding

$$w_e = \frac{2.5A}{\Delta b}\overline{\langle w'b'\rangle}_{SC}\left(1+\hat{\sigma}\overline{\langle w'q_\ell'\rangle}\right),$$

where $\hat{\sigma}$ is a temperature-dependent scaling factor (Bretherton and Wyant, 1997). For a sufficiently short period of time, provided that $A/\Delta b$ and $\overline{\langle w'b'\rangle}$ remain nearly constant,

$$w_e \approx w_{ec} = w_0 + c\left(1-\frac{z_b}{z_i}\right), \tag{5.22}$$

where w_0 and c are treated as constants. From the cloud base relationship[5]

$$z_b(h,q_t) = \frac{1}{H}\left((1+\gamma)\Delta^s q_t - \frac{\gamma}{L}\Delta^s h\right), \tag{5.23}$$

where $H = (dq_s/dz)_u$ is the rate of change of q_s along a dry adiabat and $\gamma = L/c_p\frac{\partial q_s}{\partial T}$, we can write (5.11) in terms of z_b and s_{vl} instead of h and q_t:

$$\dot{z}_b = \underbrace{-\frac{1}{z_i}(w_{ec}+C_T V + cz_b^+/z_i)}_{\lambda_b} z_b + F_B/z_i \tag{5.24a}$$

$$\dot{s}_{vl} = \underbrace{-\frac{1}{z_i}(w_{ec}+C_T V)}_{\lambda_s} s_{vl} + F_S/z_i, \tag{5.24b}$$

where all source and sink terms that are not directly proportional to the state variables are grouped together in F_B and F_S, and $z_b^+ = z_b(h^+, q_t^+)$. Eq. (5.24b) has a solution exhibiting exponential decay $s_{vl} = c_0\exp(-\int\lambda_s(z_b)dt)+c_1$, with the familiar thermodynamic timescale. (5.24a) admits a hyperbolic tangent solution for z_b, but for the purpose of showing that the entrainment response provides a faster response timescale, it suffices to note that $c>0 \Rightarrow \lambda_b > \lambda_{\text{th}}$. Thus, the cloud base, which is a function of the thermodynamic moisture and temperature variables, adjusts on a faster timescale than any other individ-

[5]Technically speaking, this is the cloud base using linearized thermodynamics, which is somewhat different than the calculation performed by the default MLM which solves $q_s(p_b,T_b) = q_t$ for z_b. However, using linearized thermodynamics produces similar results to the default MLM, so this motivating argument is in reasonable agreement with the more complicated expression for cloud base.

ual thermodynamic variable does because the entrainment closure is sensitive to the cloud thickness.

A least-squares linear fit over the first 12 hours of the 2D RP simulation provides an estimate of $c = 0.0149$ m s^{-1}. Inserting this into (5.24a) yields $\lambda_b = 8.5 \times 10^{-5}$ s^{-1}, corresponding to a timescale of 3.3 h, which is within about 10% of the fast scale $\lambda_1 = 7.8 \times 10^{-5}$ s^{-1}(3.5 h timescale) calculated using a finite difference technique. Using (5.22) and (5.23) in (5.21a) gives $\lambda_1 = 6.9 \times 10^{-5}$ s^{-1}($\tau_1 = 4.0$ h). Thus, even using the crude approximation of (5.22) is able to largely explain the origin of the fast scale in the 2D system.

The same essential reasoning translates to the full 3D MLM. Since nothing relied on the 2D assumption, provided $w_e \approx w_0 + c(1 - z_b/z_i)$ and z_i varies slowly relative to z_b, the expression derived in (5.24a) applies and a similar interpretation holds. Figure 5.3 plots an assortment of trajectories in the full MLM starting from randomly chosen initial conditions. Each of the trajectories approaches the asymptotically stable fixed point in a qualitatively similar way. Initially there is a nearly linear fast response of w_e to cloud thickness, which eventually collapses onto a curve corresponding to the *slow manifold* introduced by Bretherton et al. (2010).

5.3.3 3D MLM Eigensystem

Returning to the full MLM of (5.11) and applying the DYCOMSII–RF01 steady-state conditions to the "essential" Jacobian of (5.13a) yields

$$\boldsymbol{J}_0 = \begin{bmatrix} -D & 0 & 0 \\ D\frac{dh^+}{dz_i} & -\left(D + \frac{C_T V)}{z_i}\right) & 0 \\ 0 & 0 & -\left(D + \frac{C_T V)}{z_i}\right) \end{bmatrix}. \tag{5.25}$$

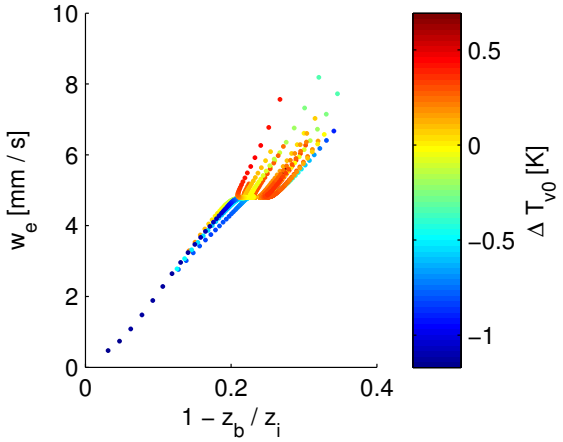

Figure 5.3: Entrainment rate of several trajectories for full 3D MLM simulations of DYCOMSII–RF01, plotted against $(z_i - z_b)/z_i$. Each trajectory originates from an initial condition that has been randomly perturbed away from the steady-state (shown as a black dot). Only simulations where the BIR remained less than 0.4 at all times were included. The relationship is approximately linear for perturbations away from the slow manifold. Colorbar shows ΔT_{v0}. Points are plotted once per hour of simulation.

In the case that there are no internal feedbacks (e.g., the RP case with fixed entrainment), the eigenvalues and eigenvectors are calculated from (5.25) to be

$$\lambda_1 = -D = \lambda_i \qquad \boldsymbol{v_1} = \begin{bmatrix} 1 \\ \frac{w_e}{C_T V}\frac{dh^+}{dz_i} \\ 0 \end{bmatrix} \tag{5.26a}$$

$$\lambda_2 = -D - C_T V/z_i = \lambda_{\text{th}} \qquad \boldsymbol{v_2} = \begin{bmatrix} 0 \\ 1 \\ 0 \end{bmatrix} \tag{5.26b}$$

$$\lambda_3 = \lambda_{\text{th}} \qquad \boldsymbol{v_3} = \begin{bmatrix} 0 \\ 0 \\ 1 \end{bmatrix}, \tag{5.26c}$$

where $\boldsymbol{v_{2,3}}$ could be any vectors that span the space defined by the thermodynamic variables (h, q_t). Here, the interpretation is clear–λ_1 is associated with inversion deepening, since its

eigenvector is the only one that projects in the z_i direction. The other two degenerate eigenvalues correspond to the adjustment timescale for the thermodynamic variables, which occurs on a shorter timescale than that of the inversion deepening. It should also be noted that $\boldsymbol{v_1}$ carries along a component in the δh direction, indicating that there is a slow component to the steady-state adjustment of the moist static energy due to the free troposphere lapse rate of h.

Consider the matrix $\boldsymbol{J_0}$ defined in (5.25) subject to a single outer-product type perturbation $\boldsymbol{J'}$, where

$$\boldsymbol{J'} = \boldsymbol{U}\boldsymbol{W}^T = \begin{bmatrix} u_1 \\ u_2 \\ u_3 \end{bmatrix} \begin{bmatrix} w_1 & w_2 & w_3 \end{bmatrix}. \tag{5.27}$$

Recall that $\boldsymbol{J'}$ has the same form as the perturbations (5.13b)–(5.13d). The eigenvalues of $\boldsymbol{J_0} + \boldsymbol{J'}$ are given by:

$$\lambda_1 = \frac{1}{2}\left(-2D - C_T V/z_i + \lambda' - \sqrt{\chi}\right) \tag{5.28a}$$

$$\lambda_2 = -D - C_T V/z_i \tag{5.28b}$$

$$\lambda_3 = \frac{1}{2}\left(-2D - C_T V/z_i + \lambda' + \sqrt{\chi}\right), \tag{5.28c}$$

where $\lambda' = \boldsymbol{W}^T\boldsymbol{U} = u_1 w_1 + u_2 w_2 + u_3 w_3$ is the non-zero eigenvalue of $\boldsymbol{J'}$ and

$$\chi = \left(\lambda' - \frac{C_T V}{z_i}\right)^2 + 4u_1\left(\frac{C_T V}{z_i} w_1 + D\frac{dh^+}{dz_i} w_2\right). \tag{5.29}$$

First, note that the thermodynamic adjustment scale is unaltered ($\lambda_3 = \lambda_{\text{th}}$). Mathematically, this is because there is a common eigenvector associated with both $\boldsymbol{J}_0$ (corresponding to λ_{th}) and $\boldsymbol{J'}$ (corresponding to a zero eigenvalue). Therefore, any *individual* outer product perturbation will preserve τ_{th}. Both the inversion deepening eigenvalue and the other thermodynamic eigenvalue are, in general, altered by the perturbation.

When the second term in (5.29) is small compared to the first, then these reduce to

$$\lambda_1 \approx \lambda_{\text{th}} + \lambda' \tag{5.30a}$$

$$\lambda_2 \approx \lambda_{\text{th}} \tag{5.30b}$$

$$\lambda_3 \approx \lambda_{\text{i}}. \tag{5.30c}$$

This is a good approximation when $\boldsymbol{J}' = \boldsymbol{J}_{\text{e}}$ with the MLM's default entrainment closure due to the strong dependence of the integrated buoyancy flux, and therefore w_e, on the cloud thickness.

When $u_1 = 0$ (e.g., the physical forcings of (5.13c) and (5.13d)), the second term in (5.29) is identically zero. In this case the relations in (5.30) become equalities rather than approximations, and the eigenvector associated with λ_1 is given exactly by $\boldsymbol{U}$. Thus if the *direct* radiation (or precipitation) feedback was dominant and there was no response due to entrainment, the eigenvector corresponding to λ_1 would project identically in the direction of the perturbation δh (or δq_t) and have no impact at all on the slow, inversion-deepening scale.

In summary, any individual perturbation that exhibits dependence on the boundary layer state will have some impact on the two timescales of $\boldsymbol{J}_0$ by splitting the degenerate thermodynamic eigenvalues, but only in the case where λ' has a large, negative real part do we expect the fast scale to arise. There is no general statement that can be made about the sum of 2 or more perturbations to $\boldsymbol{J}_0$ in terms of the eigenvalues of the individual matrices. Hence, this discussion applies primarily to the RP case.

The eigenvalues and eigenvectors for DYCOMSII–RF01 steady state are shown in Table 5.2, for the three cases presented in Table 5.1. The eigenvectors have been transformed to δz_i, δz_b, and $\delta \Delta T_{v0}$ coordinates and scales so that $|\delta z_b| = 1$ m. For the MLM in both default and RP configurations, the fast scale (corresponding to λ_1) is indeed associated with a large change in z_b relative to z_i and slight warming, as suggested by the 2D analysis. The intermediate, thermodynamic scale (corresponding to λ_2) projects almost entirely into the $(\delta z_b, \delta \Delta T_{v0})$ plane. The slow scale (λ_3) is associated with boundary layer deepening, cloud thickening, and entrainment-driven warming.

Table 5.2: Eigenvalues and eigenvectors from MLM DYCOMSII–RF01 steady-state.

Test	λ_1 [s^{-1}]	$\boldsymbol{v_1}$	λ_2 [s^{-1}]	$\boldsymbol{v_2}$	λ_3 [s^{-1}]	$\boldsymbol{v_3}$
Default	-3.74×10^{-5}	$\begin{bmatrix} 0.39 \\ 1 \\ 0.003 \end{bmatrix}$	-9.76×10^{-6}	$\begin{bmatrix} -5 \times 10^{-4} \\ 1 \\ 0.06 \end{bmatrix}$	-3.61×10^{-6}	$\begin{bmatrix} 1.94 \\ 1 \\ 0.007 \end{bmatrix}$
RP	-3.69×10^{-5}	$\begin{bmatrix} 0.39 \\ 1 \\ 0.003 \end{bmatrix}$	-9.74×10^{-6}	$\begin{bmatrix} 1 \times 10^{-4} \\ 1 \\ 0.06 \end{bmatrix}$	-3.87×10^{-6}	$\begin{bmatrix} 2.28 \\ 1 \\ 0.008 \end{bmatrix}$
Constant w_e	-9.92×10^{-6}	$\begin{bmatrix} 0 \\ 1 \\ 0.004 \end{bmatrix}$	-9.76×10^{-6}	$\begin{bmatrix} 0 \\ 1 \\ 0.07 \end{bmatrix}$	-3.75×10^{-6}	$\begin{bmatrix} 2.21 \\ 1 \\ 0.008 \end{bmatrix}$

Eigenvalues in inverse seconds. Eigenvectors in terms of $\begin{bmatrix} \delta z_i & \delta z_b & \delta \Delta T_{v0} \end{bmatrix}^T$ and normalized such that $|\delta z_b| = 1$ m and $\delta z_i \geq 0$. Default refers to the full MLM, RP to the MLM with cloud top cooling and no precipitation, and "Constant w_e" refers to the default configuration with fixed w_e.

On the fast scale the cloud thickness adjusts rapidly by changing the cloud base, such that the cloud thins if the boundary layer is deepening, and thickens if the boundary layer shallows. For the TN-type default closure of the model, this response is robust, owing to a large λ_e' dictating that the eigenvector is closely aligned with $\boldsymbol{u}_e$ defined in (5.13b).

On the intermediate scale the thermodynamic variables adjust without contributing to changes in the boundary layer depth. On the slow scale, the inversion changes more than the cloud base, such that a deepening boundary layer is associated with increasing LWP but very little change in entrainment. The thermodynamic variables respond in line with the increased entrainment warming caused by the larger inversion temperature jump for a deeper boundary layer. Whether the third scale is associated with increasing or decreasing LWP depends on the large scale forcing – see, e.g., Ackerman et al. (2004), van der Dussen et al. (2013), and Randall (1984).

By contrast, assuming fixed entrainment rate reproduces the more traditional separation into only the thermodynamic and the inversion deepening scales, with the thermodynamic eigenvectors projecting entirely into the thermodynamic plane.

5.3.4 MLM Perturbation Experiment: $\delta z_i = 50$ m

To illustrate these points, consider a perturbation to the DYCOMSII–RF01 default MLM steady-state of the form $z_i = z_i^* + \delta z_i$, where $\delta z_i = 50$ m, and the thermodynamic variables

are left untouched. Figure 5.4 shows the evolution of this system in the MLM with the TN entrainment closure. The top panel overlays contours of constant entrainment with the trajectory in the (z_b, z_i) phase plane. Each square represents the state at six hour intervals and the color indicates ΔT_{v0}. The three eigenvectors are shown as lines in the lower left of the plot (colors corresponding to those of the bottom panel), and the area of the circle corresponds to the magnitude of the projection of that eigenvector in the ΔT_{v0} direction. The bottom panels show the evolution of z_i (top left), z_b (top right), h (middle left), ΔT_{v0} (middle right), and q_t (bottom left) perturbations expanded into the basis defined by the eigenvectors of the steady state. The timescales associated with each eigenvector are given in the legend.

Because the perturbation increases the cloud thickness, the entrainment rate initially increases. Thus, δz_i projects into the fast direction as well as the slow direction, resulting in a small additional increase in z_i over the first 12 hours. However, the excessive warming and drying also raises the cloud base by nearly 20 meters over this time through adjustment of the fast scale, reducing the entrainment rate back nearly to its steady-state value within the first day. From this point, z_i and z_b evolve approximately along the slow manifold, while ΔT_{v0} decreases back to the equilibrium value on the intermediate timescale.

Whether or not each of the eigenvectors would tend to thicken or thin the cloud for a given increase in z_b is primarily due to whether the cloud top rises faster than the cloud base. Thus, any eigenvector with slope greater than 1 in the (z_b, z_i) plane will be associated with an increase in LWP, while any eigenvector with slope less than one is associated with decreasing LWP. Because the entrainment rate is quite sensitive to the LWP, the eigenvalue λ_e' of (5.13b) is quite large, and the resulting fast eigenvector projects strongly in the direction $\begin{bmatrix} \delta z_i & \delta h & \delta q_t \end{bmatrix} = \begin{bmatrix} 1 & \Delta^i h/z_i & \Delta^i q_t/z_i \end{bmatrix}$[6]. Assuming there are no significant radiative or precipitation feedbacks, the fast scale is thus associated with $\frac{dLWP}{dz_b} < 0$, regardless of the large scale conditions.

By contrast, under fixed entrainment (Figure 5.5), z_i projects entirely into the slow

[6]In principle, this assertion could be verified through a formal perturbation analysis, but that is complicated by the fact that the matrices are non-Hermitian, contain repeated eigenvalues, and do not necessarily have full rank.

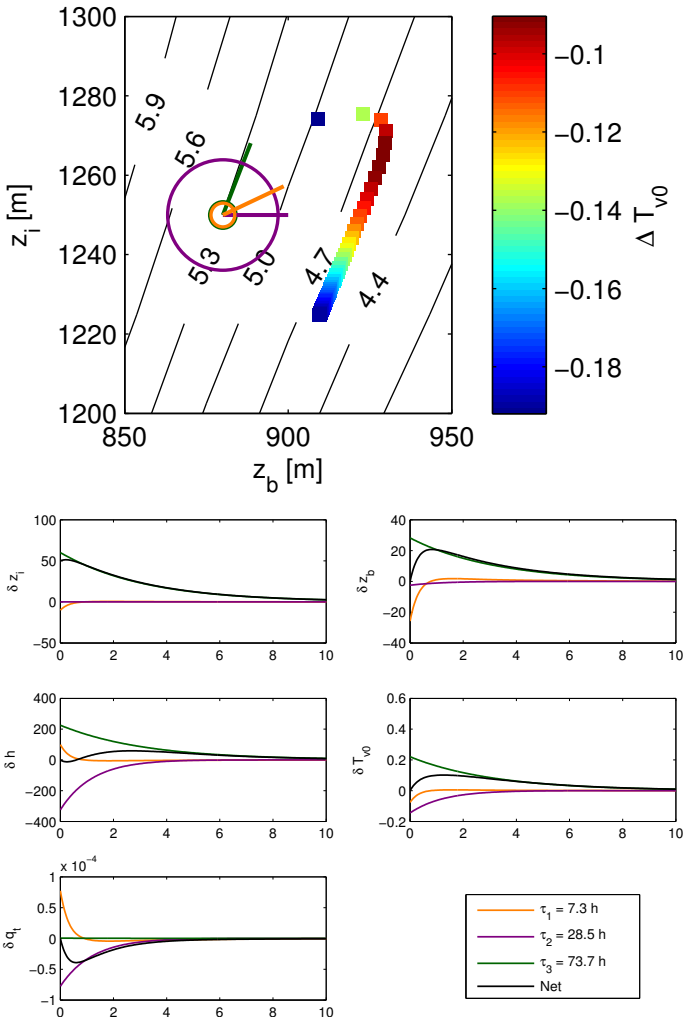

Figure 5.4: Phase space evolution of $\delta z_i = 50$ m perturbation about final steady state using default TN entrainment closure in MLM (top), and time series (bottom). Squares are state at every 6 hours. Lines correspond to eigenvectors.

direction, z_b and ΔT_{v0} changes are more more modest and adjust more slowly than in Figure 5.4 due to the lack of the fast scale. The thermodynamic variables project equally into the intermediate and slow directions initially since $\delta z_b(0) = 0$ and $\delta \Delta T_{v0}(0) = 0$. The evolution of the slow thermodynamic component is dictated by the inversion s_ℓ jump that increases with z_i and controls how much entrainment warming there is, while the intermediate component is driven by the surface fluxes.

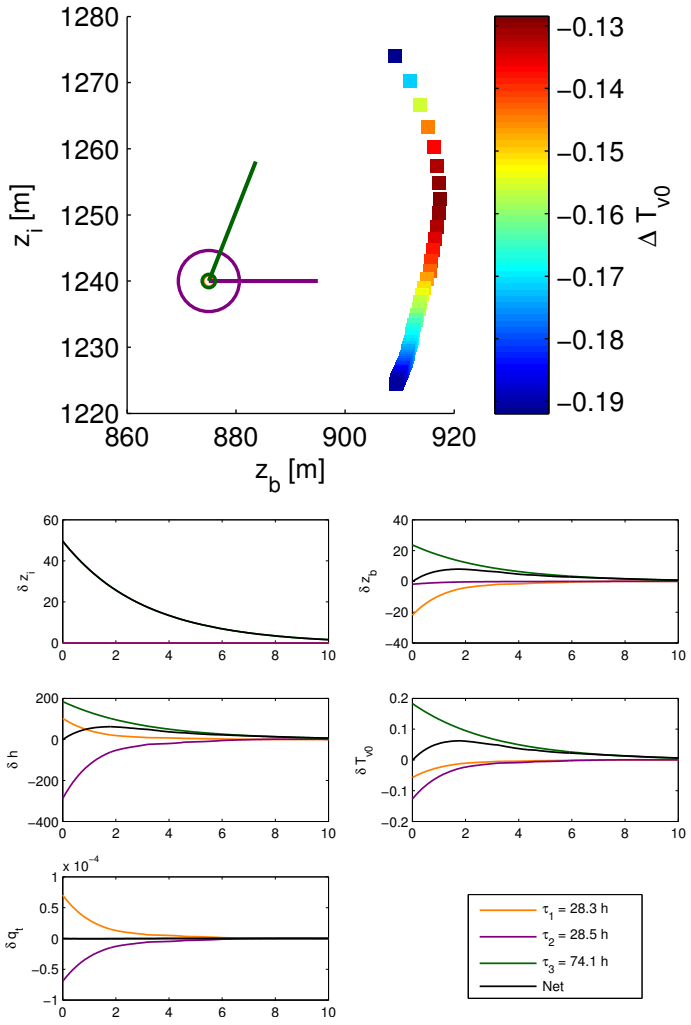

Figure 5.5: As in Figure 5.4, but with constant w_e.

5.3.5 Sensitivity to Entrainment Closure

The fast scale explored in the preceding section owes its existence to the entrainment response, and thus is dependent on the entrainment closure. Despite the importance of entrainment in the dynamics of the STBL, there is no consensus about the best way to represent it, and little experimental evidence that is suitable for constraining the entrainment parametrization approaches (Stevens, 2002).

In this section, we address the impact of the entrainment closure on the fast scale by

repeating the DYCOMSII–RF01 steady-state timescale analysis with a representative set of entrainment closures spanning a range of underlying assumptions. The default entrainment closure used in the MLM is based on that of Turton and Nicholls (1987), and hereafter denoted as the "TN" entrainment closure. The implementation of this closure is described more fully in Chapter 2.1, and also in Caldwell and Bretherton (2009), Uchida et al. (2010), and Bretherton et al. (2013). It explicitly includes the role of cloud droplet sedimentation in the entrainment efficiency following Bretherton et al. (2007). In addition to the default configuration, I also consider the case where there the sedimentation response is not included ($a_{\text{sed}} = 0$) in the entrainment efficiency, and also the case where the entrainment efficiency A is held constant.

The closure of Schubert et al. (1979a) is a flux-partitioning closure that fixes the subcloud buoyancy flux at a particular point (in this case, just below the cloud base) to a fraction of the integrated buoyancy flux:

$$\langle w'b' \rangle (z_b^-) = -k \int_0^{z_i} \langle w'b' \rangle (z) dz, \tag{5.31}$$

where $k = 0.5$ is used.

The closure of Lewellen and Lewellen (1998) (hereafter LL) is another flux-partitioning closure which deduces the entrainment rate from the assumption that

$$\eta_{LL} = \frac{\int_0^{z_i} (\langle w'b' \rangle_{NE} - \langle w'b' \rangle) dz}{\int_0^{z_i} \langle w'b' \rangle_{NE} dz}, \tag{5.32}$$

is a fixed constant ($\eta_{LL} = 0.35$ is used in this analysis). Here $\langle w'b' \rangle_{NE}$ is the buoyancy flux that *would* be present assuming there was no entrainment.

The closure of Lock et al. (2000b) relates the entrainment rate to a combination of velocity scales that each represent sources of turbulence. The Lock closure for the DYCOMSII–RF01 case can be written as

$$w_e = A_1 \frac{V_{\text{sum}}^3 / z_i + g \tilde{\beta}_T \alpha_t \Delta F_R^{BL}}{\Delta b + c V_{\text{sum}}^2 / z_i} \tag{5.33}$$

where V_{sum} is a combination of V_{surf} (representing surface heating), V_{rad} (representing cloud-

top radiative cooling) and $V_{\rm br}$ (representing buoyancy reversal). Full details, including parameter values, can be found in Lock et al. (2000b).

Several previous MLM studies that considered sensitivity to entrainment closure found that the nature of the entrainment closure being used does not significantly impact the steady-state solution (Caldwell and Bretherton, 2009; Bretherton and Wyant, 1997; Lewellen and Lewellen, 1998). This can be somewhat explained by the energy balance argument presented by Bretherton and Wyant (1997), which states that the entrainment rate must ultimately balance the diabatic flux divergence of s_{vl} across the cloud layer. Neglecting the subcloud component to the buoyancy flux leads to the minimal entrainment closure:

$$w_e^E = \frac{\Delta^{\rm cld} F_{R+P}/\rho_0 - (z_i - z_b)\frac{ds_{vl}}{dt}}{\Delta^i s_{vl}} \tag{5.34}$$

This closure was introduced as the minimal entrainment closure by Lilly (1968), and is equivalent to the Schubert closure with $k = 0$.

Table 5.3 shows the eigenvalues obtained from the steady-state of DYCOMSII–RF01 MLM simulations performed with each of these closures in the RP configuration. Since the emphasis is on the role of the entrainment closure, I present only the RP simulations to avoid any possible biases in the timescales due to precipitation or radiative feedbacks. Although I've shown previously that these effects are minor with the TN closure, since each of the entrainment closures settles into its own steady-state entrainment rate the role of precipitation and radiative feedbacks may differ across the simulations (e.g., a large LWP would enhance the precipitation feedbacks, whereas a very small LWP may decrease the overall radiative flux divergence in the default configuration).

Somewhat surprisingly, nearly all of the closures investigated include some form of fast timescale response. The only closure for which the fast timescale (and indeed, even the slow timescale) is not present is the energy balance closure. The reason for this is that each of these closures, with the exception of the energy balance closure, depends on an integral of the buoyancy flux. Since there is a substantial jump in buoyancy flux at the cloud base due to latent heating, each entrainment closure is sensitive to the cloud thickness, and thus also the level of the cloud base. Although the magnitude of this fast scale varies between

Table 5.3: Eigenvalues (in 1×10^{-6} s^{-1}) for a variety of entrainment closures discussed in Sec. 5.3.5. The timescale in hours is shown in parentheses.

Closure	λ_1	λ_2	λ_3
TN(full)	-36.1 (7.7 h)	-9.74 (28.5 h)	-3.70 (75 h)
TN($a_{sed} = 0$)	-36.9 (7.5 h)	-9.74 (28.5 h)	-3.87 (72 h)
TN(constant A)	-27.6 (10.1 h)	-9.84 (28.2 h)	-4.46 (62 h)
LL	-50.6 (5.5 h)	-10.31 (26.9 h)	-3.79 (73 h)
Lock	-31.7 (8.8 h)	-12.68 (21.9 h)	-4.47 (62 h)
Schubert ($k = 0.5$)	-28.9 (9.6 h)	-8.91 (31.2 h)	-4.73 (59 h)
Energy Balance	-9.6 (28.8 h)	-7.16 (38.8 h)	-5.77 (48 h)
Constant w_e	-9.74 (28.5 h)	-9.74 (28.5 h)	-3.75 (74 h)

closures, its existence does not.

In the LL, TN, and Schubert cases the fast timescale ranged from 5.5 h–10.1 h, exhibiting some scale separation from the intermediate scale (26.9–31.2 h). For the TN closure, the fast timescale was minimally impacted by the inclusion of the entrainment-sedimentation feedback of Bretherton et al. (2007), responding very slightly faster when $a_{\text{sed}} = 0$. Considering the effect of including sedimentation will slightly decrease the entrainment efficiency for a thicker cloud, thereby counteracting the tendency to increase entrainment with a thicker cloud, this is consistent with our interpretation of the fast timescale. By contrast, using fixed A results in a somewhat slower fast timescale, since it neglects the evaporative enhancement that further increases the entrainment efficiency for a cloud with greater liquid at the cloud top.

The inability of the energy balance closure to capture the fast scale present in the more sophisticated closures is consistent with our interpretation of the fast scale, since this closure does not depend explicitly on the integrated buoyancy flux.

5.4 Comparison with LES: Δq_t^+ perturbation in DYCOMSII–RF01

Constructing a perturbation that elicits a fast response in both LES and MLM is complicated by the need to ensure that the perturbation induces a discernible signal in the LWP. Furthermore, in order to compare with the MLM, any LES perturbation in the DYCOMSII–

RF01 framework must occur relatively early in the simulation because the LES evolves into a somewhat decoupled steady state (Stevens et al., 2005). Thus, rather than consider a perturbation about the steady state, we instead consider a perturbation to the boundary layer forcing early in the simulation and consider the rate at which two trajectories (one control trajectory, subject to the unperturbed forcings, and the other subject to the perturbation) evolve. In terms of (5.4), except δF is nonzero while $\boldsymbol{\delta x}(0) = \mathbf{0}$.

We implement a perturbation to the free troposphere humidity by adding a moist layer ($q_t = 2.25$ g kg^{-1}) in the free troposphere that then subsides into the boundary layer, thereby decreasing the inversion moisture jump. Since the DYCOMSII–RF01 idealized radiation scheme is independent of droplet size or free troposphere humidity, this has no direct radiative impact, but influences the cloud thickness through the amount of moisture that is entrained into the boundary layer.

Figure 5.6 shows the LES time-height evolution of q_ℓ in both the control case (CTL, left) and the perturbation case (Δq_t^+) where a moist layer ($q_t = 2.25$ g kg^{-1}) subsides in from the free troposphere, reaching the inversion after approximately six hours (right). The impact on liquid water path is seen immediately, with the Δq_t^+ simulation supporting more cloud liquid.

The fast response of the liquid water path is visualized by considering the difference in LWP between the Δq_t^+ and CTL runs shown in Figure 5.7. In both the LES (solid lines) and the MLM (dashed lines) the LWP increases rapidly once perturbation occurs. Though it is tempting to consider this rapid response alone as an expression of the fast timescale, the rapid divergence is due to additional moisture being entrained into the boundary layer in the perturbed case relative to the unperturbed case. Since the fast timescale is a result of the entrainment *adjustment* to LWP, the fast response here is better understood as the combination of the rapid increase in ΔLWP from 0.2–0.5 days, followed by the slower increase in LWP thereafter. That is, if the entrainment rate was held constant at the moment the perturbation is applied, the divergence in LWP would follow the initial evolution, and continue to increase nearly linearly. However, the larger LWP in the Δq_t^+ case increases the entrainment rate, which curtails the rapid increase in LWP.

The relation of this to the fast timescale in terms of the cloud base adjustment described

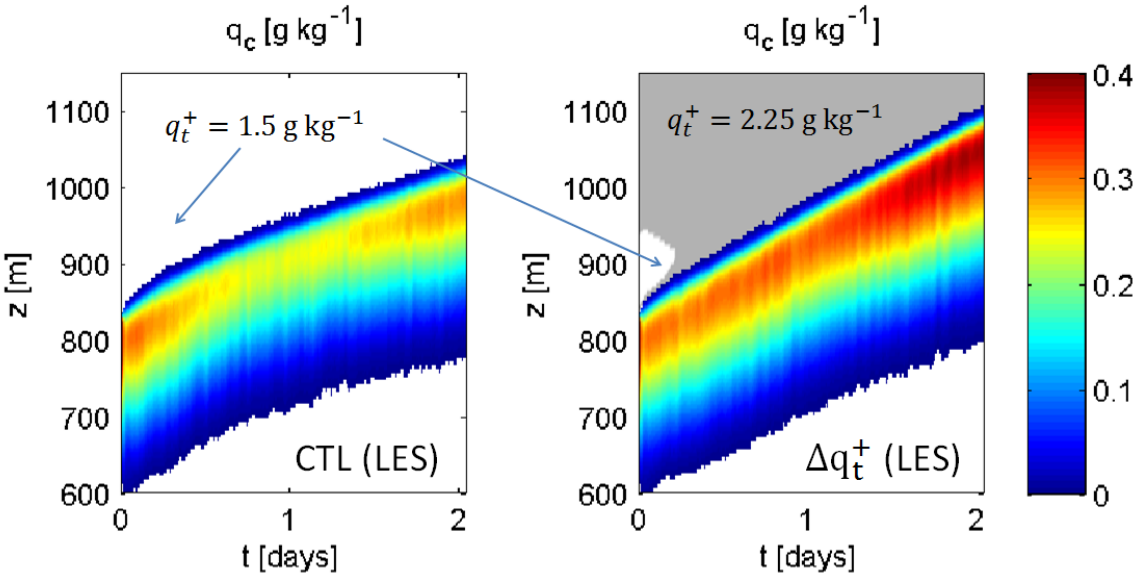

Figure 5.6: LES evolution of DYCOMSII–RF01 LWC for both CTL (left) and Δq_t^+ (right).

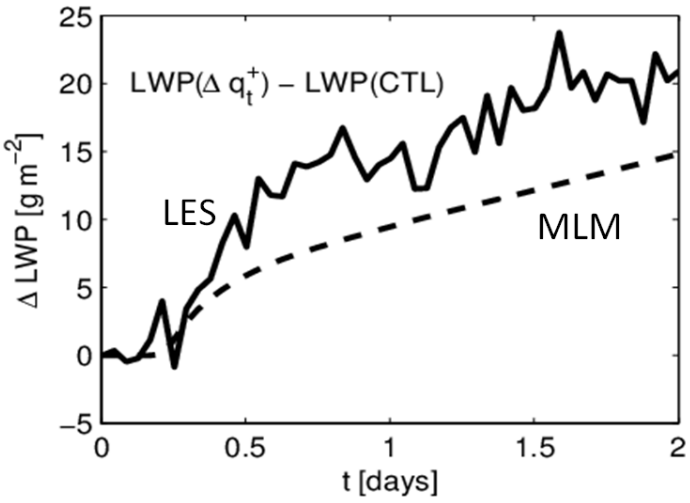

Figure 5.7: LES and MLM $\Delta LWP = LWP(\Delta q_t^+) - LWP(CTL)$, showing the fast timescale on which LWP diverges between the CTL and Δq_t^+ runs.

in Sec. 5.3.2 is seen more clearly in Figure 5.8, which plots the time series of the inversion top and cloud base for both MLM and LES CTL and Δq_t^+ simulations. In the LES, the inversion is calculated as the mean level where relative humidity decreases below 50%, and

the cloud base is identified as the level at which the mean cloud cover exceeds 50% of the maximum cloud cover. In both the MLM and LES, immediately after the perturbation the Δq_t^+ case shows a decrease in cloud base, thickening the cloud and resulting in a larger entrainment rate, as evidenced by the deepening of the inversion in the Δq_t^+ case relative to the MLM. The rapid cloud base adjustment is halted by this increase in entrainment rate, and the LWP proceeds to grow at a slower rate through the remainder of the simulations.

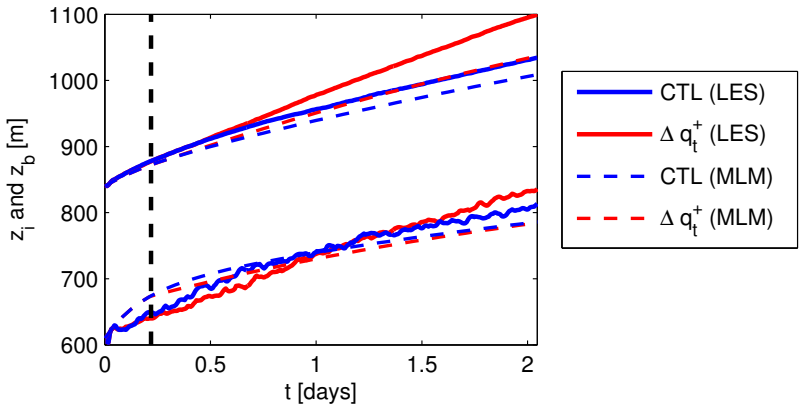

Figure 5.8: Evolution of capping inversion z_i and cloud base z_b in MLM and LES in CTL and Δq_t^+ DYCOMSII–RF01 runs. The dashed black line marks the approximate time at which the perturbation is applied.

5.4.1 Linearization applied to the MLM

The evolution of the linearized MLM CTL case (following (5.4)) subject to the Δq_t^+ perturbation

$$\boldsymbol{\delta F} = \left(\frac{\partial w_e}{\partial q_t^+} \begin{bmatrix} 1 \\ \Delta^i h / z_i \\ \Delta^i q_t / z_i \end{bmatrix} + \begin{bmatrix} 0 \\ 0 \\ w_e / z_i \end{bmatrix} \right) \delta q_t^+$$

is shown in Figure 5.9. The linearization (shown in black) does a remarkably good job reproducing the overall evolution of cloud top and cloud base (top panel), though it tends to over-entrain slightly (this becomes more noticeable after about one day). This provides

motivation to further expand the linearized system in terms of the eigenvectors of the Jacobian. In the bottom three panels of Figure 5.9, the inversion (top), cloud base (middle), and cloud thickness (bottom) perturbations are expanded into this basis. The inversion deepening projects strongly along the slow eigenvector, with a slight contribution from the fast scale that quickly saturates. The negative cloud base perturbation on the short scale is driven by the fast response (shown in orange), though its projection on the long scale governs the eventual cloud base rise. Until about 0.5 days, the increase in cloud thickness is due almost entirely to the fast scale response.

5.5 Fast scale response present in CGILS S12 climate-warming perturbation scenarios (LES and MLM)

In the previous section we analyzed a perturbation to the overlying humidity that elicited a fast entrainment-LWP response. One important motivation for this work is the relevance of this process for climate change sensitivity studies. We consider now three of the climate change sensitivity studies from the CGILS S12 case – the control (CTL) simulation, a +2K warming scenario (P2), and the control run with quadrupled CO_2 concentration (4xCO2). See Bretherton et al. (2013) and Chapter 4 for further discussion of the case setup. Each MLM and LES boundary layer is initialized with approximately the same cloud layer characteristics (i.e., similar z_i, z_b, and LWP).

In the full CGILS S12 MLM setup, the boundary layer evolution was coupled to a free troposphere whose temperature and moisture evolve in time to achieve radiative equilibrium. This was to facilitate better comparison with the LES. This primarily affects the temperature, moisture, and radiative cooling profile directly above the inversion, decreasing the effective inversion jump in s_ℓ and thereby stimulating greater entrainment. However, the cooling of the overlying air also brings along with it an associated timescale that leads to rapid adjustment during the first day of the MLM (and presumably the LES), one that is difficult to disentangle from the mechanism underlying the fast scales we seek here.

To better ascertain the degree to which the underlying fast response contributes to the P2 and 4xCO2 simulations, I also consider the following MLM configurations:

1. Constant w_e (CE): As in default, but with fixed entrainment rate equal to the steady-

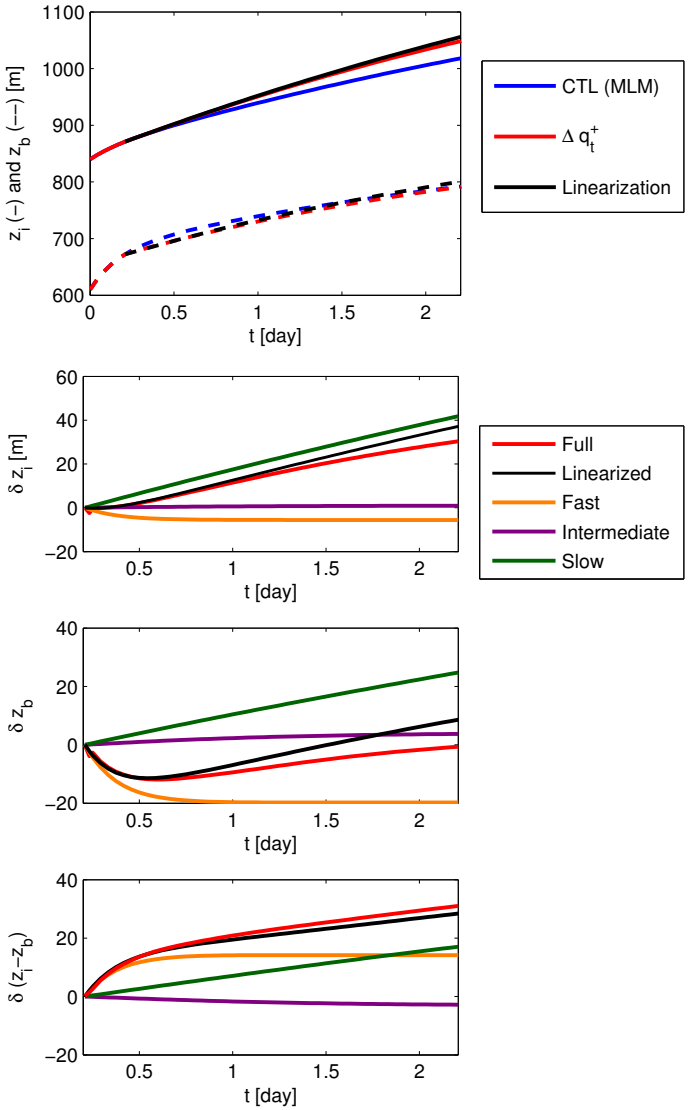

Figure 5.9: Top: Evolution of z_i and z_b for the MLM, showing linearization as well. Bottom: Projection of the eigenmodes associated with each timescale onto perturbations in z_i, z_b, and $z_i - z_b$, where $\delta z_x = z_x(\Delta q_t^+) - z_x(CTL)$.

state entrainment rate[7].

2. Fixed free troposphere (FT): The free troposphere moisture and temperature profiles are held fixed to the initial profiles specified by Blossey et al. (2013). In the case that z_i decreases, values are linearly extrapolated downward from the initial free troposphere profile. In spirit, this version is similar to the configuration used for DYCOMSII–RF01, except for the use of diurnally averaged radiation calculated using the RRTMG scheme in place of idealized nocturnal DYCOMSII–RF01 radiation.

3. FTM: As in fixed free troposphere, but with a uniform 2K temperature decrease in the free troposphere to better approximate the steady-state inversion temperature jump.

5.5.1 LES and default MLM

Figure 5.10 shows the time series for the first two days of the evolution of the LWP for the LES and default MLM. In both the MLM and LES there is a very rapid adjustment of LWP within the first few time steps of the model. However, this itself is not an indication of the fast scale. For that, we must consider the growth of a perturbation.

Figure 5.11 shows the difference in LWP between P2 and CTL, and between 4xCO2 and CTL. Consider first the LES (solid lines). There is a fast scale adjustment in the P2 ΔLWP relative to the CTL, evidenced by the 5 g m^{-2} decrease in LWP within the first half day before levelling off for the remainder of the time plotted. The LWP perturbation in 4xCO2, however, decreases nearly linearly throughout the first two days, and thus does not project onto the fast scale. This is consistent with previous analysis (not presented) of the DYCOMSII–RF01 case in which a perturbation to the radiative flux divergence (which is in essence the nature of the 4xCO2 perturbation) did not excite a fast scale response.

The default MLM (top left) reproduces the LES ΔLWP remarkably well over the first 0.5 days for the P2 perturbation, also clearly exhibiting the fast scale response. The 4xCO2

[7]Since we are interested in the early evolution of the simulation, one could argue that this is not the most appropriate entrainment rate to use. However, since the entrainment rate early in the simulation varies rapidly, no other choice is obviously better.

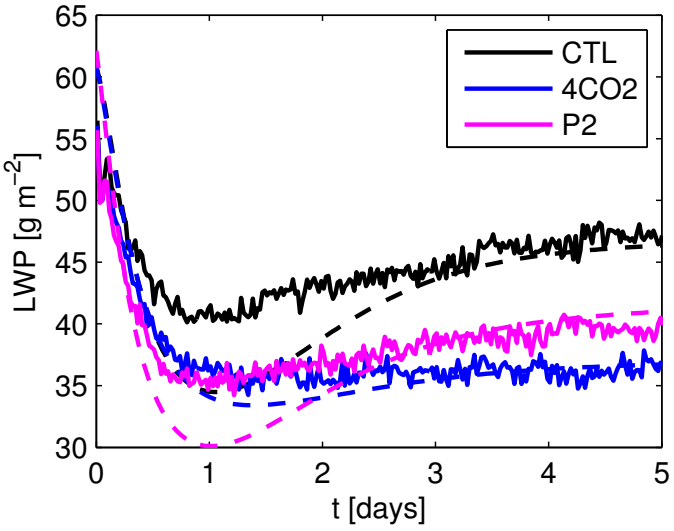

Figure 5.10: Time series of LWP for the CGILS S12 CTL, P2, and 4xCO2 cases, for both the LES (solid) and MLM (dashed).

LWP response is quite different, due primarily to the differing evolution of the free troposphere. At the very least, though, the MLM and LES agree that the 4xCO2 perturbation does not project onto the fast scale.

Thus, both LES and MLM again indicate the presence of a fast timescale, and indeed the bulk of the difference between P2 and CTL LWP that exists in the steady state developed over the first 12 hours. The analysis of the previous section indicated that the fast scale was due primarily to the entrainment-LWP adjustment. However, the top left panel of Figure 5.12 shows that the LES entrainment rate's relation to LWP during the fast adjustment period exhibits the *opposite* relationship from that which was analyzed in the MLM DYCOMSII–RF01 analysis of the previous section. Furthermore, the same qualitative relationship is also exhibited by the MLM (top right panel).

To assess the role the overlying free troposphere adjustment plays, we consider 3 additional configurations of the MLM. Figure 5.11 shows the evolution of ΔLWP in each of these configurations. First, consider the CE case (top right). Although the LWP still adjusts rapidly for each case during the first several hours, the fast scale associated with ΔLWP is not present – thus, variable entrainment rate in the boundary layer is still re-

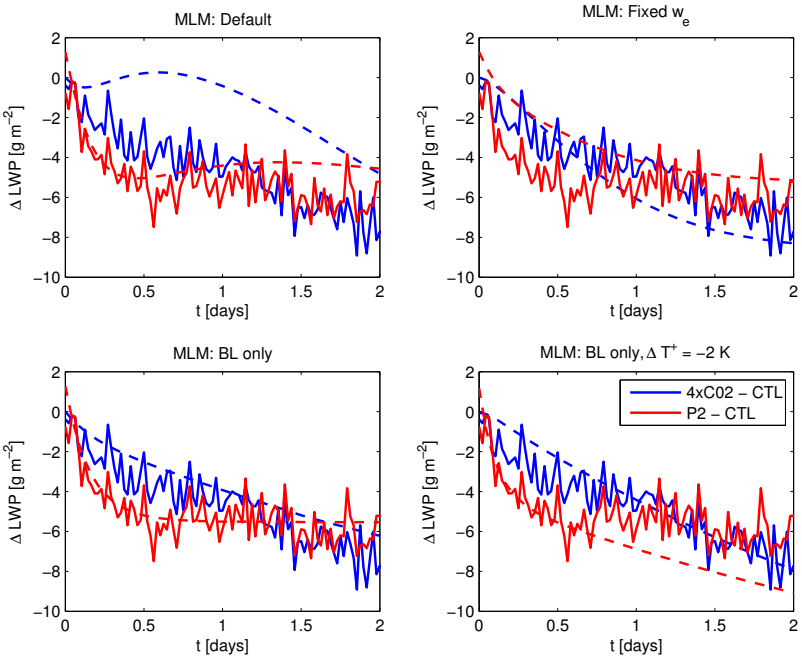

Figure 5.11: Difference in LWP between P2 and CTL, and between 4xCO2 and CTL, for both LES (solid lines) and MLM (dashed lines). Each panel corresponds to a different MLM configuration, indicated by the panel title.

quired for the expression of the fast scale. I hypothesize that the adjustment of the overlying atmosphere contributes to the rapid initial adjustment of LWP, since it is also present in the CE configuration.

Consider next the FT and FTM cases (bottom panels of Figure 5.11). The fast scale is again recovered, indicating that the FT entrainment response is sufficient for explaining the rapid adjustment of ΔLWP. In fact, comparison of this evolution with the LES shows that it is in better agreement than the default MLM is on the short scale. This may indicate that the MLM over-emphasizes the role of the free troposphere adjustment in the transient evolution of the boundary layer. Furthermore, the bottom panels of Figure 5.12 exhibit the classic linear response between LWP and cloud thickness within the fast regime. It is worth comparing again this trajectory in (LWP, w_e) phase space with that of the default MLM configuration (top right). The only difference between these two configurations is the evolution of the overlying temperature and moisture. Thus, we see that this process exerts

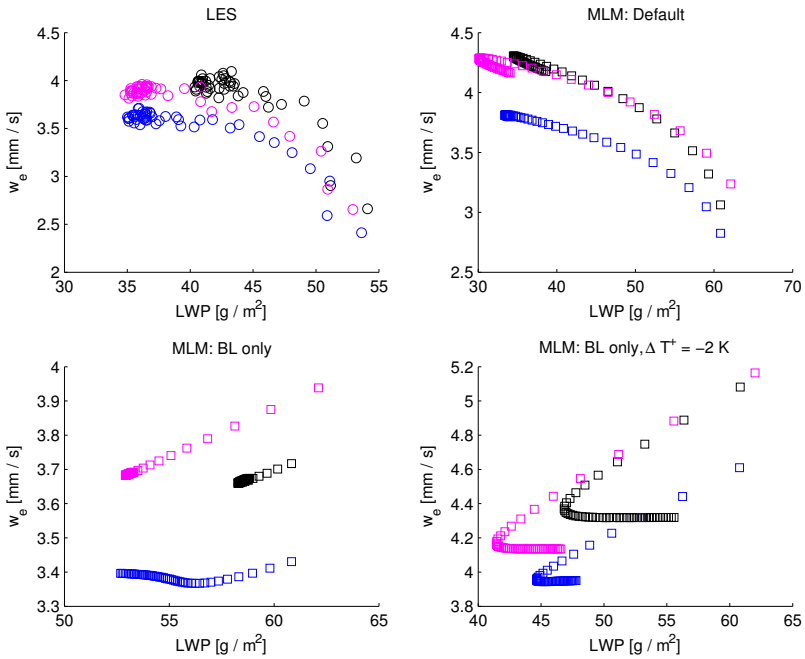

Figure 5.12: Scatter plots showing the hourly average entrainment rate vs. the LWP for CTL, P2, and 4xCO2 cases in the LES (top left), default MLM (top right), FT MLM (bottom left), and FTM MLM (bottom right).

substantial control over the w_e-LWP relationship.

5.5.2 Cloud-thinning response to P2 perturbation

Although the focus of this chapter has thus far been on the fast timescale, the entrainment-liquid flux mechanism responsible for the fast scale also has implications for the cloud thickness in a uniformly warmed climate. To show this, we use the MLM in FT (fixed troposphere) configuration to evolve the S12 CTL case to steady state, and then apply an instantaneous perturbation from CTL to P2, while also increasing the temperature of the boundary layer by 2K at fixed relative humidity. Fixed entrainment efficiency is used in order to focus on the response of entrainment to the integrated buoyancy flux. The time series of cloud base and boundary layer depth is shown in the left panel of Figure 5.13. Remarkably, the fast scale response explains the bulk of the steady-state P2 response, which has very slightly increased entrainment being supported by a thinner cloud.

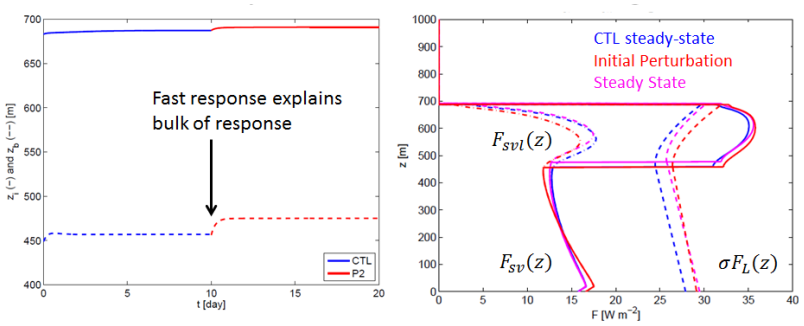

Figure 5.13: Left: Time series showing S12 MLM CTL simulation (blue) instantaneously perturbed to P2 (red) at $t = 10$ days, with the boundary layer warmed by 2K with fixed relative humidity at the point of perturbation. Right: Buoyancy flux profiles just before the perturbation (blue), just after the perturbation (red), and at the final steady state (magenta), scaled into units of W m^{-2}. Also shown are contributions from F_{sv}, F_{svl}, and σF_L.

The explanation for this can be gleaned from an examination of the right panel of Figure 5.13, which shows the buoyancy flux profile for the state just before the perturbation is applied, instantaneously after the perturbation, and at steady state. Also shown are $F_{sv} = \rho_0 \langle w' s'_v \rangle$, $F_{svl} = \rho_0 \langle w' s'_{v\ell} \rangle$, and $\sigma F_L = \sigma \rho_0 L \langle w' q'_t \rangle$, which represents the latent contribution to the buoyancy flux jump within the cloud. Due to the increased latent heat

flux in the warmed climate, the in-cloud buoyancy increases in the warmed climate. This generates a burst of entrainment that thins the cloud layer until balance is restored. Because of the larger in-cloud buoyancy flux, a similar entrainment rate is sustained by a thinner cloud in the warmer climate, representing a positive cloud-climate feedback mechanism. Thus, the mechanism behind the fast STBL timescale is also the mechanism that explains the positive feedback between CTL and P2 that was discussed in Chapter 4.5.4.

5.6 The diurnal cycle

I also performed an analysis of the diurnal cycle based on the CGILS S12 CTL case, and found that the short timescale is only a small part of the LWP response of the MLM for diurnal-cycle forcing. To simulate the diurnal cycle in a way that would be tractable for linearizing the MLM using (5.4), I separately fit the longwave (LW) and shortwave (SW) components of the steady-state diurnally averaged profile as

$$F_R(z) = F_{LW} + A_{SW} F_{SW} \tag{5.35}$$

$$F_{LW} = F_D(F_0 = 78, F_1 = 15.4, \kappa = 105) \tag{5.36}$$

$$F_{SW} = -(15e^{-39Q_c(z)} + (162 + 0.007z)), \qquad (z \leq z_i) \tag{5.37}$$

where F_D is the DYCOMSII–RF01 radiation parameterization, and $Q_c = \int_z^\infty \rho_w q_\ell dz'$. For the diurnally averaged case, $A_{SW,0} = 1$. The SW parametrization corresponds to the assumption that there is uniform absorption below the cloud, and exponentially decaying absorption within the cloud layer.

Using the idealized specification for radiation, the diurnal cycle was approximated by choosing $A_{SW}(t) = A_0 \cos Z(t)$, where $Z(t)$ is the solar zenith angle and A_0 was chosen to match the TOA insolation.

Because the entrainment rate responds directly to the radiative forcing through its im-

pact on the buoyancy flux, the linearization of (5.4) has the form

$$\boldsymbol{\delta F}(t) = \left(\frac{dw_e}{dA_{SW}} \boldsymbol{u}_\mathrm{e} - \begin{bmatrix} 0 \\ -\Delta^{BL} F_{SW}/\rho_0 \\ 0 \end{bmatrix} \right) (A_{SW}(t) - A_{SW,0}). \tag{5.38}$$

The derivative of w_e with respect to A_{SW} was estimated by explicitly separating the contribution of the radiative flux profile to the integrated buoyancy flux,

$$\begin{aligned} w_e &= \frac{\alpha I_0}{1 - \alpha I_1} \\ &= \frac{\alpha \left(I_{0,NR} + I_{0,LW} + A_{SW} I_{0,SW} \right)}{1 - \alpha I_1} \Longrightarrow \frac{dw_e}{dA_{SW}} \approx \frac{\alpha I_{0,SW}}{1 - \alpha I_1}, \end{aligned}$$

where I_j are the integrals defined in the appendix of Bretherton and Wyant (1997), and the subscript LW refers to the longwave contribution to I_0, SW the shortwave contribution, and NR the non-radiative contribution. This was found to somewhat over-estimate the response of w_e, so it was rescaled to better reproduce the range of w_e seen in the full S12 MLM diurnal simulations discussed in Chapter 4.

Inserting (5.38) into (5.4), we can integrate the system of first order, linear ODEs, and take the limit as $t \to \infty$ to extract the long-term, periodic solution $\boldsymbol{\delta x}(t)$. This approach allows one to determine the phase shift and amplitude of the resulting oscillations relative to the input forcing.

Counter to initial expectations, the diurnal cycle does not project strongly onto the fast scale. This is due to a combination of factors. First, the entrainment rate responds directly to changes in the radiative forcing, whereas the short timescale response is driven by feedbacks between the LWP and entrainment rate, which is dominated by the direct radiative response. Secondly, the slow and intermediate timescales are associated with eigenvalues that are much smaller than the frequency of the diurnal cycle, $\omega_D = 2\pi/\mathrm{day}$, whereas the fast timescale eigenvalue is comparable in magnitude to ω_D. As a result, the two slower scales exhibit a relatively small phase shift relative to the diurnal forcing, and add nearly constructively. The contribution from the fast scale has only a small impact on the

overall phase shift between input forcing and output signal. This impact is small enough that it is of comparable magnitude to the errors introduced by the use of the simplified radiation scheme used in the analysis. This is keeping in line with the lack of a short scale projection onto the radiative perturbation in the S12 4xCO2 case.

5.7 Conclusions

I have argued that the STBL admits a fast timescale that arises due to entrainment–LWP feedbacks. This was explained using a simple argument based on an evolution equation for cloud base, and further supported by a variety of MLM and LES simulations. In particular, the MLM was used to show that the fast scale was only presence when entrainment feedbacks are present; that the approximate timescale can be derived simply by considering the linear relation between w_e and $1 - z_b/z_i$ over the short timescale; and to investigate the response of the DYCOMSII–RF01 case to a perturbation about the steady-state. The role of the fast timescale was also investigated away from steady state, both in LES and MLM, by considering the difference between two trajectories from control and perturbation simulations for both the DYCOMSII–RF01 and CGILS S12 case studies. The fast scale contributes to the response of LWP to perturbations in the temperature of the surface and free troposphere, as well as to perturbations to the overlying humidity. Perturbations to the radiative driving were found not to project onto the fast timescale. This is true both when using idealized DYCOMSII–RF01 radiation and with the RRTMG radiation scheme used in many modern GCMs. In the case of the P2 perturbation to the CGILS S12 CTL case, the mechanism behind the fast timescale is shown to effectively explain the steady-state reduction of LWP in the warmed climate.

Although the entrainment-mediated response depends on the specific entrainment closure for the MLM, the vast majority of entrainment closures investigated exhibited this fast timescale. This is because most of the commonly used MLM closures, whether they are based on flux-partitioning or w_* forms, are anchored to the integrated buoyancy flux, which in turn is sensitive to the amount of cloud within the boundary layer due to the in-cloud buoyancy jump associated with the flux of liquid water. The exceptions to this are the so-called energy balance (or minimal) closures, based on steady-state energy balance

arguments for the boundary layer. Thus, even though the energy balance assumption is reasonable for identifying the steady-state entrainment rate, it does not capture the fast adjustment timescale. The use of such simplified closures will limit the ability of a model to exhibit a fast scale.

Within a linear system subject to time-varying forcings, the eigenvalues are relevant for determining the phase shift between the forcing and response of the system. I found that, in the case of the diurnal cycle, the signature of the fast timescale is difficult to detect due to the other adjustment timescales that are present. However, other time-varying forcings may project more strongly into the fast scale. This provides a possible indirect way to test whether a given entrainment closure is adequately capturing the adjustment timescales, by considering a time-varying forcing applied to, e.g., an LES. When considering such a test, it is important to choose a perturbation that will elicit a strong response on a short time frame, such as a perturbation to the overlying humidity.

Chapter 6

CONCLUSIONS

Stratocumulus clouds exert substantial influence on Earth's energy balance, but the range of spatial and temporal scales over which they interact with their surroundings presents a modelling challenge. This is particularly true for global climate models, whose large spacial domain and long time integrations require a grid where boundary layer clouds are hopelessly unresolved. Thus, the essential problem facing climate modellers is that boundary layer clouds are critical to understanding the Earth's response to increasing greenhouse gas concentrations, but the climate models themselves are forced to rely on parameterizations that must, by requirement, be both simple enough to capture the essence of aggregate boundary layer cloud behavior on a very coarse grid, yet sophisticated enough to accurately represent a wide range of physical processes. Parameterizations are, in turn, limited by a lack of definitive observations and process modeling identifying the important cloud-climate mechanisms driving climate change.

Low cloud-climate feedbacks represent the greatest source of disagreement amongst global climate models regarding climate sensitivity. To better represent them in climate models, we must better parameterize them so they can realistically respond to perturbations. This requires we understand the mechanisms currently operating in cloud parameterizations, better constrain these mechanisms through observations, and use this information to improve the parameterizations.

Within this context, the overarching goal of this work has been twofold – to better understand the processes that govern the radiative response of the stratocumulus-topped boundary layer to climate change-like perturbations within a hierarchy of models, and to better parameterize known processes.

In Chapter 3 we addressed an issue in which SCAM5 (the SCM associated with the CAM5 GCM) was exhibiting the exact *opposite* sensitivity of the LWP of a non-drizzling

stratocumulus to increasing N_d to that which was expected based on both LES and physical reasoning. For a non-drizzling stratocumulus, the suppression of cloud droplet sedimentation at cloud top with decreasing droplet size should increase the entrainment efficiency for higher N_d, thereby decreasing the cloud LWP. Accurately representing this feedback requires contributions from the cloud microphysics parameterization (which governs the cloud droplet sedimentation) and the PBL mixing scheme (which calculates the entrainment rate).

We found several factors that contribute to the response of non-drizzling stratocumulus LWP to N_d in SCAM5. The representation of q_ℓ internally within the PBL scheme in a way that was inconsistent with the representation of q_ℓ in the cloud microphysics was primarily responsible for the entrainment efficiency's insensitivity to cloud droplet concentration. We propose a simple modification in which q_ℓ is not diffused by the PBL scheme to fix this discrepancy, referred to as pseudo-conservative diffusion. This alone, however, is unable to reverse the incorrect sign of the LWP sensitivity to N_d in SCAM5, unless coupled with a shorter time step. Explicitly representing the entrainment-sedimentation feedback in (3.1) also helps. Global CAM5 simulations implementing pseudo-conservative diffusion in both pre-industrial and present-day simulations made very little impact in the overall change in SWCF, suggesting that, despite the clear improvement to the parameterization, it is not a dominant factor in CAM5's estimation of the AIE.

In Chapter 4, we systematically examined climate change sensitivities of subtropical stratocumulus-topped boundary layers using both an LES and MLM through a series of steadily forced simulations that perturbed forcings in various ways expected to accompany climate change. These perturbations included changes in temperature, CO_2 concentration, relative humidity, subsidence, inversion stability, and wind speed.

These models predict a reduction in shortwave cloud radiative effect (positive shortwave cloud feedback) for the CMIP3 $2\times CO_2$ forcing perturbations. The $2\times CO_2$ SWCRE reduction induced by the CMIP3 forcing changes is more than 10 W m^{-2} in the MLM, and somewhat larger in the LES. We partitioned the CMIP3 response into effects from individual forcing changes, which combine approximately linearly. The positive feedback from SWCRE reduction comes mostly from cloud thinning due to the overall warming of the profile induced by higher tropical SSTs, together with the direct radiative effect of increased CO_2.

Reduced subsidence due to weakening of tropical overturning circulations partly counteracts these two factors. Changes in wind speed, inversion stability, and free-tropospheric relative humidity have smaller, but non-negligible, impacts on the cloud thickness. The competition between reduced subsidence, which tends to lift the inversion in a warmer climate, and increased inversion stability and CO_2, which causes the inversion to shallow, is reflected in a slight predicted response in stratocumulus-top height.

Our analysis provides a firmer physical basis for climate model predictions that subtropical stratocumulus feedbacks on climate are positive. We further speculate that the large intermodel spread in the amplitude of subtropical low cloud feedbacks in global climate models is partially due to competing physical mechanisms, some of which decrease cloud thickness and fraction, and some of which increase them. Although the LES and supporting MLM arguments lend additional evidence for positive feedbacks, further observational tests of the physical mechanisms identified as being important should be undertaken. The physical mechanisms identified in this study as especially important for climate change are the roles of reduced radiative driving and more efficient turbulence production due to Clausius-Clapeyron-driven humidity flux increases in thinning clouds in a warmer climate.

In Chapter 5, we again turned to an MLM and LES to assess the characteristic timescales on which an STBL can be expected to respond to perturbations, and to understand the physical mechanism behind these timescales. We identified a heretofore unnoticed fast timescale of a few hours that is due entirely to entrainment-LWP feedbacks. Because most entrainment closures are tied to the integrated buoyancy flux in the STBL, and there is a large buoyancy jump within the cloud relative to below the cloud, entrainment and cloud base conspire together to rapidly reach an approximately local balance, after which time the entrainment rate and cloud base evolve more slowly. This was demonstrated in several cases to hold both in the MLM and LES, suggesting that this is a robust feature of the STBL.

One point of future interest is to better characterize what perturbations project onto the fast scale. Since boundary layer clouds are subject to forcings that occur with a wide variety of characteristic time scales, this knowledge will help interpret how quickly we can expect the LWP and entrainment rate to adjust to new conditions. We started down this

path by considering the degree to which perturbations to temperature or CO_2 projected onto the fast scale. In both MLM and LES we found that an increase in both the surface and free troposphere temperature simultaneously led to a rapid LWP response that reached its full extent over this fast scale (i.e., it projected very strongly onto the fast scale), whereas perturbing the radiative driving lead to a LWP difference that grew over a longer timescale.

Each of the analyses presented suggest avenues to explore moving forward. Our analysis of the AIE in SCAM5 showed that reducing the time step was necessary to uncover the correct sign of LWP sensitivity to N_d for non-drizzling stratocumulus. This suggests that it would be relevant to apply a time step sensitivity analysis to the global CAM5 simulations of pre-industrial versus present-day emissions coupled to the pseudo-conservative PBL diffusion of q_t. Such an analysis should shed light on the degree to which the parameterization of key aerosol-cloud interactions are hampered by the time-resolution. It would also be worthwhile to further analyze the global impact of our modifications to the cloud microphysics determination of the fall speed and droplet concentrations for rain. Although these modifications were originally implemented to remove a small amount of spurious surface precipitation, the changes made to the derived droplet distributions may have further-reaching implications.

In order to focus more directly on the AIE in CAM5, we envision that further single-column analysis would prove fruitful. Following our global runs, as well as those presented by Wang et al. (2011) (see Figures 9 and 14), the Northwest Pacific and South China Sea are two marine regions that represent a particularly large correlation between the change in LWP and the change in CCN between pre-industrial and present-day simulations. It would be informative to look at single column output from those regions to investigate which processes are important to the LWP response there. One interesting statistic to consider would be the fraction of precipitating clouds in these regions and their fractional contribution to the overall SWCRE.

The remarkable agreement between the MLM and LES in assessing the sensitivities to various forcings in the CGILS S12 case studies suggests that, at least in the well-mixed STBL regime, the LES response is well-interpreted using mixed-layer arguments. This is particularly encouraging because such arguments have the potential to provide a much

clearer understanding of the mechanisms governing the response of the STBL, which may help evaluate the response of other models. Given this success, I propose that we undertake a similar analysis with a subset of the SCMs included in the CGILS intercomparison. The variations in response of the SCM are substantially more varied than their LES counterparts. The degree to which an "SCM-tuned" MLM is able to reproduce the response of an individual SCM could illuminate the important underlying mechanisms behind the SCM-derived sensitivities. This approach is a natural extension of the work already undertaken in the MLM-LES comparison.

One of the limitations of the work presented here is its focus on the well-mixed boundary layer to the exclusion of stratified layers. In cases where the MLM is used, this is a requirement. However, insights derived from the MLM should be explored in decoupled boundary layers as well. For the CGILS S12 MLM analysis, an LES analysis supports the position that the mechanisms generally apply to the decoupled STBL represented by the S11 location because entrainment is the key process governing the boundary layer structure (Bretherton et al., 2013). For the timescale analysis, we have yet to ascertain the degree to which the fast timescale is relevant to decoupled boundary layers. We hypothesize that it will remain important for any stratocumulus layer that generates significant cloud top entrainment, but this still needs to be tested in LES. This is the most important next logical step for analyzing the fast timescale. It would be particularly interesting to see how this fast timescale responds as the well-mixed boundary layer becomes more decoupled and the stratocumulus cloud coverage decreases and gives way to shallow cumulus. Whether or not an observational test can be designed to detect the fast timescale or its underlying entrainment-LWP feedback mechanism is worthy of further consideration.

An interesting potential application of the timescales analysis is the possibility it can be used to improve and differentiate between entrainment closures by analyzing the response of the STBL LWP to an appropriate time-varying forcing. Since the output phase lag, amplitude, and shape of a linear system of ODEs relative to a driving time-varying forcing depends on its eigenvalues and eigenvectors, this may present an indirect means of assessing how responsive an entrainment closure is to various perturbations, and could be particularly useful in the absence of high-accuracy observational measurements of the entrainment rate

in STBLs.

This dissertation relied heavily on several modelling frameworks: MLM, SCM, GCM, and LES all contributed to some portion of this work. By using these models in concert we are able to play off of their relative strengths and weaknesses and gain a better overall understanding of which responses are robust, which are particularly uncertain, and where the greatest modelling deficiencies and challenges remain.

BIBLIOGRAPHY

Ackerman, A. S., Kirkpatrick, M. P., Stevens, D. E., and Toon, O. B., 2004: The impact of humidity above stratiform clouds on indirect aerosol climate forcing. *Nature*, **432**(7020), 1014–1017.

Ackerman, A. S., vanZanten, M. C., Stevens, B., Savic-Jovcic, V., Bretherton, C. S., Chlond, A., et al., 2009: Large-eddy simulations of a drizzling, stratocumulus-topped marine boundary layer. *Mon. Wea. Rev.*, **137**(3), 1083–1110.

Albrecht, B. A., 1989: Aerosols, cloud microphysics, and fractional cloudiness. *Science*, **245**(4923), 1227–1230.

Bellon, G. and Stevens, B., 2012: Time scales of the trade wind boundary layer adjustment. *J. Atmos. Sci.*, **70**(4), 1071–1083.

Blossey, P. N., Bretherton, C. S., Zhang, M., Cheng, A., Endo, S., Heus, T., et al., 2013: Marine low cloud sensitivity to an idealized climate change: The CGILS LES intercomparison. *Journal of Advances in Modeling Earth Systems*, 1–25. doi:10.1002/jame.20025.

Blossey, P. N. and Durran, D. R., 2008: Selective monotonicity preservation in scalar advection. *Journal of Computational Physics*, **227**(10), 5160 – 5183. doi:10.1016/j.jcp.2008.01.043.

Bolton, D., 1980: The computation of equivalent potential temperature. *Mon. Wea. Rev.*, **108**(7), 1046–1053.

Bony, S., Colman, R., Kattsov, V. M., Allan, R. P., Bretherton, C. S., Dufresne, J.-L., et al., 2006: How well do we understand and evaluate climate change feedback processes? *Journal of Climate*, **19**(15), 3445–3482.

Bony, S. and Dufresne, J., 2005: Marine boundary layer clouds at the heart of tropical cloud feedback uncertainties in climate models. *Geophysical Research Letters*, **32**(20), L20806. doi:10.1029/2005GL023851.

Bony, S., Dufresne, J., Le Treut, H., Morcrette, J., and Senior, C., 2004: On dynamic and thermodynamic components of cloud changes. *Climate Dynamics*, **22**(2-3), 71–86. doi:10.1007/s00382-003-0369-6.

Boyce, W. E. and DiPrima, R. C., 2008: *Elementary Differential Equations and Boundary Value Problems*. Wiley, 9 edition.

Bretherton, C., Uttal, T., Fairall, C., Yuter, S., Weller, R., Baumgardner, D., et al., 2004: The epic 2001 stratocumulus study. *Bulletin of the American Meteorological Society*, **85**(7), 967+. doi:10.1175/BAMS-85-7-967.

Bretherton, C. S., Blossey, P. N., and Jones, C. R., 2013: Mechanisms of marine low cloud sensitivity to idealized climate perturbations: A single-LES exploration extending the CGILS cases. *Journal of Advances in Modeling Earth Systems*, 1–22. doi:10.1002/jame.20019.

Bretherton, C. S., Blossey, P. N., and Uchida, J., 2007: Cloud droplet sedimentation, entrainment efficiency, and subtropical stratocumulus albedo. *Geophys. Res. Lett.*, **34**(3), 1–5. doi:10.1029/2006GL027648.

Bretherton, C. S. and Park, S., 2009a: A new moist turbulence parameterization in the community atmosphere model. *J. Climate*, **22**(12), 3422–3448.

Bretherton, C. S. and Park, S., 2009b: A new moist turbulence parameterization in the community atmosphere model. *J. Climate*, **22**(12), 3422–3448.

Bretherton, C. S., Uchida, J., and Blossey, P. N., 2010: Slow manifolds and multiple equilibria in stratocumulus-capped boundary layers. *Journal of Advances in Modeling Earth Systems*, **2**(14), 1–20. doi:10.3894/JAMES.2010.2.14.

Bretherton, C. S. and Wyant, M. C., 1997: Moisture transport, lower-tropospheric stability, and decoupling of cloud-topped boundary layers. *Journal of the Atmospheric Sciences*, **54**(1), 148–167.

Brient, F. and Bony, S., 2013: Interpretation of the positive low-cloud feedback predicted by a climate model under global warming. *Climate Dynamics*, **40**(9-10), 2415–2431. doi:10.1007/s00382-011-1279-7.

Caldwell, P. and Bretherton, C. S., 2009: Response of a subtropical stratocumulus-capped mixed layer to climate and aerosol changes. *Journal of Climate*, **22**(1), 20–38. doi:10.1175/2008JCLI1967.1.

Caldwell, P., Bretherton, C. S., and Wood, R., 2005: Mixed-layer budget analysis of the diurnal cycle of entrainment in southeast pacific stratocumulus. *Journal of the Atmospheric Sciences*, **62**(10), 3775–3791.

Caldwell, P. M., Zhang, Y., and Klein, S. A., 2012: Cmip3 subtropical stratocumulus cloud feedback interpreted through a mixed-layer model. *J. Climate*, **26**(5), 1607–1625.

Cess, R. D., Potter, G. L., Blanchet, J. P., Boer, G. J., Genio, A. D. D., Dqu, M., et al., 1990: Intercomparison and interpretation of climate feedback processes in 19 atmospheric general circulation models. *Journal of Geophysical Research*, **95**(D10), 16,601–16,615. doi:199010.1029/JD095iD10p16601.

Chen, T., Rossow, W. B., and Zhang, Y., 2000: Radiative effects of cloud-type variations. *J. Climate*, **13**(1), 264–286.

Christensen, M. W., Stephens, G. L., Carrio, G. G., and Cotton, W. R., 2013: Radiative impacts of cirrus on the properties of marine stratocumulus. *J. Geophys. Res.*, in press.

Coakley, J. A. and Walsh, C. D., 2002: Limits to the aerosol indirect radiative effect derived from observations of ship tracks. *J. Atmos. Sci.*, **59**(3), 668–680.

Comstock, K., Bretherton, C., and Yuter, S., 2005: Mesoscale variability and drizzle in southeast pacific stratocumulus. *Journal of the Atmospheric Sciences*, **62**(10), 3792–3807.

Eaton, B. E., 2010: User's guide to the community atmosphere model am4.0. Technical report, NCAR.

Forsythe, G., Malcolm, M., and Moler, C., 1977: *Computer Methods for Mathematical Computations*. Prentic-Hall.

Gettelman, A., Morrison, H., and Ghan, S. J., 2008: A new two-moment bulk stratiform cloud microphysics scheme in the community atmosphere model, version 3 (cam3). part ii: Single-column and global results. *J. Climate*, **21**(15), 3660–3679.

Grenier, H. and Bretherton, C. S., 2001: A moist pbl parameterization for large-scale models and its application to subtropical cloud-topped marine boundary layers. *Mon. Wea. Rev.*, **129**(3), 357–377.

Hahn, C. and Warren, S. G., 2007 (updated 2009): A gridded climatology of clouds over land (1971-1996) and ocean (1954-2008) from surface observations worldwide. Technical Report NDP-026E, CDIAC, Department of Energy, Oak Ridge, TN. Documentation, 71 pp.

Hartmann, D. L., 1994: *Global Physical Climatology*. Academic Press.

Hartmann, D. L. and Short, D. A., 1980: On the use of earth radiation budget statistics for studies of clouds and climate. *J. Atmos. Sci.*, **37**(6), 1233–1250.

Iacono, M. J., Delamere, J. S., Mlawer, E. J., Shephard, M. W., Clough, S. A., and Collins, W. D., 2008: Radiative forcing by long-lived greenhouse gases: Calculations with the aer radiative transfer models. *J. Geophys. Res.*, **113**(D13), D13103–.

IPCC, 2007: *Climate Change 2007: The Physical Science Basis. [Solomon, S., D. Qin, M. Manning, Z. Chen, M. Marquis, K.B. Averyt, M.Tignor and H.L. Miller (eds.)]*. Cambridge University Press, Cambridge, United Kingdom and New York, NY, USA.

Jones, C. R., Bretherton, C. S., and Leon, D., 2011: Coupled vs. decoupled boundary layers in vocals-rex. *Atmospheric Chemistry and Physics*, **11**(14), 7143–7153. doi:10.5194/acp-11-7143-2011.

Khairoutdinov, M. and Kogan, Y., 2000: A new cloud physics parameterization in a large-eddy simulation model of marine stratocumulus. *Mon. Wea. Rev.*, **128**(1), 229–243.

Khairoutdinov, M. F. and Randall, D. A., 2003: Cloud resolving modeling of the ARM summer 1997 IOP: model formulation, results, uncertainties, and sensitivities. *J. Atmos. Sci.*, **60**(4), 607–625. doi:10.1175/1520-0469(2003)060⟨0607:CRMOTA⟩2.0.CO;2.

Klein, S. A. and Hartmann, D. L., 1993: The seasonal cycle of low stratiform clouds. *J. Climate*, **6**(8), 1587–1606.

Lauer, A., Hamilton, K., Wang, Y., Phillips, V. T. J., and Bennartz, R., 2010: The impact of global warming on marine boundary layer clouds over the eastern pacifica regional model study. *Journal of Climate*, **23**(21), 5844–5863. doi:10.1175/2010JCLI3666.1.

Leon, D. C., Wang, Z., and Liu, D., 2008: Climatology of drizzle in marine boundary layer clouds based on 1 year of data from cloudsat and cloud-aerosol lidar and infrared pathfinder satellite observations (calipso). *J. Geophys. Res.*, **113**(D8), D00A14–.

Lewellen, D. C. and Lewellen, W. S., 1998: Large-eddy boundary layer entrainment. *J. Atmos. Sci.*, **55**(16), 2645–2665.

Lilly, D., 1968: Models of cloud-topped mixed layers under a strong inversion. *Quarterly Journal of the Royal Meteorological Society*, **94**(401), 292–309.

Lin, S.-J. and Rood, R. B., 1996: Multidimensional flux-form semi-lagrangian transport schemes. *Mon. Wea. Rev.*, **124**(9), 2046–2070.

Lin, W., Zhang, M., and Loeb, N. G., 2009: Seasonal variation of the physical properties of marine boundary layer clouds off the california coast. *J. Climate*, **22**(10), 2624–2638.

Lock, A. P., Brown, A. R., Bush, M. R., Martin, G. M., and Smith, R. N. B., 2000a: A new boundary layer mixing scheme. part i: Scheme description and single-column model tests. *Mon. Wea. Rev.*, **128**(9), 3187–3199.

Lock, A. P., Brown, A. R., Bush, M. R., Martin, G. M., and Smith, R. N. B., 2000b: A new boundary layer mixing scheme. part i: Scheme description and single-column model tests. *Mon. Wea. Rev.*, **128**(9), 3187–3199.

Loeb, N. G., Wielicki, B. A., Doelling, D. R., Smith, G. L., Keyes, D. F., Kato, S., et al., 2009: Toward optimal closure of the earth's Top-of-Atmosphere radiation budget. *Journal of Climate*, **22**, 748–766. doi:10.1175/2008JCLI2637.1.

Lu, J. and Cai, M., 2009: Stabilization of the atmospheric boundary layer and the muted global hydrological cycle response to global warming. *J. Hydrometeor*, **10**(1), 347–352.

Marshall, J. S. and Palmer, W. M. K., 1948: The distribution of raindrops with size. *J. Meteor.*, **5**(4), 165–166.

Meehl, G. A., Covey, C., Taylor, K. E., Delworth, T., Stouffer, R. J., Latif, M., et al., 2007: The wcrp cmip3 multimodel dataset: A new era in climate change research. *Bull. Amer. Meteor. Soc.*, **88**(9), 1383–1394.

Mlawer, E., Taubman, S., Brown, P., Iacono, M., and Clough, S., 1997: Radiative transfer for inhomogeneous atmospheres: RRTM, a validated correlated-k model for the longwave. *Journal of Geophysical Research-Atmospheres*, **102**(D14), 16663–16682. doi: 10.1029/97JD00237.

Morrison, H. and Gettelman, A., 2008: A new two-moment bulk stratiform cloud microphysics scheme in the community atmosphere model, version 3 (cam3). part i: Description and numerical tests. *J. Climate*, **21**(15), 3642–3659.

Myers, T. A. and Norris, J. R., 2013: Observational evidence that enhanced subsidence reduces subtropical marine boundary layer cloudiness. *J. Climate*, –. doi: 10.1175/JCLI-D-12-00736.1.

Neale, R. B., Gettelman, A., Park, S., Chen, C.-C., Lauritzen, P. H., Williamson, D. L., et al., 2010: Description of the ncar community atmosphere model (cam 5.0). Scientific and Technical Note NCAR/TN-486+STR, NCAR.

Nicholls, S., 1984: The dynamics of stratocumulus - aircraft observations and comparisons with a mixed layer model. *Quarterly Journal of the Royal Meteorological Society*, **110**(466), 783–820.

Nicholls, S. and Leighton, J., 1986: An observational study of the structure of stratiform cloud sheets: Part i. structure. *Q.J.R. Meteorol. Soc.*, **112**(472), 431–460.

Nicholls, S. and Turton, J., 1986: An observational study of the structure of stratiform cloud sheets. part ii: entrainment. *Quarterly Journal of the Royal Meteorological Society*, **112**(472), 461–480.

Norris, J. R. and Iacobellis, S. F., 2005: North pacific cloud feedbacks inferred from synoptic-scale dynamic and thermodynamic relationships. *J. Climate*, **18**(22), 4862–4878.

Park, S. and Bretherton, C. S., 2009: The university of washington shallow convection and moist turbulence schemes and their impact on climate simulations with the community atmosphere model. *J. Climate*, **22**(12), 3449–3469.

Pierrehumbert, R. T., 1995: Thermostats, radiator fins, and the local runaway greenhouse. *J. Atmos. Sci.*, **52**(10), 1784–1806.

Quaas, J., Ming, Y., Menon, S., Takemura, T., Wang, M., Penner, J. E., et al., 2009: Aerosol indirect effects – general circulation model intercomparison and evaluation with satellite data. *Atmospheric Chemistry and Physics*, **9**(22), 8697–8717. doi: 10.5194/acp-9-8697-2009.

Ramanathan, V., Cess, R. D., Harrison, E. F., Minnis, P., Barkstrom, B. R., Ahmad, E., et al., 1989: Cloud-radiative forcing and climate: Results from the earth radiation budget experiment. *Science*, **243**(4887), pp. 57–63.

Randall, D., 1980: Conditional instability of the 1st kind upside-down. *Journal of the Atmospheric Sciences*, **37**(1), 125–130.

Randall, D., Wood, R., Bony, S., Colman, R., Fichefet, T., Fyfe, J., et al., 2007: Climate models and their evaluation. In S. Solomon, D. Qin, M. Manning, Z. Chen, M. Marquis, K. Averyt, M. Tignor, and H. Miller, editors, *Climate Change 2007: The Physical*

Science Basis. Contribution of Working Group I to the Fourth Assessment Report of the Intergovernmental Panel on Climate Change. Cambridge University Press, Cambridge, United Kingdom and New York, NY, USA.

Randall, D. A., 1984: Stratocumulus cloud deepening through entrainment. *Tellus A*, **36**(5), 446–457.

Randall, D. A., Coakley, J. A., Lenschow, D. H., Fairall, C. W., and Kropfli, R. A., 1984: Outlook for research on subtropical marine stratification clouds. *Bull. Amer. Meteor. Soc.*, **65**(12), 1290–1301.

Randall, D. A., Xu, K.-m., Somerville, R. J. C., and Iacobellis, S., 1996: Single-column models and cloud ensemble models as links between observations and climate models. *J. Climate*, **9**(8), 1683–1697.

Richter, I. and Xie, S.-P., 2008: Muted precipitation increase in global warming simulations: A surface evaporation perspective. *Journal of Geophysical Research: Atmospheres*, **113**(D24), n/a–n/a. doi:10.1029/2008JD010561.

Rogers, R. R. and Yau, M. K., 1989: *A Short Clourse in Cloud Physics*. Elsevier, New York, 3rd edition.

Sandu, I. and Stevens, B., 2011: On the factors modulating the stratocumulus to cumulus transitions. *J. Atmos. Sci.*, **68**(9), 1865–1881.

Schubert, W. H., Wakefield, J. S., Steiner, E. J., and Cox, S. K., 1979a: Marine stratocumulus convection. part i: Governing equations and horizontally homogeneous solutions. *J. Atmos. Sci.*, **36**(7), 1286–1307. doi:10.1175/1520-0469(1979)036⟨1286:MSCPIG⟩2.0.CO;2.

Schubert, W. H., Wakefield, J. S., Steiner, E. J., and Cox, S. K., 1979b: Marine stratocumulus convection. part ii: Horizontally inhomogeneous solutions. *J. Atmos. Sci.*, **36**(7), 1308–1324.

Sherwood, S. C., Ingram, W., Tsushima, Y., Satoh, M., Roberts, M., Vidale, P. L., et al., 2010: Relative humidity changes in a warmer climate. *Journal of Geophysical Research: Atmospheres*, **115**(D9), n/a–n/a. doi:10.1029/2009JD012585.

Slingo, A., 1990: Sensitivity of the earth's radiation budget to changes in low clouds. *Nature*, **343**(6253), 49–51.

Soden, B. J., Held, I. M., Colman, R., Shell, K. M., Kiehl, J. T., and Shields, C. A., 2008: Quantifying climate feedbacks using radiative kernels. *Journal of Climate*, **21**(14), 3504 – 3520.

Soden, B. J. and Vecchi, G. A., 2011: The vertical distribution of cloud feedback in coupled ocean-atmosphere models. *Geophysical Research Letters*, **38**, 6 PP. doi:201110.1029/2011GL047632.

Stevens, B., 2002: Entrainment in stratocumulus-topped mixed layers. *Quarterly Journal of the Royal Meteorological Society*, **128**(586), 2663–2690. doi:10.1256/qj.01.202.

Stevens, B., 2006: Bulk boundary-layer concepts for simplified models of tropical dynamics. *Theoretical and Computational Fluid Dynamics*, **20**(5-6), 279–304.

Stevens, B., Beljaars, A., Bordoni, S., Holloway, C., Khler, M., Krueger, S., et al., 2007: On the structure of the lower troposphere in the summertime stratocumulus regime of the northeast pacific. *Mon. Wea. Rev.*, **135**(3), 985–1005.

Stevens, B., Chin-Hoh, M., Ackerman, A. S., Bretherton, C. S., Chlond, A., de Roode, S., et al., 2005: Evaluation of large-eddy simulations via observations of nocturnal marine stratocumulus. *Monthly Weather Review*, **133**(6), 1443 – 1462.

Stevens, B. and Feingold, G., 2009: Untangling aerosol effects on clouds and precipitation in a buffered system. *Nature*, **461**(7264), 607–613.

Stevens, B., Lenschow, D. H., Vali, G., Gerber, H., Bandy, A., Blomquist, B., et al., 2003: Dynamics and chemistry of marine stratocumulusdycoms-ii. *Bull. Amer. Meteor. Soc.*, **84**(5), 579–593.

Strogatz, S. H., 2001: *Nonlinear Dynamics and Chaos: With Applications to Physics, Biology, Chemistry, and Engineering*. Westview Press.

Turton, J. and Nicholls, S., 1987: A study of the diurnal-variation of stratocumulus using a multiple mixed layer model. *Quarterly Journal of the Royal Meteorological Society*, **113**(477), 969–1009.

Twomey, S., 1974: Pollution and the planetary albedo. *Atmospheric Environment (1967)*, **8**(12), 1251 – 1256. doi:10.1016/0004-6981(74)90004-3.

Twomey, S., 1977: The influence of pollution on the shortwave albedo of clouds. *J. Atmos. Sci.*, **34**(7), 1149–1152.

Uchida, J., Bretherton, C. S., and Blossey, P. N., 2010: The sensitivity of stratocumulus-capped mixed layers to cloud droplet concentration: do LES and mixed-layer models agree? *Atmospheric Chemistry and Physics*, **10**(9), 4097–4109. doi:10.5194/acp-10-4097-2010.

van der Dussen, J. J., de Roode, S. R., and Siebesma, A. P., 2013: Factors controlling rapid stratocumulus cloud thinning. Submitted to J. Clim.

van Driel, R. and Jonker, H. J. J., 2010: Convective boundary layers driven by nonstationary surface heat fluxes. *J. Atmos. Sci.*, **68**(4), 727–738.

Vecchi, G. A. and Soden, B. J., 2007: Global warming and the weakening of the tropical circulation. *J. Climate*, **20**(17), 4316–4340.

Wang, M., Ghan, S., Ovchinnikov, M., Liu, X., Easter, R., Kassianov, E., et al., 2011: Aerosol indirect effects in a multi-scale aerosol-climate model PNNL-MMF. *Atmospheric Chemistry and Physics*, **11**, 5431–5455.

Warren, S., Hahn, C., London, J., Chervin, R., and Jenne, R., 1986: *Global Distribution of Total Cloud Cover and Cloud Type Amounts Over Land*. National Center for Atmospheric Research.

Warren, S. G., Hahn, C. H., London, J., Chervin, R. M., and Jenne, R. L., 1988: Global distribution of total cloud cover and cloud type amounts over the ocean. Technical report, United States Department of Energy.

Webb, M., Lambert, F., and Gregory, J., 2013: Origins of differences in climate sensitivity, forcing and feedback in climate models. *Climate Dynamics*, **40**(3-4), 677–707. doi:10.1007/s00382-012-1336-x.

Webb, M. J. and Lock, A. P., 2012: Coupling between subtropical cloud feedback and the local hydrological cycle in a climate model. *Climate Dyn.*, –. doi:10.1007/s00382-012-1608-5.

Wood, R., 2007: Cancellation of aerosol indirect effects in marine stratocumulus through cloud thinning. *J. Atmos. Sci.*, **64**(7), 2657–2669.

Wood, R., 2012: Stratocumulus clouds. *Mon. Wea. Rev.*, **140**(8), 2373–2423.

Wood, R. and Bretherton, C. S., 2006: On the relationship between stratiform low cloud cover and lower-tropospheric stability. *Journal of Climate*, **19**(24), 6425–6432.

Wood, R., Mechoso, C. R., Bretherton, C. S., Weller, R. A., Huebert, B., Straneo, F., et al., 2011: The vamos ocean-cloud-atmosphere-land study regional experiment (vocals-rex): goals, platforms, and field operations. *Atmospheric Chemistry and Physics*, **11**(2), 627–654. doi:10.5194/acp-11-627-2011.

Wyant, M. C., Bretherton, C. S., Chlond, A., Griffin, B. M., Kitagawa, H., Lappen, C.-L., et al., 2007: A single-column model intercomparison of a heavily drizzling stratocumulus-topped boundary layer. *J. Geophys. Res.*, **112**(D24), D24204–.

Xu, K.-M., Cheng, A., and Zhang, M., 2010: Cloud-resolving simulation of low-cloud feedback to an increase in sea surface temperature. *J. Atmos. Sci.*, **67**(3), 730–748.

Zhang, G. and McFarlane, N. A., 1995: Sensitivity of climate simulations to the parameterization of cumulus convection in the canadian climate centre general circulation model. *Atmosphere-Ocean*, **33**(3), 407–446.

Zhang, M. and Bretherton, C., 2008: Mechanisms of low cloud-climate feedback in idealized single-column simulations with the community atmospheric model, version 3 (CAM3). *Journal of Climate*, **21**(18), 4859–4878. doi:10.1175/2008JCLI2237.1.

Zhang, M., Bretherton, C. S., Blossey, P. N., Austin, P. H., Bacmeister, J. T., Bony, S., et al., 2013: CGILS: results from the first phase of an international project to understand the physical mechanisms of low cloud feedbacks in general circulation models. Submitted to *JAMES*.

Zhu, P., Bretherton, C. S., Khler, M., Cheng, A., Chlond, A., Geng, Q., et al., 2005: Intercomparison and interpretation of single-column model simulations of a nocturnal stratocumulus-topped marine boundary layer. *Mon. Wea. Rev.*, **133**(9), 2741–2758.